# Oroclines, their scale and tectonic requirements: Insights from thermo-mechanical analogue models

by

Laurence Gagnon
BSc, McGill University, 2011

A Thesis Submitted in Partial Fulfillment
of the Requirements for the Degree of

MASTER OF SCIENCE

in the School of Earth and Ocean Sciences

## Supervisory Committee

# Oroclines, their scale and tectonic requirements: Insights from thermo-mechanical analogue models

by

Laurence Gagnon
BSc, McGill University, 2011

## Supervisory Committee

Stephen Johnston, School of Earth and Ocean Sciences
**Supervisor**

Adam Monahan, School of Earth and Ocean Sciences
**Departmental Member**

Colin Goldblatt, School of Earth and Ocean Sciences
**Departmental Member**

# Abstract

We use scaled 3-D thermo-mechanical analogue models to investigate the formation of oroclines (originally linear orogens now curved in map view by buckling about vertical axes). The experimental setup consists of a tank of water (the asthenosphere) on top of which rest hydrocarbon plates (the lithosphere) with strain-softening behaviours and thermo-dependent elasto-plastic properties. An electric heating element below and 4 infrared lights above produce a constant vertical (geo)thermal gradient in the plates. A horizontal piston drives constant plate motion and gives rise to a compressional stress regime. Geometric, kinematic and dynamic variables are calibrated in accordance with a set of scaling laws and proper plate composition.

Our results suggest that oroclinal buckling involves the entire lithosphere and cannot be confined to the crust only. A wide range of syn-oroclinal structures developed during buckling, including thin- to thick-skinned thrust belts, transform faults and extensional structures, as well as extensional basins and subduction zones in the lithosphere adjacent to the ribbons. During oroclinal buckling, a thrust belt forms upon complete closure of the interlimb region and is attributable to the trailing orocline limb overthrusting the leading orocline limb. An analogous syn-oroclinal thrust system characterizes the Central Iberian Orocline (CIO) of the Variscan orogen in Iberia where the north limb of the west-convex orocline exposes recumbent north-verging folds while the overriding south limb bears upright to gently north-verging folds. Our results imply that these structures developed during final closure of the CIO, and indicate that the north- and south- limbs of the CIO constitute the leading- and trailing-limbs, respectively, of an orocline that formed by overall northward translation. Modelling of magmatic arcs rotating about vertical axes yields late stage transform faults that bisect the buckling arcs. This outcome is analogous to the Panama Canal fault zone that severs the buckled Panamanian Isthmus. The hinge zones of modeled oroclines are the sites of subduction initiation, similar to subduction initiation of the Caribbean plate beneath the convex to the north, North Panamanian orocline, and of oceanic lithosphere from the Ionian Sea beneath the Calabrian orocline of Sicily.

# Table of Contents

# List of Tables

# List of Figures

# Acknowledgements

Only a few years within Seos Ranks
Yet so many people deserve proper ‘thanks’

First and foremost my resourceful supervisor, Stephen
For your time, ideas, wisdom and a project to believe in

I am equally grateful to David and his modeling device
Granting me to see buckling oroclines with my own eyes

Thank you Adam and Colin, for your precious feedback
Jordan and Jess, I couldn’t think of any sufficient payback
Philippe*, cheers to your skills and successful video-hack

And how to forget my dear Alexandra
With your heart wide as the Tundra

Finally, I am sincerely thankful to my family and friends
For which I would do anything, even forge mountain bends

*Chapter 1*

# 1. Introduction

This study presents and interprets the results from a series of analogue modeling experiments on oroclines. This introduction chapter first defines the oroclines and shows some natural analogues. Then the main questions are presented and a solution to address them is offered at last.

The term "orocline" was defined by S.W. Carey (1955) as an originally linear 'orogenic system which has been flexed in plan to an elbow or horseshoe shape'. The oroclinal model implies two compressional events: one that forms the orogen and an other that folds it. Three well-studied examples will be discussed throughout this thesis:

A) The coupled oroclines of the Variscan, covering most of Spain (Weil. Et al. 2013; Johnston 2013). The southern of the two buckles, the Central Iberian Orocline, comprises a domain of upright folds and another of recumbent folds (Diez Balda et al., 1990) along with disynchronous episodes of magmatism and isotopic signs of mantle renewal.

B) At the bridge that has connected the North and South Americas in the mid-late Miocene (10 Ma; Marshall et al., 1979), lies another orocline, the Panama deformed belt. The Paleogene volcanics of the arc are offset in the vicinity of the Panama Canal where transpressional systems are in place. The Caribbean oceanic plate presently underthrusts the continental ismuth of Panama (Coates 2004).

C) The Apennine Mountains and the Silice are currently rotating, closing the Calabrian orocline upon compression between Europe and Africa (Johnston & Mazzoli). An extensional basin to the West has opened the Tyrrhenian Sea, and to the East, the mountain belt overrides the oceanic lithosphere of the Ionian Sea.

Though oroclines are common features of orogenic belts globally, fundamental aspects associated with their formation are not understood. These include 1) Mechanisms by which an orogen may deform by the implied 'buckling' about a vertical axis, 2) the full

manner and extent of deformation associated (scale: thin-skinned vs. thick-skinned), and 3) the tectonic settings through which buckling can be initiated (Carey, 1955, Weil and Sussman, 2004; Van der Voo, 2004, Marshak, 2004; Johnston and Mazzoli, 2008; Johnston et al., 2013).

The degree to which critical questions regarding the large-scale and protracted geologic processes involved with orocline formation can be assessed by conventional field analyses is limited. We address these questions with the first attempts to thermo-physically model oroclinal buckling using paraffin-wax analogues. The model, at its simplest, consists of the application of horizontal compressional stress parallel to elongated paraffin plates [the lithosphere] at rest on top of a pool of water [the asthenosphere]. The paraffin plates are subjected to a vertical strength gradient [geotherm], which generates a strength profile representative of that of the Earth (Boutelier et al., 2004). Empirical parameters explored include 1) manipulation of the initial geometry and material composition of the continental ribbon, 2) boundary-control at the ribbon's margins, and 3) variation in the extent and dynamics of the compression regime. Our experiments provide new constraints on 1) tectonic initiation of oroclinal buckling 2) the geologic scale, geometry and dynamics of oroclinal deformation and 3) the nature of structural accommodations involved in the development of tight to isoclinal oroclines, for which modern analogues can be found in the Central Iberian, Panamanian, and Calabrian oroclines.

It is the objective of the plate tectonic modeller to insure that the co-dependent experimental settings (2.2.) are representative of natural geologic systems. This goal may be achieved if empirical variables are proportionally scaled, if the models' vertical strength profiles are representative of those within the Earth's lithosphere, and if the geometries and boundaries of the paraffin ribbons are tectonically realistic.

*Chapter 2*

# 2. Experimental Design and Methods

## 2.1. Modelling apparatus

Given its simplicity and acute realism, the analogue modelling of plate tectonic processes using materials such as sand, clay, silicone and wax to embody lithospheric plates is a preferred modelling technique (Ghosh et al., 1995; Boutelier et al., 2003; Zulauf, 2004; Johnston, 2004; Schreurs et al., 2006; Pastor-Galan et al., 2012). This study employs the thermo-mechanical lithospheric-scale modelling apparatus (**Fig. 1**) developed by Boutelier (Boutelier et al., 2004; Bouterlier and Chemenda, 2008, 2011; Boutelier and Oncken, 2011), which, unlike many other anologue devices, is capable of expressing the temperature and strength gradients of the lithosphere with a three-dimensional perspective.

Desired material thermo-mechanical properties (density, thermal diffusivity, elasto-plasticity, ductility, etc.) can be acquired with precise mixtures of paraffin, microcrystalline waxes, Vaseline, and paraffin oil, all held together with a highly branched alpha-olefin polymer. The model will only be representative of nature if these properties are proportionally scaled with respect to nature.

The rheological strength (2.2.2.) of the crust and mantle are dependent on pressure, temperature and mineralogy, all of which vary as a function of depth. Successful lithospheric-scale thermo-mechanical models must generate realistic depth-strength profiles. The thermo-mechanical modelling apparatus conceived by Boutelier (2004, 2011, 2012, 2013) achieves this through rheological and compositional vertical stratification. Strength gradients are controlled empirically by generating a vertical thermal gradient through materials with specific elasto-plastic properties and temperature-dependent strengths. A thermo-dependent ductility gradient is likewise induced, reflecting the range of

brittle and ductile behaviors in the crust and lithospheric mantle (Byerlee, 1978; Ranalli and Murph 1987; Ranalli 1997).

The near-rigid lithospheric shell of the Earth is underlain by a hot, fluid-like asthenosphere with several orders of magnitude higher strain-rates, which is independently mobile and exerts only a small shear traction on the overlying plates. The main role of the asthenosphere is to maintain hydrostatic equilibrium, and its accurate modelling depends on a realistic calibration of the astheno-lithospheric density ratio. For convenience the asthenosphere is represented by water, with its density defined as the standard. This provides a convective environment, fulfilling the important prerequisite of a relatively isothermal asthenosphere. The small shear traction exerted on the lithosphere by the asthenosphere, when integrated over the large areas of the plates, equates to substantial drag forces. These forces add to the other tectonic forces to create large-scale compressional and extensional regimes that are responsible for deformation features across the globe.

The compressional regime required for oroclinal deformation is provided by a mobile piston which presses the paraffin plates horizontally against a stationary back-wall. The piston's velocity is appropriately scaled (section 2.3.1.) to be representative of relative plate motions at rates that could be up to tens of centimeters/year, dynamism typical of the high stress fields of natural subduction systems. In order to buckle (fold) about a vertical axis, compressional stress ($\sigma_1$) must be horizontal and parallel to the long axis of the continental ribbon (Carey 1955). The piston is therefore oriented orthogonally to the paraffin beam. The extent and nature of strain depends not only on the intensity of the tectonic stresses (compression from the piston) but also on the yield strength of the lithospheric material (paraffin plates).

The modelling device employed in this study provides a detailed and broad dataset for each modelling experiment. Strain systems are investigated by means of Particle Imaging

Velocimetry (PIV) (Hampel, 2004; Adam et al., 2005), an efficient non-invasive method of measuring displacement and deformation via an image correlation. For a complete enquiry of the model's 3-dimensional dynamics and deformation, PIV cameras are installed on the top of the tank providing a quantitative examination, and also on its sides for a more qualitative survey. Thermal probes connected to a thermo-regulator (adjusting the length of the heat pulses produced by the heater and infrared emitters) are employed to calibrate the heat gradient. Force sensors mounted along the back-wall of the tank allow approximation of total stress induced in the system. Once an experiment is complete, with the modeled paraffin plates cooled and solidified at their final state, they can be bisected to expose any cross-section desired.

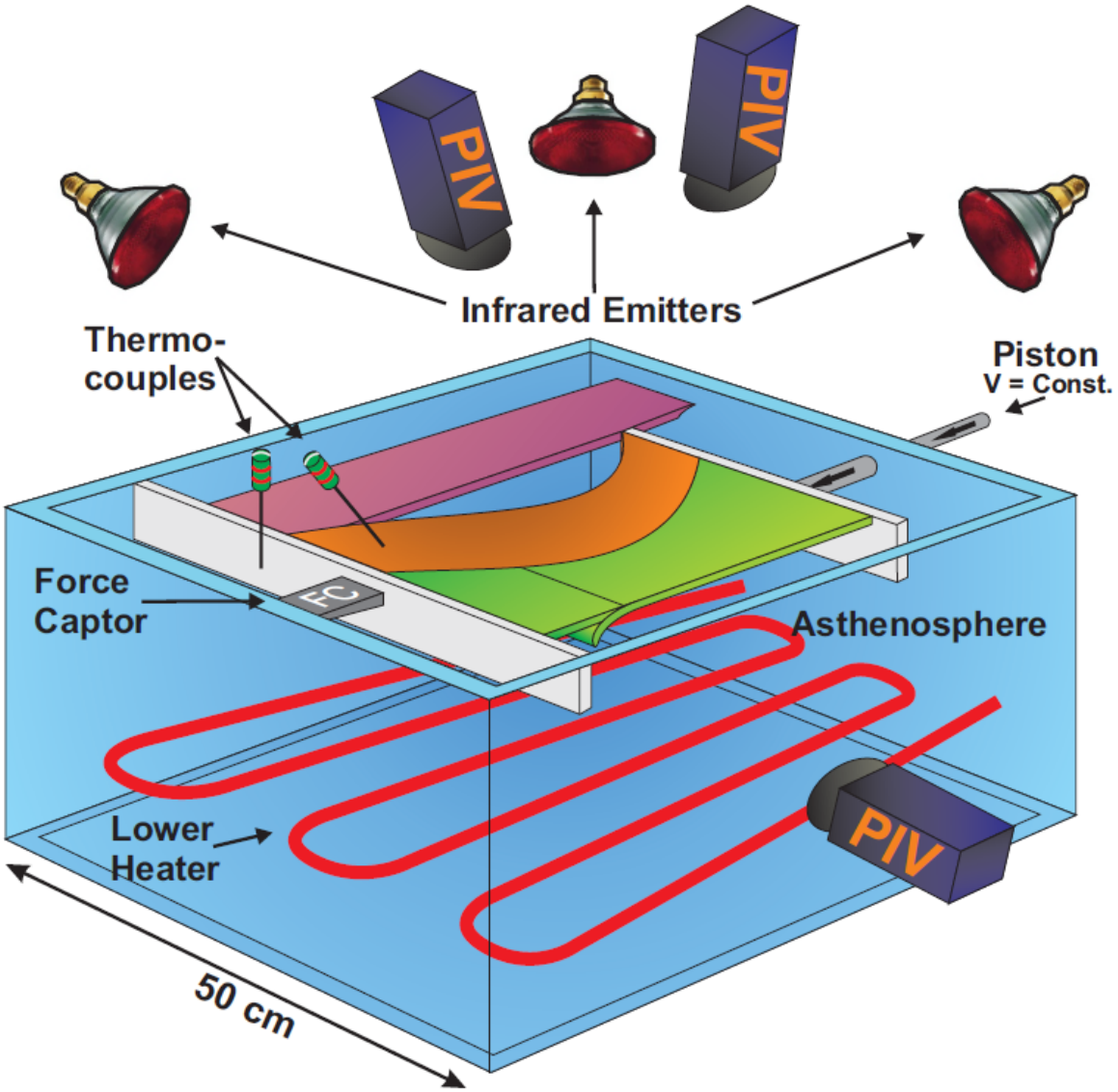


**Figure 1. Sketch of the experimental setup. The apparatus consists of a 50 cm wide tank of water [asthenosphere] on top of which rest paraffin plates [tectonic plates] with thermo-dependent strengths. At the bottom of the water, an electric heating element keeps the water at 40°C. Above, 4 infrared lights are suspended, emitting an adjustable amount of heat which keeps the surface of the paraffin plates at 36,5°C. The paraffin surface and water temperatures are measured by two thermal probes connected to a thermo-regulator adjusting the length of the heat pulses produced by the electric heater and infrared emitters. This configuration ensures a constant thermal gradient [geothermal gradient] which is fundamental for realistic lithospheric strength profiles. A mobile piston induces the compressional stress [compressional regime] required to deform the plates. The piston can vary in velocity [relative plate motion] but also in width, giving the option to compress all the plates, some of them or only one in particular [tectonic scenario]. The model motions are monitored at the surface and on the side with cameras, and strain system and deformation are computed via a P.I.V. technique. FC = Force Captor**

## 2.2. Experimental Parameters

### 2.2.1. Scaling laws

The bridge built between nature and the models holds essentially on the scaling laws that are adopted. The latter are at the heart of the principle of analogue modelling, ensuring that geometric, kinematic and dynamic variables are proportionally balanced and representative of natural geologic scenarios (Buckingham, 1914; Shemenda, 1994). To attain this, the modeller must define non-dimensional ratios of the controlling thermo-mechanical parameters. These ratios should be equal in nature and in experiments and can be deduced either from a dimension analysis of the controlling parameters or directly from mathematical equations designated for a specific geologic subject, provided these equations are known (Boutelier and Chemanda, 2011). Once lengths (vertical and horizontal), densities, thermal diffusivities, velocities and strengths are properly scaled down (Buckingham, 1914; Ramberg, 1967; Davy and Cobbold, 1991; Shemenda, 1994), the laboratory model should operate identically to its natural analogue.

The first non-dimensional ratio, the aspect ratio, is defined by the conveniently small dimensions of the ‘‘asthenospheric tank’’ (50x50 cm). The geologic structures under investigation extend, in map view, over thousands of kilometres ($\mathrm{L}$), and are often over a 100 kilometres thick ($\mathrm{H}$). Therefore an aspect ratio ($\mathrm{H/L}$) of 1/10 is also accorded to the modeled orogens that all measured over 30 cm long and 3 cm thick (dimensional controls further discussed in section 3.2.). The density scale is bound to the choice of water to embody the sub-lithospheric body. By using $H_2O$ as density standard and adjusting the paraffin weight through addition of clay powders (binding with the oil-based matrix via a water-in-oil surfactant; Boutelier & Oncken 2011), one can replicate the natural ratios between asthenospheric and lithospheric densities. The scaling of velocity (and of time) relies on a key parameter for Earth’s rheology: thermal diffusivity, the rate at which heat travels through specific materials. In nature, a balance prevails for the pace of heat diffusion

(lithosphere) and advection (asthenosphere), insuring a specific thermal budget in harmony with the lithospheric yield strength. Hence, the rate scale is empirically fixed by means of a dimensionless ratio $VH/\kappa$ equal to that in nature (Chemenda et al., 2000) where $\kappa$ is the thermal diffusivity parameter, $V$ is the velocity parameter (correlated to the time parameter by $V=t/H$) and $H$ is the length parameter. Likewise, calibration of the strengths ($\sigma$) can be achieved by referring to the dimensionless ratio: $\sigma / \rho * V^2$. Strain already being a dimensionless ratio (ΔL/L), strain localization (discussed in 2.2.2.) recorded in our models would bear the same proportions in nature. The large discrepancy in viscosity between the listhosphere and asthenosphere is well portrayed by using low-viscosity water as the asthenosphere's analogue. If one deducts a dimensionless ratio based on Jeffery's equation of viscosity (Jeffery, 1922), the modeled asthenospheric viscosity would be slightly depreciated compared to estimations for the planet (K. Lambeck et al. 1995; C.P. Conrad and M. D. Behn 2010; C. Doglioni et al. 2011). Nevertheless, these viscosity estimations are still being discussed and seeing as the focus of the study concerns mainly the lithospheric level, the viscosity approximation can be considered as valid (Boutelier and Chemanda, 2011).

The empirical parameters adopted in this study (presented in table 1) generate non-dimensional ratios (all of those discussed above) of the same order of magnitude as those estimated in nature, ensuring that the models are realist.

**Table 1. Empirical parameters scaled to nature**

| Parameter | Symbol | Unit | Model | Nature |
|---|---|---|---|---|
| Thickness of the lithosphere | $H_l$ | m | ~ 0.03 | ~ 105 000 |
| Density of the asthenosphere | $\rho_{asth}$ | $kg/m^3$ | 1000 | 3250 |
| Density of the upper crust | $\rho_{crust}$ | $kg/m^3$ | 860 | 2795 |
| Density of the cont. lith. mantle | $\rho_{cont.\ lith.}$ | $kg/m^3$ | 1000 | 3250 |
| Density of the oce. lith. mantle | $\rho_{oce.\ lith.}$ | $kg/m^3$ | 1000–1030 | 3250–3350 |
| Continental crust yield strength [a] | $\sigma_c$ | Pa | 18–43 | $2.05–5.7 * 10^8$ |
| Continental lith. mantle yield strength [a] | $\sigma_l$ | Pa | 27–43 | $3.07–5.7 * 10^8$ |
| Thermal diffusivity of the lithosphere | $\kappa$ | $m^2/s$ | $8 * 10^{-8}$ | $1 * 10^{-6}$ |
| Convergence Rate | V | m/s | $2.5 * 10^{-4}$ | $2.54 * 10^{-9}$ |
| Time | t | s | 92 | $3.15 * 10^{13}$ |

[a] Yield strengths throughout analogue materials decrease with depth in each layer; the table values represent the yield plastic strength averaged over the layer thickness.

### 2.2.2. Geotherm and Vertical Strength Profiles

The Earth has a hot core and a temperate surface. This confers to the bowels of the planet a vertical thermal gradient referred to as the "geotherm" (short for geothermal gradient). The strength profile of the lithosphere, a variation with depth of the lithospheric material yield strength, is greatly dependent on this geotherm. The thermo-dependent plastic yield strengths of paraffin materials are capable of replicating these natural lithospheric strength profiles. Measurements performed on a rheometer (Boutelier & Oncken 2011) showed that the most representative rheologic states of the paraffin plates are acquired in the thermal ranges of 40$^{o}$C. Thus, an electric heating element is built at the bottom of the tank, keeping the water at 40$^{o}$C. Above, a system of four infrared emitters keeps the surface of the paraffin plates at 36,5$^{o}$C, ensuring a linear "geotherm" for well-calibrated strength profiles. The heating systems are controlled by thermal probes and an auto-adaptive thermo-regulator (Boutelier and Chemanda 2002). Proper strength profiles ensure that the modeled lithosphere bends at depth and becomes more brittle closer to surface, as in nature (Byerlee 1978).

Model rheologies are calibrated according to lithospheric strength profiles extrapolated from laboratory measurements of natural rock strengths at typical plate tectonic P-T conditions (Goetze and Evans, 1979; Brace and Kohlstedt, 1980; Evans and Kohlstedt, 1995; Kohlstedt et al., 1995). Various tectonic configurations and geologic scenarios can be simulated via the layered consolidation of different lithospheric materials, depicting the elasto-plastic properties of the crust (weak and brittle) and mantle (strong and ductile). In cases where the stress regime surpasses the lithospheric material yield strength, compressional forces are accommodated by deformation. Strain-softening abilities will vary depending on the material modeled (e.g. crust vs. mantle), affecting the extent of lithospheric-scale strain localization (Boutelier and Oncken 2011). Near the surface, in the

brittle layer of the crustal environment, strain localization is a natural outcome of deformation. On the other hand, a more ductile regime prevails at the hot depths of the mantle where strain softening processes like dynamic recrystallization and shear heating take place (Poirier, 1980; White et al., 1980; Rutter and Brodie, 1988; Montési and Zuber, 2002; Hartz and Podladchikov, 2008). The latter regime and its softening behaviours remain under investigation; some argue that at the high temperatures of these depths, the lithospheric mantle has a low viscousity (Ranalli and Murphy 1987; Ranalli, 1997). Carefully calibrated strain-softening properties allow the initiation and progression of realistic lithospheric-scale strain zones and many other natural deformational features.

The yield stress and strain softening properties of the analogue materials can be measured via a rheometer. The curve derived from these data show that, at first, as shear stress increases, shear strain only rises lightly, in the linear fashion characteristic of an elastic material. This elastic domain only allows for limited elastic deformation (under 5% shear strain), as expected in natural rocks that rather have the tendency to permanently deform (strain localization). As the curve looses its linearity and starts to deflect toward the stress peak, it enters the plastic domain, where the deformation becomes irreversible. The curve climaxes at a stress level that is considered as the material yield strength. Once in the plastic domain, the strength decreases to less than half of the yield strength; the material has a strain softening behaviour (more than 50% softening), similar to what is expected in nature due to strain softening mechanisms like dynamic recrystallization and shear heating (Poirier, 1980; White et al., 1980; Rutter and Brodie, 1988; Montési and Zuber, 2002; Hartz and Podladchikov, 2008). The diagrams exposed in figure 2. show that the stress-strain curves of our materials are strongly thermo-dependent, as expected in nature, but are independent from the shear-rate, a behaviour highly characteristic of elasto-plastic materials (in contrast with visco-plastic materials) (Boutelier and Oncken 2013).

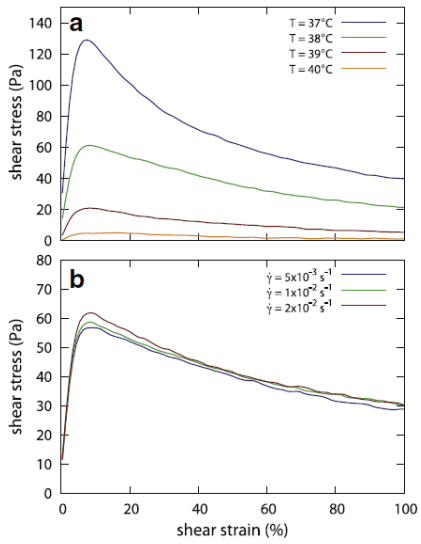


**Figure 2. Two stress-strain diagrams plotted to show the rheologic properties of the analogue materials. Testing performed on a rheometer records a steep stress increase for little strain in the initial elastic domain (linear part of the curve), prior to ductile plastic deformation and failure. As the curve reaches its climax, it exceeds the material yield strength, which is thermo-dependent. Passed that peak, a thermo-dependent strain softening behaviour is observed (softening down to 50 % and more). (A) Curves of a constant shear rate ($\delta\gamma/\delta t = 10^{-2}\ s^{-1}$) for varying temperatures. (B) Curves of a constant temperature (38°C) for varying shear rates. (after Boutelier et al. 2013)**

### 2.2.3. Geometric configuration

The geometric configuration of continental ribbons is an issue when modelling oroclines. Variations in dimension and shape (e.g. **Fig. 3**) of the ribbons alter the extent and nature of deformation. To investigate what promotes or prevents vertical axis rotation of a continental ribbon, the main geometric aspects explored in this study are 1) the width-thickness ratio, 2) the bending wavelength (length-width ratio), 3) the crustal extent and 4) the presence of tapered corners.

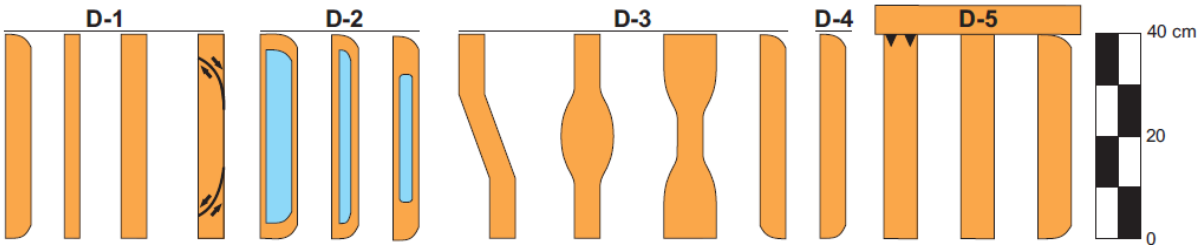


**Figure 3 Scaled sketch of ribbon surface geometries experimented with in the D-series. *Orange*: Lithospheric mantle material *Light blue*: Continental crust.**

### 2.3.4. Neighbouring plates and boundary control

To assess mountain belt behaviour and buckling requirements, the simplest tectonic scenario is a laterally unconstrained ribbon. For this purpose, elongated lithospheric continents were built, deposed at the surface of the "asthenospheric tank" and subjected to a parallel stress field (D-series). The lateral freedom involved in these basic models promotes vertical axis bending and helps to study the buckling mechanism at its source. As instructive as these model approximations might be, they do not provide us with the complete story about the surrounding tectonic arrangement required to give rise to an orocline. Therefore, additional paraffin mountain belts were built, but this time escorted by other paraffin plates along their margins. It stands to reason that, just as potential natural tectonic scenarios, the possible modelling configurations are countless. The composition (continental vs. oceanic) and dimensions of the adjacent plates is investigated, as are the types of boundaries between them and the continental ribbons. In this study, this boundary control takes various forms, including subductive and collisional convergent boundaries, transform faults and incipient ridges.

**Table 2. The 34 analogue models driven for this study can be categorized into four distinct empirical series.**

| Series | Description |
|---|---|
| **A** (3 ribbons) | A low-density crustal ribbon is mounted on a lithospheric mantle plate and orthogonally subjected to the compressional regime of a subduction zone (pre-existing thrust fault). |
| **B** (2 ribbons) | A continental lithospheric ribbon is bordered by two other paraffin plates. The mobile piston forces the three plates to converge towards a subduction zone (pre-existing thrust fault) carved into a fourth "overriding plate". |
| **C** (14 ribbons) | A continental lithospheric ribbon is bordered by one or two other paraffin plates. The mobile piston forces compression of the ribbon and (in some experiments) of the adjacent plate(s) against the stationary back-wall. Analogue to the tectonic environment of a collisional scenario. |
| **D** (15 ribbons) | A continental lithospheric ribbon rests at the surface of the 'asthenospheric tank', without any lateral constraints, and is subjected to a parallel compressional regime. The simplicity of these experiments helps to observe and study the basic deformations and mechanisms in oroclinal systems, from initiation of the curvature to complete closure of the limbs. |

***See the results (table. 3) for further information on each individual experiment**

*Chapter 3*

# 3. Results

The 34 model runs conducted in this study exhibited an array of results (**Table 3**). First, the common deformational structures are summarized (section **3.1**). Next, unique deformational responses dependent on specific parameters are described, such as geometry of the initial orogen (section **3.2**), the crustal component (section **3.3**) and boundary control (section **3.4**). Finally, a number of models were designed to recreate specific tectonic scenarios, notably a complete interlimb closure (section **3.5**), a magmatic arc (section **3.6**) and a triple junction (section **3.7**).

## 3.1 Frequent Deformational Structures

### 3.1.1. Differential thickening

Thickening is the first and most basic empirical response when any modelled ribbon is compressed parallel to its long axis. At the early stages of each experiment, activation of the piston induces thickening, especially at the collisional contacts of the shortening plates (piston and back wall). Thickening is observed where peaks of convergence are recorded (via P.I.V. analysis; e.g. shown in **3.5** and **3.7**). Thickening can only allow a limited extent of shortening, after which another strain system takes the lead. In cases with a surplus of stress and where material accumulation is excessive for isostatic balance, lithospheric failure occurs (thrust belts, subduction zones or transpressional systems) adjacent to thickened zones. In cases where oroclinal buckling of the continental beam prevails, the inner hinge experiences further thickening while the outer arc undergoes thinning. Cross-sections of a ribbon buckling upon full limb closure showed up to 90% inner-arc thickening and 43% of thinning at the outer arc (**D-4**).

**Table 3. Experimental results**

| Exp. | Comp. Regime | Initial Lateral Boundaries | Coupling with Crust | Geometric Specifics | Deformation |
|---|---|---|---|---|---|
| A-1 | Subd. | -N/A- | Molded within lith. plate | | Lith. : subduction<br>Crust : wedges at subd. boundary + lateral extrusion |
| A-2 | Subd. | -N/A- | Deposed on lith. plate | Initially curved crustal ribbon | Lith. : subduction<br>Crust : wedges at subd. boundary + lateral extrusion<br>+ localized block rotation |
| A-3 | Subd. | crustal ribbon adjacent to side wall (trans.) | Extra-low coupling horizon | | Lith. : subduction<br>Crust : wedges at subd. boundary + lateral extrusion |
| B-1 | Subd. | R. : cont. overthrust<br>L. : cont. underthrust | Molded within lith. rib. | | Lith. rib. : subduction along with the rest of lith. material<br>Crust : wedges at subd. boundary + lateral extrusion |
| B-2 | Subd. | R. : oce. underthrust<br>L. : oce. underthrust | Molded within lith. rib. | Initially curved lith. ribbon and crust | Lith. rib. : subduction along with the rest of lith. material<br>Crust : wedges at subd. boundary + lateral extrusion |
| C-1 | rib.: coll.<br>oce.: subd. | R. : cont. trans.<br>L. : oce. underthrust | -N/A- | | Lith. rib. : double subduction (at both extremities)<br>Oce lith. : subduction |
| C-2 | rib.: coll. | R. : oce. underthrust | -N/A- | t.c. | Lith. rib. : curvature initiates + hinge overthrusts the oce. lith.<br>+ differential thickening + extension faults at outer arc<br>+ late-stage large-scale trans. |
| C-3 | rib.: coll. | R. : oce. underthrust<br>L. : cont. trans. | -N/A- | t.c. | Lith. rib. : subduction<br>Cont. & Oce. lith.: No deformation |
| C-4 | rib.: coll. | R. : cont. trans. | -N/A- | t.c. | Lith. rib. : double subduction (both extremities) |
| C-5 | rib.: coll. | R. : oce. underthrust<br>L. : cont. i.r. | -N/A- | t.c. | Lith. rib. : curvature initiates + hinge overthrusts the oce. lith.<br>+ differential thickening + extension faults at outer arc<br>+ interlimb basin extension + late-stage large-scale trans. |
| C-6 | rib.: coll.<br>oce.: subd. | R. : cont. i.r.<br>L. : oce. underthrust | -N/A- | t.c. Triple junct. at the ribbon's mid-length | Lith. rib. : early shortening accommodation via 4 centers of rotation<br>+ late-stage thrust system + triple curvature of lith. roots.<br>+ differential thickening<br>Oce. lith.: subduction + late stage slab breack-up |
| C-7 | rib.: coll.<br>oce.: subd. | R. : oce. underthrust | -N/A- | t.c. Lith. rib. initially L-shaped ($90^0$ angle) | Lith. rib. : buckles and collides on the orthogonal arm of the "L"<br>+ differential thickening + extension faults at outer arc<br>*Experimental failure*: oce. plate fell down mid-experiment |
| C-8 | rib.: coll.<br>oce.: subd. | R. : cont. i.r.<br>L. : oce. underthrust | -N/A- | t.c. Same as C-6, new batch of oce. lith. | Lith. rib. : early shortening accommodation via 4 centers of rotation<br>+ late-stage thrust system + triple curvature of lith. root |

| | | | | | |
|---|---|---|---|---|---|
| | | | | | + differential thickening<br>Oce. lith.: subduction *same results as C-6 : new batch reliable* |
| C-9 | rib.: coll.<br>oce.: subd. | R. : oce underthrust<br>L. : oce i.r.+ trans.<br>(L-shaped around rib) | Molded within lith. rib. | t.c. Lith. rib. Initially L-shaped ($90^0$), same for oce. plate on the left | Lith. rib: initiates thrust system + curvature of lith. roots.<br>Crust: lateral and frontal extrusion covering large area<br>Oce rib: -R.- subducts under rib. -L.- coll. compression |
| C-10 | rib.: coll.<br>oce.: subd. | R. : cont. i.r.<br>L. : oce underthrust | -N/A- | t.c. Triple junction near the back wall | Lith. rib. : subduction initiates at triple junction<br>Oce. lith. : subduction |
| C-11 | rib.: coll.<br>oce.: subd. | R. : cont. i.r.<br>L. : oce underthrust | -N/A- | t.c. Same as C-10 but thicker lith. rib. | Lith. rib. : large-scale diagonal trans. initiates at triple junction<br>Oce. lith. : subduction |
| C-12 | rib.: coll. | R. : oce underthrust | -N/A- | t.c. Narrow oce. plate | Lith. rib. : subduction initiates near back-wall |
| C-13 | rib.: coll.<br>oce.: subd. | R. : cont. i.r.<br>L. : oce underthrust | -N/A- | t.c. Triple junction near the back wall | Lith. rib. : subduction initiates at triple junction<br>Oce. lith. : subduction |
| D-1 | rib.: coll. | -N/A- | -N/A- | 4 ribbons<br>Dimension control | Lith ribbons: buckling + extension faults at outer arc<br>+ differential thickening<br>+ (late-stage) bends interfere with each other<br>+ Thicker ribbons force others aside |
| D-2 | rib.: coll. | -N/A- | #1 High<br>#2 Medium<br>#3 Low | t.c. 3 ribbons<br>Crustal control | Lith ribbons: buckling + extension faults at outer arc<br>+ differential thickening + asymmetric dynamics<br>+ (late-stage) bends interfere with each other<br>Crust: Follow the lith. ribbons + upward extrusion for #1 & 2<br>+ "pinch down" for #2 (cross-sections) |
| D-3 | rib.: coll. | -N/A- | -N/A- | 4 ribbons<br>Shape control<br>(see Fig.3) | Narrow section in the ribbon favours trans. formation<br>Wide sections in the ribbon resist buckling<br>2 opposed t.c. initiate a double buckle, one eventually takes the lead |
| D-4 | rib.: coll. | -N/A- | -N/A- | t.c.<br>Full limb closure scenario | Lith ribbons: buckling + extension faults at outer arc<br>+ differential thickening + coll. of the limbs<br>+ thrust system along the limbs' contact<br>+ (late-stage) trailing limb overthrusts the leading limb |
| D-5 | # 1 coll.<br># 2 coll.<br># 3 subd. | -N/A- | -N/A- | 3 ribbons<br>Comp. Regime control<br>#1 t.c. | # 1 & 2 : buckling + extension faults at outer arc<br>+ differential thickening<br>+ (late-stage) bends interfere with each other<br># 3 : subduction |

R. = Boundary on the right
L. = Boundary on the left
Comp. Compressive
rib.= Ribbon
coll.= Collisional
subd. = Subductive
Lith. = Lithospheric mantle
cont. = Continental
oce. = Oceanic
trans. = Transform fault
i.r. = Incipient Ridge
t.c.= Tapered corners

### 3.1.2. Thrust Belts

Under highly compressional regimes, thickening occurs along with thin- to thick-skinned thrust belts. Shallow thrust systems commonly form next to the collisional contacts and, in cases with buckling, at the inner hinge of the orocline. Deeper thrust faults are also found. For example, upon complete limb closure of a buckling continental ribbon, the interlimb contact undergoes peaks of compression, and the intense thickening occurs along a system of thrusts (thrust belt) that accommodates some of the compression. As the piston pushes further, a single thrust fault takes the lead and bisects the entire lithosphere (**D-4**). These large-scale thrust faults (**C-1**; **C-10**; **C-13**), either blind or apparent, can accommodate large amounts of shortening and facilitate lithopsheric root delamination. They preferentially initiate next to "weak zones", notably in the vicinity of a triple junction (see section **3.7**). These thin- to thick-skinned thrusts are detectable through P.I.V. computing of relative convergence at the surface of the models, showing as blue lines of convergence (e.g. in section **3.5** and **3.7**).

### 3.1.3. Extensional systems

Even though all the models were subjected to a compressional regime, extensional systems were commonly recorded. For example, ribbons that undergo vertical axis buckling systematically display an extensional regime at the outer arc. In such cases, divergence (measured via P.I.V. analysis of the models' surfaces; experiment **D-4**) at the outer arc is concurrent with lithospheric stretching and thinning of the outer margin of the buckling ribbon. Extension faults are found all along the outer arc, radiating around the hinge and tangential to the ribbon's border (**D-4, C-5**). Where the limbs of buckling continental ribbon move away from an adjacent plate, an interlimb gap or basin is formed (**C-5**). This gap exposes the asthenosphere (water) implying that, in a natural environment, asthenospheric mantle material would rise and fill such a gap building a new lithospheric floor as the basin opens. If the ribbon buckles to the point of full limb closure, the interlimb basin eventually

seals completely (**D-4**). For models where buckling does not prevail, small-scale transpressional basins form in zones of shear movement between lithospheric plates. A rarely observed extensional system is found where compression climaxes (P.I.V. inquiry: **D-4**). In response to overthickening in the inner hinge, material extrudes at the surface, radiating away from the topographic and compressional summits. Redistribution of extrusive material is greater within the crustal lithosphere but can also be sustained within the lithospheric mantle.

## 3.2. Geometric Control

The geometric configuration of the continental ribbons was studied via variation of the continental beams' length, width and thickness ratios. Results show that as the length/width ratio of the continental ribbon increases, its bending wavelength decreases. This consequently increases the bending ability and the potential for multiple oroclines. The narrower the ribbon gets, the greater it will bend, although if a ribbon is too narrow it is more likely to experience lithospheric failure along transpressional fault systems (**D-3**). Thickness plays a similar role: too thin a ribbon will easily fail and initiate a thrust system. The strength of a thin ribbon is further reduced as its sharper thermal gradient makes the continental beam hotter (weaker, more ductile) at shallow depths. A thick and strong continental prism, on the other hand, has the ability, as it buckles, to deform adjacent plates (**D-1; D-3; D-5; C-6; C-8**) or even force them to subduct (**C-2; C-5**).

Given perfectly rectangular continental prisms (D-1), vertical axis bending prevails as the response to long-axis parallel compression. It proved impossible to predict the buckling direction of symmetrical ribbons; at first the ribbons shorten and thicken slightly at the collisional contacts (next to the piston and back-wall) before arbitrarily initiating a buckle to one side or the other. The pre-buckling thickening and the unpredictability of the bending orientation can both be obviated with the implementation of curved tapered corners (see ***"t.c.".*** in the "specific geometries" column of **Table 3**) at the beam's two collisional

contacts). With curved tapered corners, allowing differential forcing, rotation of the limbs is recorded at the very initial stages of shortening (P.I.V. analysis; **Fig. 4**). In the variant where these curved corners are carved oppositely (last ribbon of **D-3**; **Fig. 3**), a "coupled orocline" initiates (**Fig. 4**), and will progress, provided the bending wavelength is short enough (high length/width ratio). A ribbon with a longer wavelength (wider ribbon) can still initiate a double bend, but only one of the two bends (the one next to the back-wall) will reach full interlimb closure. At the surface of the latter ribbon, P.I.V. calculations of relative rotation show three distinct centers of rotation for the coupled orocline (**D-3**; **Fig. 4**) whereas a single buckle features only two centers (**D-4**; **Fig. 4**). These experiments help us to resolve the basic force systems and geometric requirements to initiate individual or multiple buckles.

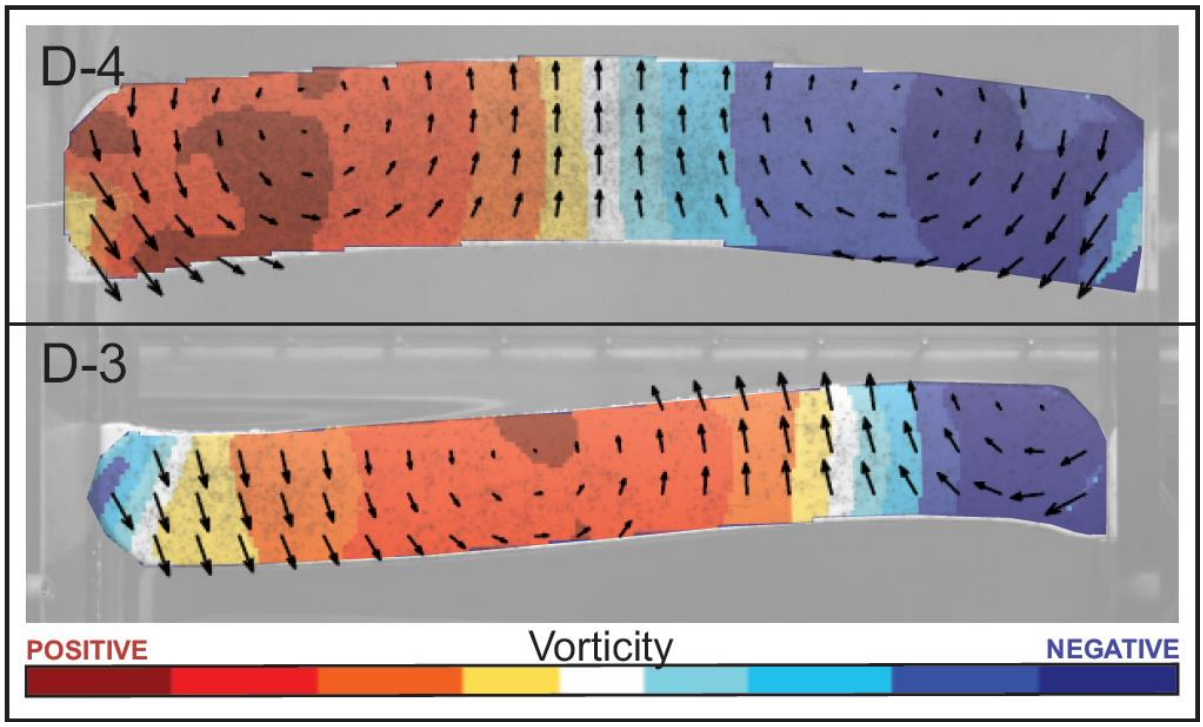


**Figure 4. P.I.V. calculations of rotation at the surface of the models from experiments D-4 and D-3. The experiments involve a compressed continental beam with tapered corners at both ends. For D-4, the tapered corners are apposed symmetrically; compression of the piston promotes a simple buckle with two centers of vorticity mid-length on both rotating limbs. One limb rotates counter-clockwise (Red) and the other clockwise (Blue). The continental ribbon from D-3 has oppositely oriented tapered corners providing the differential forcing required for a coupled orocline, covalent with three distinct centers of vorticity, one in the middle of the ribbon (CCW-Red) and one at each extremity (CW-Blue).**

### 3.3. Crustal Component

At the surface of our planet, the silica-rich crust has distinctive properties (density, elasto-plasticity, yield strength, etc.) that distinguish it from the underlying mafic mantle. The compositions of the experimental hydrocarbon analogues are adjusted to properly portray these specific crustal attributes. Experiments from the A-Series and B-Series were conducted to study the deformation of elongated ribbons with a continental crust as they are subducted along a trench perpendicular to the ribbon (referred to throughout as 'crustal ribbons'. Results show that in such compressional regimes (**Fig. 5**), the buoyancy of the crustal ribbons forces the crust to detach from the subducting mantle lithosphere and to wedge itself into the converging boundary. As crust accumulates at this ''accretionary wedge'', excess material escapes at the surface, yielding lateral extrusion (**Fig. 6**). Similar weak and strain-localized crustal behaviour was commonly observed in our experiments. The crust proved too week to propagate the compressional stress throughout the rest of the crustal ribbon. We conclude that lithospheric mantle has to be involved in the formation of secondary oroclines, as the crust on its own is too weak to buckle.

This type of crustal response (**Fig. 5**) is recorded in all experiments, whether the crustal ribbon was [A] moulded into the lithospheric mantle plate, [B] deposed next to the tank's side wall (analogous to a continental transform) or even [C] bounded by pre-existing thrust faults. In the latter model, the thrust belt structure parallel to the crustal ribbon is designed to allow lateral freedom and facilitate sideways buckling movement. Yet, even so, the crustal material wedges itself into the converging boundary and reacts in a strain-localized and extrusive manner.

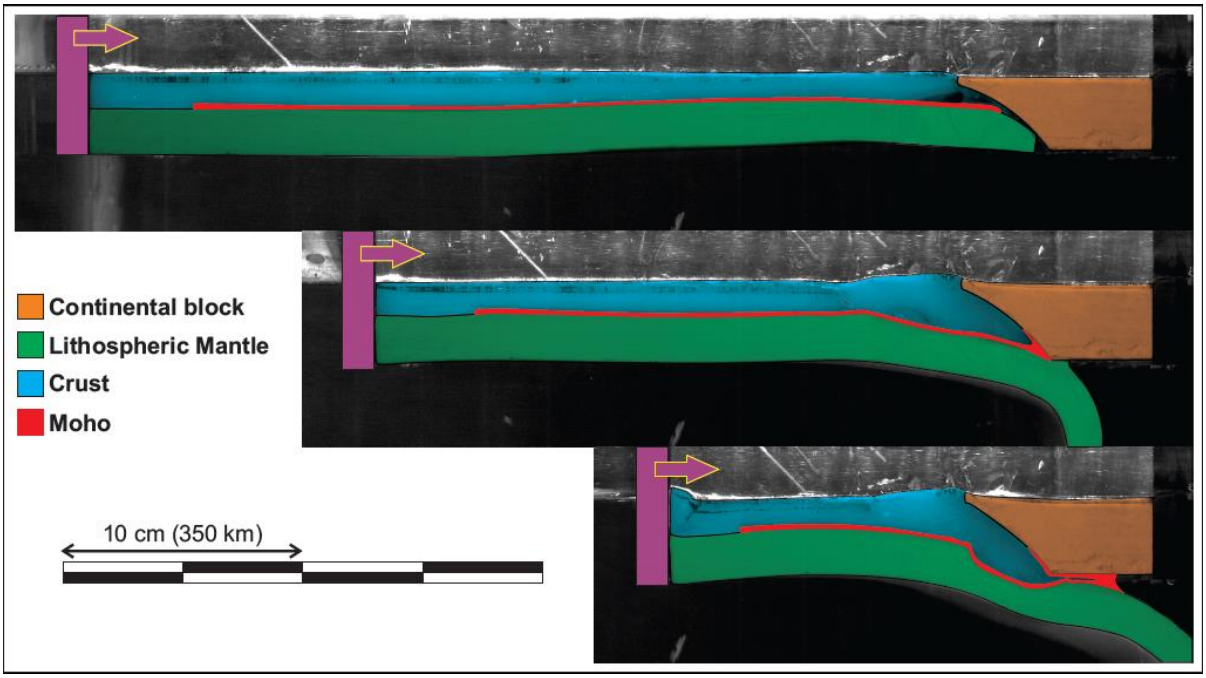


**Figure 5. Pictures from the side wall (equivalent to cross-sections) of model A-3 at initial-, mid- and late-stages. The piston [purple] pushes the lithospheric mantle plate [green] and its crustal ribbon [blue] against an overthrusting continental block [orange]. At the Moho [red] a thin substratum of weak material operates as low-coupling horizon between the crustal beam and the mantle plate. The buoyant crust wedges and thickens at the boundary and extrudes at the surface but does not subduct with the underlying mantle plate.**

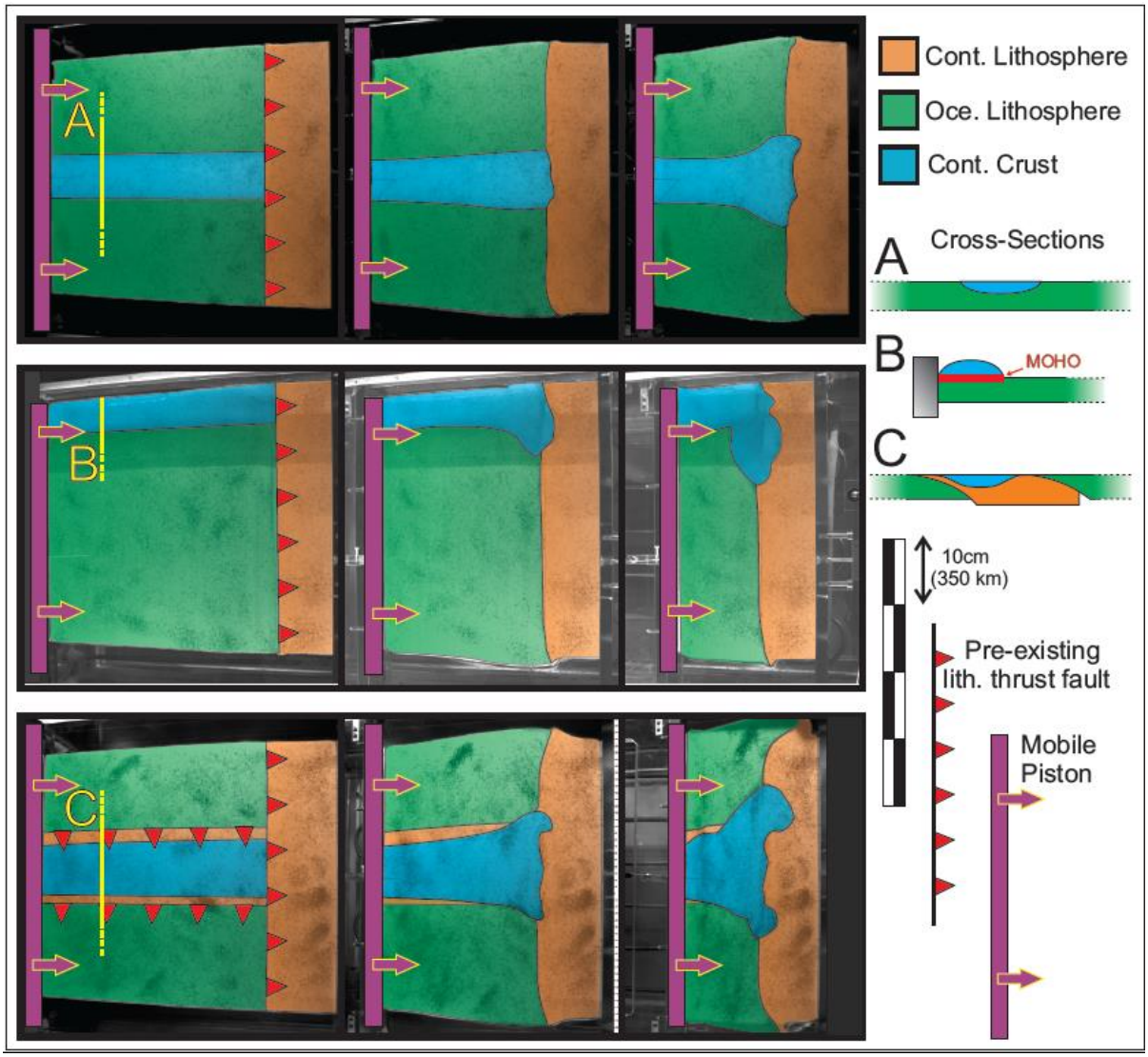


**Figure 6. Surface pictures of experiments A-1 [A], A-3 [B] and B-1 [C] at initial-, mid- and late- stages. The models all involved a crustal ribbon [light-blue] subjected to the compressional regime of a subduction zone. Upon advancement of the piston [purple bar] the oceanic lithosphere is forced to subduct at the pre-existing thrust fault [red-toothed line]. Concurrently the buoyant crust wedges itself into the converging boundary. After substantial crustal accumulation at the boundary, the crust undergoes lateral extrusion at the model's surface; practically no crustal material gets subducted with the underlying mantle. The yellow lines are the surface projections of the cross sections presented in the legend.**

Experiment D-2 (**Fig. 3**) studied various crustal beams moulded over continental mantle ribbons, and showed that under compression, the overlying crustal layer harmoniously follows the buckling underlying mantle beam. Upon full limb closure, the compressional regime leads to crustal thickening and upward extrusion. When the crust thickens in a region, the extra mass results in sinking of the lithospheric mantle. Afterwards, isostatic equilibrium tends to redistribute the material overload laterally, resulting in a relative thinning of the lithospheric mantle under the crustal accrual. Similar thinning occurs under crustal ribbons and acts as a longitudinal zone of weakness making the orogen analogues more susceptible to lithospheric failure. In these experiments, failure initiates around the inner hinge (where compression peaks) and then propagates outward, principally in the trailing limb (piston side) of the buckling crustal ribbon, where a crustal ‘‘pinch down’’ can be observed in cross sections of the model. Such a feature is the aftermath of the activation of a “lithospheric thrust” forcing the leading limb of the buckle under the trailing one (similar to the thrust from **D-4,** section **3.5**). This important dichotomy within the continental beam is evident when looking at the bottom of the lithospheric root, where “mantle delamination” (blind thrust) initiates to accommodate the material overload that developes beneath the inner hinge of the orocline.

The natural coupling at the MOHO, interface between crust and mantle, may vary depending on the presence of fluids, intrusions or other geologic structures. At the Moho of some of our models, a low strength MOHO was modeled through the application of paraffin oil or a thin low-strength paraffin substratum along the crust – mantle boundary (red layer in **Fig. 5**). The crust above a low-strength MOHO was more inclined to detach and/or deform independently from the mantle (low coupling). To recreate a strong coupling at the MOHO, the setup of some models was done by pouring hot mantle material (paraffin analogue pre-heated over its melting point) directly over the cold-solid beams of crustal material. The heat of the melted mantle provided for a strong cohesion with the crust on which it is poured. In such models, a minor amount of crustal material gets dragged down with the subducting slab. A small extent of crust is subducted because of its tendency to

infiltrate extension cracks that sometimes develop in the uppermost lithospheric mantle of the subducting slabs as the slab bends downward into the trench.

Oceanic lithosphere has a thin crustal layer. In our models, this negligible layer is omitted. Indeed, many models (**Fig. 5**) show that the crustal layer has a negligible affect on the behaviour of the underlying lithospheric mantle, closely following the underlying lithosphere during deformation. As the crustal material can mask (for P.I.V. analysis) the exact deformation of the underlying lithosphere, we considered the same approximation (obviated crust) valid for experiments conducted with the intention of qualitatively investigating deep lithospheric-mantle dynamics.

### 3.4. Boundary control

The design of accurate analogue models requires that deformation take place within a valid tectonic setting. This study explored various scenarios by varying the continental ribbons' tectonic margins and the nature (oceanic or continental) of the adjacent plates.

The oceanic and continental mantle analogue materials share practically the same yield strength. The two types of paraffin plates mostly differ in thickness and density. In general, the thin and dense oceanic lithosphere plates showed a better ability to subduct. These plates experience stronger slab pull and can occasionally achieve slab break-up (**C-6**). Moreover, thinner plates also yield a sharper thermal gradient, further weakening the lithosphere. On the other hand the thicker and more buoyant continental plates are less inclined to subduct and can endure a greater amount of strain and thickening before lithospheric failure initiates. In the case of a continent-continent collisional boundary, lithospheric failure takes the form of a large thrust allowing one plate to underthrust the other. The underthrusting plate does not sink toward the bottom of the asthenosphere like an oceanic slab, but rather hangs on to the lithospheric root of the overlying plate. In general, a thicker plate will overthrust a thinner one during collision.

The margins of modeled continental ribbons can embody various types of tectonic boundaries. In our experiments, deformation was facilitated by the presence of lubricated (paraffin oil), pre-existing fault planes along the ribbon margins. In this study, the ribbon boundaries experimented with were 1) thrust faults 2) vertical faults 3) incipient ridges and 4) total lateral freedom.

### 3.4.1. Thrust faults

In the case of a continental ribbon that initially overthrusts an adjacent plate, the buoyant ribbon has a greater aptitude to buckle and migrate in that direction. The underlying plate, especially if oceanic in nature, is inclined to sink under and subduct beneath the thick buoyant continental beam. In general, thin lithosphere is easier to overthrust and deform, but in the case of thicker and heavier oceanic plates, a stronger slab-pull can be experienced, and could potentially promote further migration of the orocline hinge toward this sinking oceanic slab. Additional experiments revealed that thrust faults along the inner margin of a buckling ribbon did not help facilitate the opening of an interlimb basin. The interface tension detected at the pre-existing thrust boundary proved excessively strong and restrained buckling initiation toward the opposite side (**C-12**).

### 3.4.2. Vertical Faults

Vertical, or “transform” faults, are fashioned along ribbon margins to allow horizontal shear motion relative to the neighbouring plate. To activate such a boundary, the piston has to compress the ribbon but not the adjacent plate, allowing strike-slip relative plate motion. A similar analogue for a transform fault is produced when the mobile paraffin plates are aligned next to the stationary side wall of the tank (e.g. **A-3**; **Fig. 5** & **Fig. 6**). Our models show that the interface tension at along a vertical fault is too strong to allow extensional opening of an interlimb basin and hence prevents orocline formation, even if

the ribbon has tapered corners and is laterally free on the opposite side from the vertical fault (C-4).

### 3.4.3. Incipient Ridges

A plate boundary characterized by thinned lithospheric margins, modeling an incipient ridge, was employed on some models (e.g. in section **3.6**). These thinned boundaries are thought to be analogous to boundaries underlying natural basins located behind magmatic arcs (back arc basins). The thinned margins forms zones of weakness that facilitate the lateral displacement required to open the interlimb basin during oroclinal buckling. The incipient ridge opens instantly upon initiation of buckling and the resulting basin can grow to widths of hundreds of kilometres. Where continental ribbons buckled toward an incipient ridge boundary (**C-6**), the thin lithosphere rapidly developed substantial plastic strain (system of small-scale thrusts). Incipient ridges can also accommodate shear movement between two plates. To simulate such dynamics, the piston is placed up to the edge of the incipient ridge and is directed orthogonally to it. Provided the piston compresses the continental beam and not the adjacent plate, strike-slip motion is activated. This relative motion is also monitored via P.I.V. calculation of the rotation at the surface of the model, where the shear displacement is recorded as a clockwise rotation over the incipient ridge boundary (**C-6, C-11, C-13**). Small scale transpressional basins can also develop along boundaries during shear motion (see section **3.7**).

### 3.4.4. Lateral Freedom

To study the very basics of buckling, some experiments involved continental ribbons with no lateral constraints. These ribbons are placed at the surface of the asthenosphere (water) and subjected to long axis parallel compression via displacement of the piston positioned orthogonally to the continental beams. Most of these models are from the D-series and expressed textbook examples of lithospheric oroclines with their differential

thickening, centers of vorticity, and thrust and extension faults. These models are geometric simplifications; nonetheless, they can be compared to a scenario where the thick continental beam can freely overthrust the surrounding lithosphere. Similar simplification of the boundary conditions were employed in other modeling studies (Pastor Gàlan 2012; Johnston 2004).

### 3.5. Full interlimb closure scenario

Pure oroclinal mechanisms were investigated in an experiment featuring a single continental beam compressed to the point of buckling and complete limb closure. The ribbon (**Fig. 5** [1]) is laterally unconstrained, allowing full sideward freedom. The direction of flexing is predetermined in the ribbon by virtue of a pair of tapered corners carved at the collisional contacts (piston & back-wall). At the early stages, these two collision localities experience minor deformation, including the formation of thin-skinned thrust faults that accommodate modest thickening of the lithosphere. The first large-scale response to ribbon-parallel compression is the initiation of vertical axis bending. The hinge is localized at the ribbon's mid-length, conferring a set of symmetrical limbs that rotate toward each other. P.I.V. calculations of average displacement show two rotation centers at the middle of each rotating limb. The buckling nearly accommodates all of the shortening prior to limb closure. The ongoing flexing motion is recorded at the surface (relative motion vectors (**Fig. 4**; **D-4**)). The deformational grid (**Fig. 5** [2]) computed through analysis of the markers progression shows intense convergence (blue) at the inner hinge along with extension (red) around the outer arc. These converging and diverging zones correlate to the major compressional and extensional systems, respectively. At the early stages, the compressed inner hinge is preferentially thickened and a small-scale thrust system developes at the surface oriented perpendicular to compression. P.I.V. analysis also show that, as the model is compressed, the centre of rotation on each limb, observed via the black relative displacement vectors and vorticity calculations (**Fig. 4**), progressively migrates toward the axial plane of the buckle.

Ultimately, the limbs collide, progressively sealing the 'interlimb basin' like a zipper closing the orogen arms on themselves. Once the two limbs are contiguous, buckling is no longer an option and continued shortening is accommodated by deformation of the joined limbs.. At first, compression at the limbs' interface forces intense thickening, indicated by the P.I.V. analysis of relative displacement recording convergence scattered over the collision area. Thrust faults initiate around the inner hinge and propagate down the limbs, pursuing the excess of material accumulation at the collisional vicinity. This system of surface thrusts strike parallel to the interlimb boundary and assumes some of the convergence until compression peaks (as recorded with the force captor), when one of these sub-horizontal thrusts perforates through to the lithospheric root, the trailing limb (piston side) then overthrusts the leading limb (back-wall side). Late-stage deformation P.I.V. calculations show dissipation of the convergence everywhere on the plate except at the locality of the new major longitudinal thrust (**Fig. 8** [3]).

Cross-sections (**Fig. 7** [3]) of the cold-solid model at its final stage confirm the presence of a lithospheric-scale thrust dipping $45^0$ toward the trailing limb. Thickness measurements reveal an increase from 3.0 cm to 5.7 cm at the inner hinge, a 90% thickening. Divergence was recorded immediately over this thickened zone, and is explained as a result of isostacy causing the material overload to extrude at the surface. Around the outer arc, 43% thinning takes place with lithospheric thickness dropping to 1.7 cm from 3 cm. This thinning is accommadated by a series of radial extensional faults at the surface.

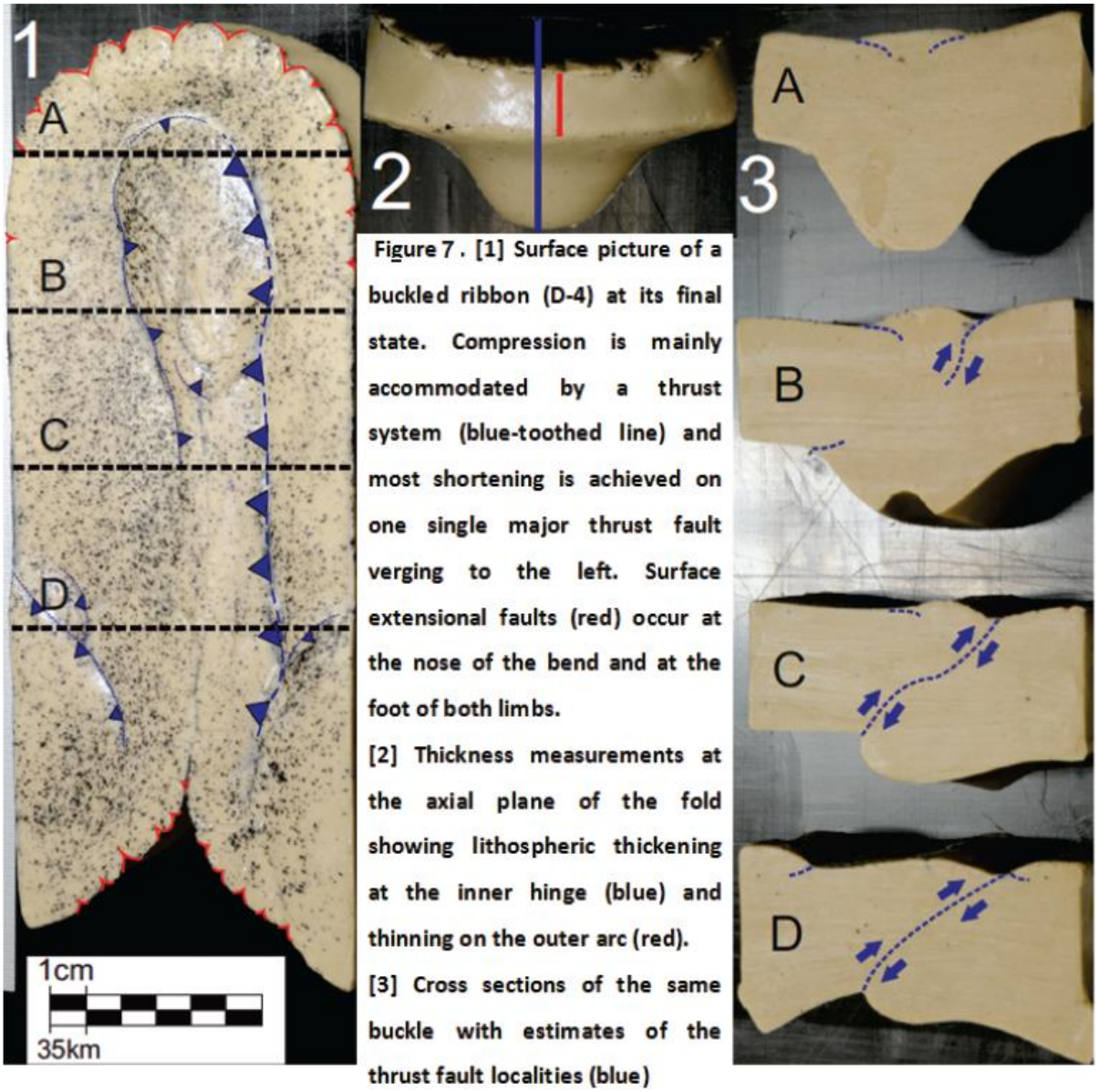


Figure 7 . [1] Surface picture of a buckled ribbon (D-4) at its final state. Compression is mainly accommodated by a thrust system (blue-toothed line) and most shortening is achieved on one single major thrust fault verging to the left. Surface extensional faults (red) occur at the nose of the bend and at the foot of both limbs.

[2] Thickness measurements at the axial plane of the fold showing lithospheric thickening at the inner hinge (blue) and thinning on the outer arc (red).

[3] Cross sections of the same buckle with estimates of the thrust fault localities (blue)

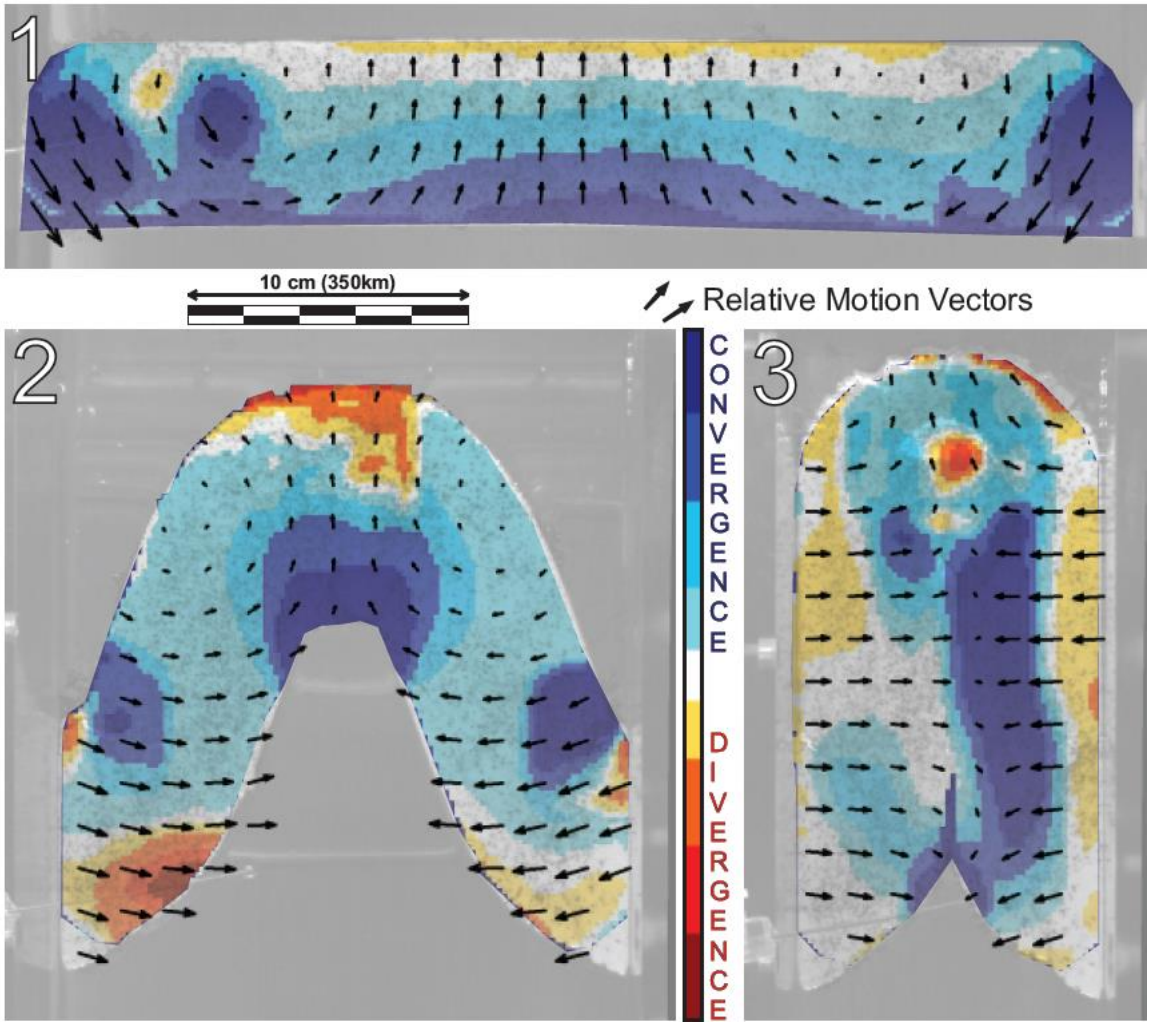


**Figure 8 Deformation at the surface of a buckling lithospheric ribbon (D-4) computed via P.I.V. technique. Relative motion vectors (black arrows) show symmetrical rotation of the limbs toward each other [1 & 2]. Strain calculations express [2] convergence (Blue) at the inner hinge until closure of the limbs, after which the convergence focalizes over the interlimb contact [3] as a thrust system develops parallel to it (thick blue line). The same calculations show that before limb closure, divergence (Red) is mainly localized at the outer arc of the bend and at the foot of the two limbs. After closure, the main divergence detected is at the inner hinge where an extrusive surface system discharges the material overload radiating away from the topographic high. See the video attached in the appendices for an overview of the entire experiment.**

## 3.6. Magmatic arc scenario

Some experiments (from the C-series) were conducted with the specific objective of modelling compression of a continental ribbon with a magmatic arc geometry, including a subduction zone along one margin, and a "back-arc basin" along the opposite margin. The empirical initial configuration is designed accordingly (**Fig. 9** & **Fig. 10** [1]): the continental ribbon overthrusts a thin oceanic plate on one side, and on the other side an incipient ridge is carved under the ribbon's boundary with a third, stationary, continental plate. In nature, such lithospheric thinning at the back of the arc is common, especially where the subducting slab rolls-back. This tectonic configuration is one of the most common producer of continental ribbons, the backbone of any orocline. Japan consists of a typical example of such configuration, where the roll back and slab pull were strong enough to open the back arc basin under the Japan sea. (Tatsumi, Yoshiyuki, et al. 1989)

As the piston compresses the ribbon along its long axis, a wide range of deformation mechanisms accommodate shortening. Empirical outcomes are early stage thickening and minor surface thrust faulting (**Fig. 10** [2]) at the collisional contacts (see **3.1.1.**). An interlimb basin opens behind the rotating leading limb, a sign of the vertical axis flexing at the very early stages; P.I.V. analysis confirms limb rotation. Progressive advancement of the piston forces differential displacement between the mobile trailing limb and the adjacent, stationary continental plate. Hence, the incipient ridge boundary becomes the locus of relative shear motion via a dextral strike-slip fault. With further shortening (**Fig. 7** [3]), the ribbon develops significant curvature toward the oceanic lithosphere, which is forced to subduct under the hinge of the bend. Concomitantly, extension of the interlimb basin exposes over 5 cm (the equivalent of over 175 kilometres) of asthenosphere [water in our models]. Ultimately (**Fig. 7** [4]), once the trailing limb has undergone enough rotation and the angle between the compression axis and the strike of the limb has grown sufficiently, the continental ribbon ruptures and a strike-slip fault bisects the ribbon and facilitates extrusion of the trailing orocline limb into the interlimb basin; at that point buckling has ceased completely.

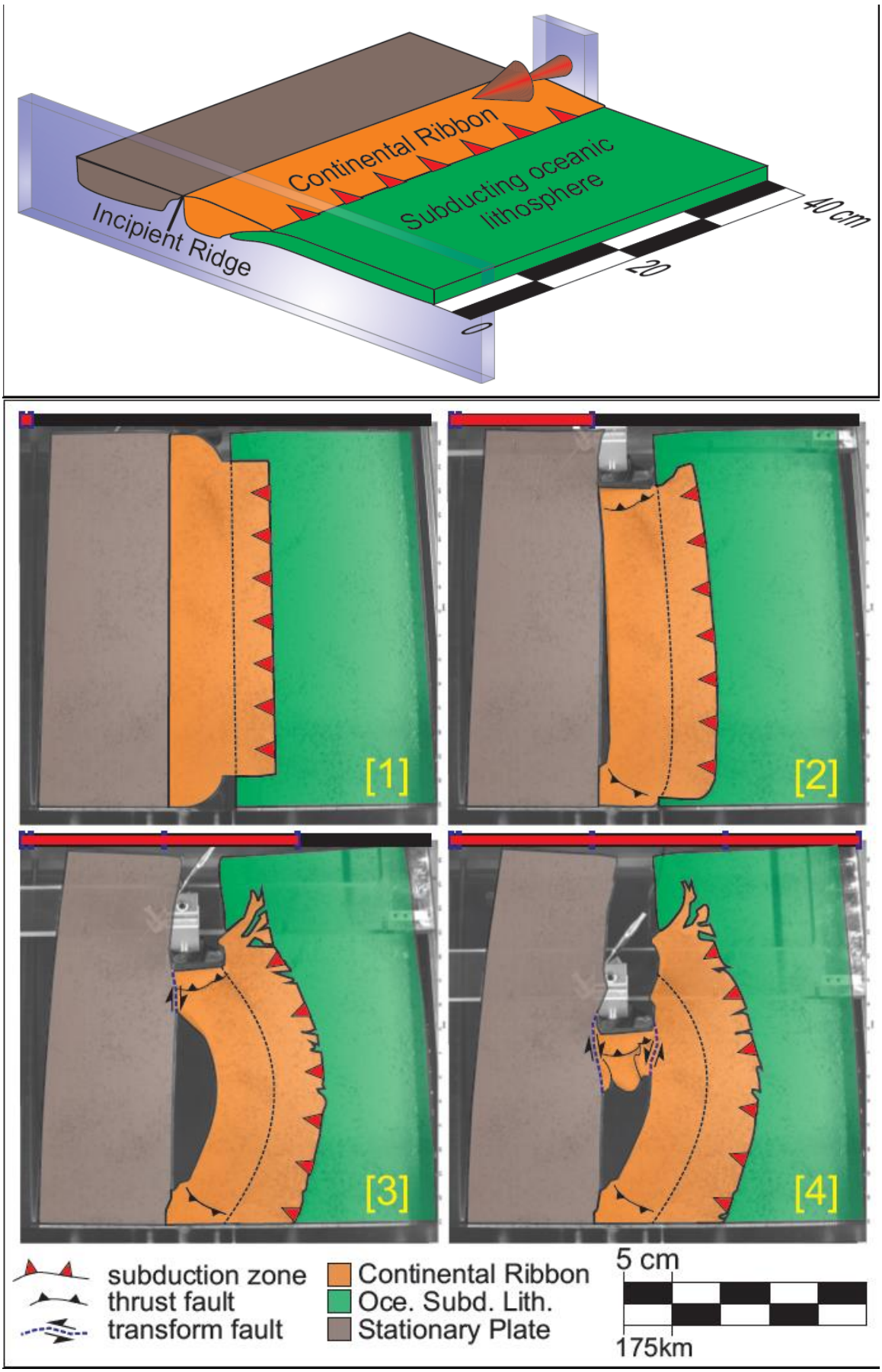
Continental Ribbon
Subducting oceanic lithosphere
Incipient Ridge
40 cm
20
0
[1]
[2]
[3]
[4]
subduction zone
thrust fault
transform fault
Continental Ribbon
Oce. Subd. Lith.
Stationary Plate
5 cm
175km

**Figure 9. (p.31 top) 3-D sketch of model C-5 at its initial state.**

**Figure 10. (p.31 bottom) Surface pictures of model C-5 . [1] At its initial state, a linear continental ribbon (orange) overthrusts an oceanic plate (green) on one side and shares on the other side an incipient ridge with a stationary continental plate (purple). [2] As the continental ribbon is compressed between the narrow piston and the back-wall, there is occurrence of thickening and minor surface thrusts at the collisional contacts. Concurrently, opening of an interlimb basin initiates at the incipient ridge. A strike-slip dextral transform fault is activated at the border between the ribbon and the stationary plate to allow shear motion all along the experiment. [3] Curvature extends toward the oceanic plate which underthursts under the buckling ribbon. On the other side, the incipient ridge has extended into a wide interlimb basin. [4] At last, the formation of a second strike-slip fault, sinistral this time, bisects the trailing limb and pushes it into the interlimb basin. The black dashed line outlines the lower contact between the ribbon and the oceanic plate. The red bar represents a time scale for which each interval equals approximately 10 million years.**

## 3.7 Triple junctions

Another tectonic scenario explored is where the ribbon's lateral border intersects another convergent plate boundary. Our study of "triple junctions" took the form of trench-trench-trench (TTT) junctions, where a convergent margin along one side of a continental ribbon intersects a subduction zone between two oceanic plates adjacent and subducting beneath the ribbon (3 models from **Fig. 11**). In such models, it is observed that structures responsible for lithospheric failure and deformation of the continental ribbon nucleate at the triple junction.

**Figure 11. (p.33) Surface pictures of 3 experiments at initial, mid and final stages (respectively from left to right). These models all involve a similar scenario to experiment C-8 (Magmatic arc scenario; Fig. 9 & Fig. 10), only this time with a pre-existing thrust segmenting the oceanic plates and forming a triple junction with the ribbon. The initial geometry of the model determines whether the favoured deformational feature of the continental ribbon will be subduction of the ribbon [C-13], an oblique transpressional system [C-11] or initiation of a coupled orocline [C-6]. The blue shading indicates the locality of preferential convergence at the model's surface. The black arrows symbolize motion vectors, depicting relative plate motion.**

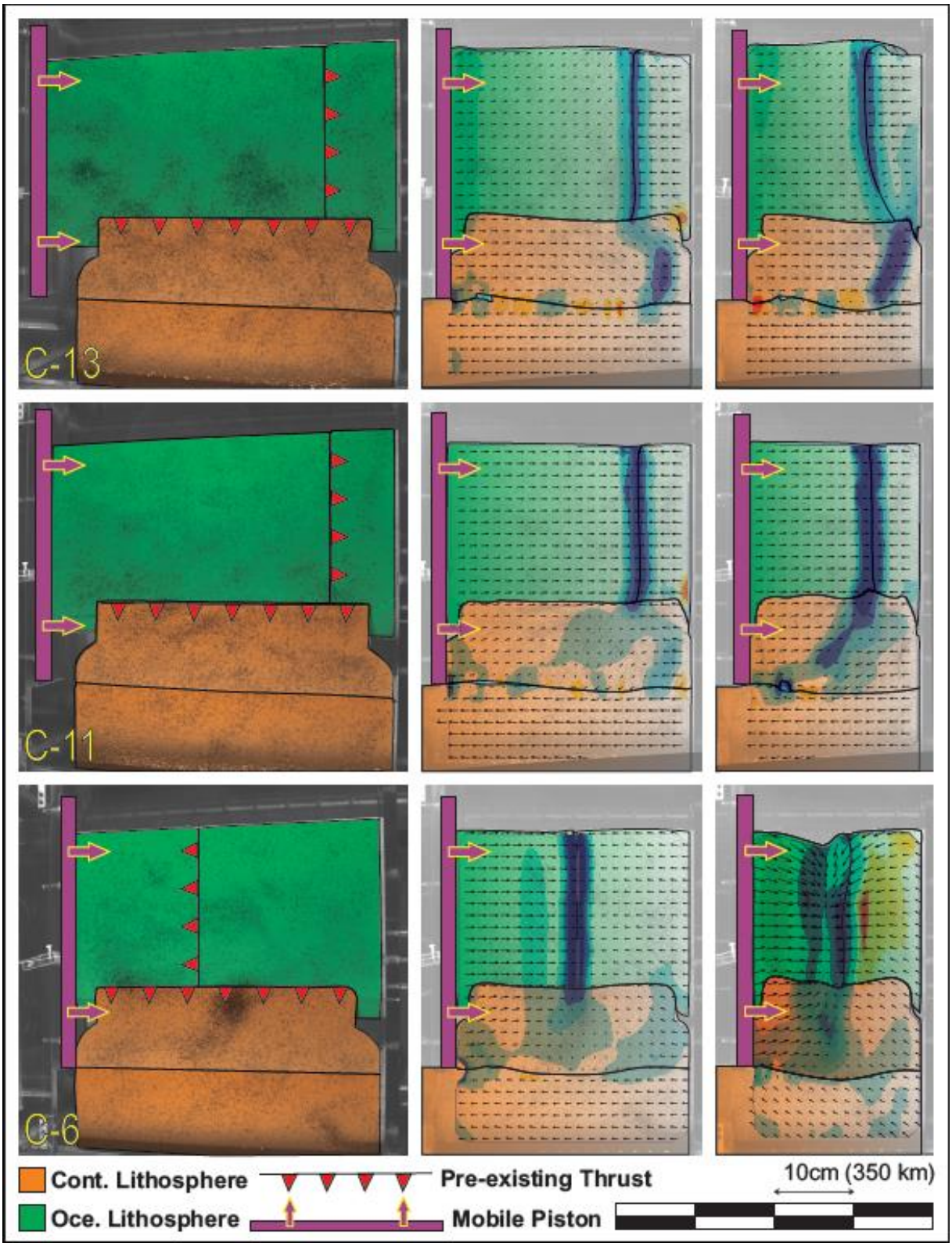
C-13
C-11
C-6
Cont. Lithosphere
Oce. Lithosphere
Pre-existing Thrust
Mobile Piston
10cm (350 km)

Upon activation of the piston, the pre-existing oceanic-oceanic subduction boundary causes downward bending and sinking of the underthrusted plate. At the triple junction compression caused by the three converging plates is transferred to the ribbon which itself is under ribbon-parallel compression (thickening and surface thrusts at collisional contacts as depicted in **3.1.1.**). As the piston advances, the triple junction behaves as a compressional instability triggering lithospheric-scale plastic deformation that shortens the ribbon. Shortening can take the shape of ribbon subduction [**C-13**], oblique transpression [**C-11**] or the initiation of a "coupled orocline" [**C-6**].

### 3.7.1. [C-13] Ribbon Subduction

This model is similar to the magmatic arc scenario (3.6.): the ribbon overthrusts an oceanic plate on one side and is bordered by an incipient ridge on the other. The prime distinction is an additional convergent boundary placed parallel to the piston and intersecting the ribbon orthogonally at the triple junction (TTT). The triple junction is located near the back-wall of the model. Localities of preferential convergence are calculated at the model surface via the P.I.V. technique (blue shading in **Fig. 11**). Convergence at the oceanic-oceanic convergent boundary is indicated by the narrow and deep blue line; **Fig. 11**, **C-13**). In the continental ribbon, initial convergence is dissipated within the collisional contact (**3.1.1.**). Later, convergence centralizes along a distinct thrust fault that propagates out of triple junction. Once the lithospheric failure along the thrust fault is entrenched, the continental ribbon is dragged down into the asthenosphere with the adjacent oceanic slab. Near the end of the experiment, compression of the buoyant underthrusted ribbon forces the triple junction to slowly migrate towards the back-wall.

### 3.7.2. [C-11] Oblique Transpressional System

Experiment **C-11** is similar to **C-13** with the exception that the ribbon is thinner, facilitating a distinct lithospheric failure. The oceanic-oceanic subduction zone and the convergent margin of the ribbon are the principal locations of convergence. Continued convergence results in the development of a steep structure that propagates diagonally across the ribbon. P.I.V. analysis shows motion along this structure, separating the ribbon into two halves. Near the end of the experiment, the lithospheric-scale vertical fault bisects the entire ribbon (**Fig. 11**) forming a dextral transpressional system that allows shear displacement between the trailing and the leading limbs of the ribbon. The trailing limb overrides the adjacent oceanic lithosphere while the leading limb thickens. Once again, failure of the ribbon initiates at the triple junction and once well-established, the resulting structure accommodates much of the shortening.

### 3.7.3. [C-6] Initiation of a Coupled Orocline.

In this experiment the triple junction is placed at the ribbon's mid-point and the polarity of oceanic subduction is reversed (the oceanic plate is attached to the back-wall and underthrusts the other plate). As in **C-11** and **C-13**, in order to initiate buckling toward the oceanic plates, tapered corners are carved at the collisional contacts of the ribbon. Upon piston activation, the ribbon bends toward the triple junction, but only briefly, before compression at the subduction zone deflects the middle of the ribbon back toward the weak and thin incipient ridge bounding the backside of the ribbon. P.I.V. analysis of relative surface motion (**Fig. 11**) shows three principal peaks of convergence (blue) within the ribbon: one at the triple junction and two others at both of the collisional contacts. This configuration is concomitant with four centres of vertical-axis rotation for which the directions alternate between clockwise and anticlockwise (respectively blue and red in **Fig. 12**). Such a rotational structure permits activation of three distinct oroclinal hinges (**Fig. 12**), that coincide with the three centers of convergence (**Fig. 11**). This flexing deformation is

observable from the bottom of the lithosphere where the lithospheric root of the orogen folds into an M-shape. Toward completion of the experiment, this rotational system gives way to intense thickening and the initiation of deep thrusts. At the end, this model records significant convergence at its oceanic-oceanic boundary, while most of the subducting slab sinks and pulls on the little oceanic lithosphere left at the surface.

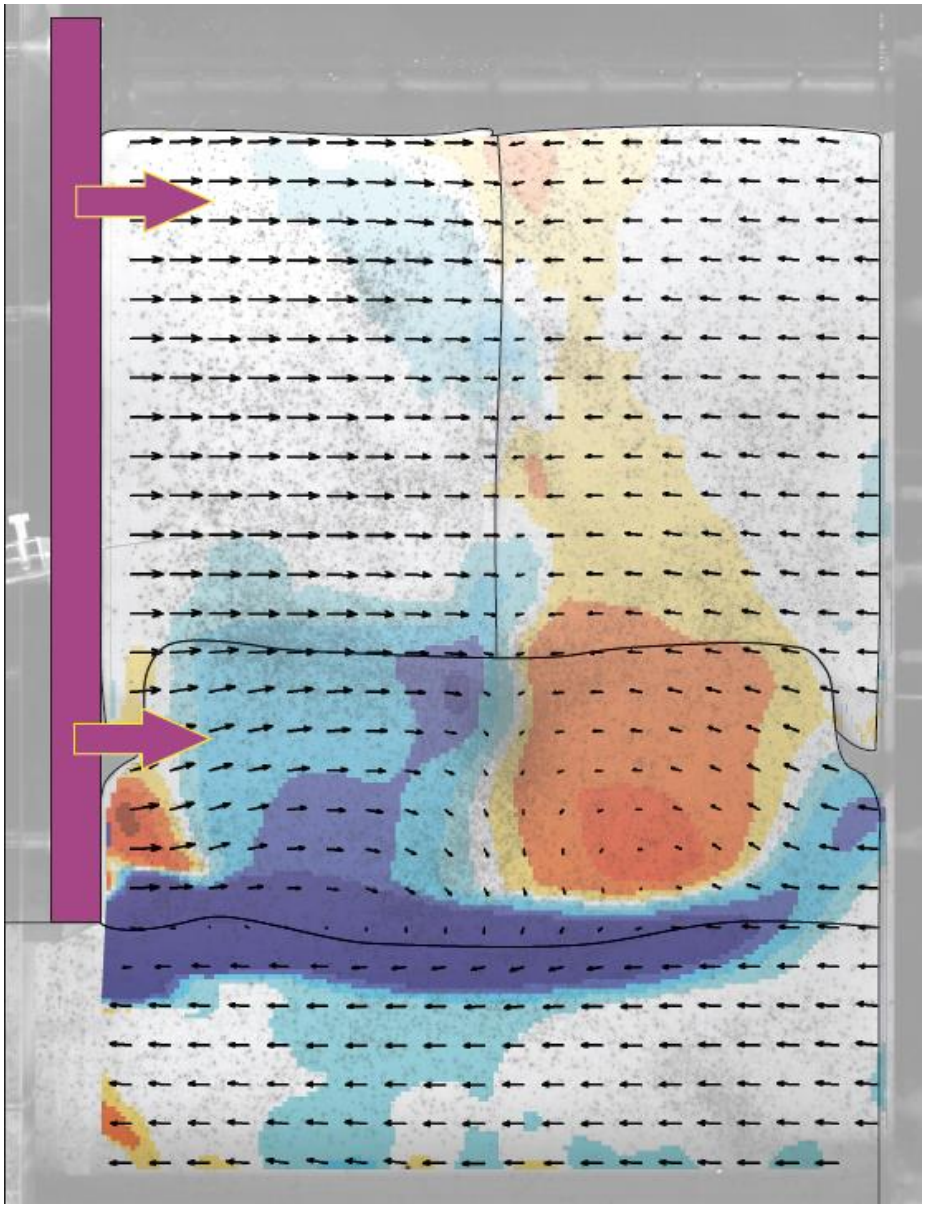

**Figure 12. Experiment C-6 at mid-stage. Blue (clockwise) and red (anticlockwise) shadings point to the rotational apexes. It shows four different rotational peaks with alternating directions. The thick blue line at the incipient ridge corresponds to the dextral shear motion perceived as clockwise vorticity. The black arrows symbolize motion vectors, depicting relative plate motion.**

Chapter 4

# 4. Discussion

This study presents models that help us resolve questions regarding oroclines, including their tectonic requirements and their scale. Some of the analogue continental ribbons, when subjected to ribbon-parallel compression, developed features that are rigorously similar to those found in natural oroclines, notably the Central Iberian, Panamian and Calabrian oroclines. The broad quantitative and qualitative dataset generated during modeling can be applied toward the elucidation of mechanisms responsible for vertical-axis flexing of a continental beam.

## 4.1. Requirements for oroclines

According to the empirical outcomes of this study, initiation and development of an orocline requires the following conditions.

1) Long axis parallel compression of a thick, strong and buoyant, ribbon-shaped continental lithospheric prism.

2) At least one of the ribbon continent's margins must be amenable to accommodating buckling and hinge migration. A convergent margin or subduction zone provides the ideal boundary condition: the buoyant orogen, as it buckles, can then easily overthrust the adjacent oceanic plate.

3) Extension has to prevail on along the margin opposite of the migrating orocline hinge. Incipient ridges are efficient boundaries for the initiation of an extensional interlimb basin. The genesis of such longitudinal zones of weakness requires margin-parallel zones of high heatflow and a tensile stress field (A. Nicolas et al, 1994), both of which can be found in

magmatic back-arc settings. Alternatively, any other elongated zone of weakness or thinned lithosphere has the potential to act as a locus for the opening of an interlimb basin during oroclinal buckling. On the other hand, two types of boundary that impede extension are deep vertical transform faults and convergent margins, both of which engage too much interface tension. Evidently, if a ribbon continent is already bordered by an extensional basin, further divergence can readily be accommodated.

4) The high aspect ratio of continental ribbons makes them vulnerable to lithospheric failure. For buckling to prevail, the ribbon has to be free of lithospheric-scale fractures that could be activated, yielding a different shortening mechanism. This precludes ribbons characterized by pre-existing thinned zones, and large-scale thrust or transform faults. In addition, overly narrow ribbon continents will break instead of buckling. Stress instabilities, like the proximity of a triple junction, can similarly operate as the trigger for lithospheric failure, severing the entire ribbon (**Fig. 11**). Similarly, the initiation of late stage transform faults during buckling will terminate buckling and can be attributed to the instability generated by an increasing angle between the shortening axis and the strike of the orocline's trailing limb. Comparable transform faults were produced in other lithospheric-scale analogue models (Pastor-Galán et al. 2012).

5) The forces required for the buckling of an orogen or ribbon continent are of the same scale as those driving subduction. A piston speed of roughly 8 cm/year (nature scale) succeeded in buckling many of our models, evincing the relative convergance rate of plates abbuting a subduction zone. Paleomagnetic data show that development of the Alaskan oroclines of the Cordillera and the Iberian oroclines of the Variscan orogen involved translation rates of about 10 cm/a for periods of 10 to 20 million years (Johnston 2013 and references therein). This suggests that the tectonic regime best-suited to produce oroclinal buckling is a convergent boundary.

## 4.2. Oroclinal scale

A significant, ongoing debate (Johnston 2004; Johnston et al. 2012) concerning oroclines is the question of their scale: do they involve the lithospheric mantle or are they thin-skinned structures restricted to the crust (Burchfield, 1980; Pérez-Estaún et al. 1988; Marshak, 1988 and reference therein). It has been argued that the crust is too weak to support large-scale and protracted deformation implied by continental-scale oroclines and that the implied buckling requires the involvement of the stronger and more ductile behaviour of the sub-crustal lithospheric mantle (Gutierrez-Alonzo et al. 2004). The lithospheric-scale of oroclines has, however, been disputed, in part because such structures would involve a large accumulation of lithosphere at the inner orocline hinge, leading to intense isostatic instability. Geological and geophysical data has yet to provide a definitive resolution to this debate. Hence, there is much to be gained by resolving the true scale of oroclinal deformation.

Our results established that thick-skinned lithospheric ribbons have the ability to buckle about vertical axes of rotation. In contrast, as shown in section 3.3., crustal material, when subjected to the compressional regime of a subduction zone, behaves in a strain-localized and extrusive manner. This type of deformation, consistent with weak materials (W.F. Brace, 1980; N.J. Kusznir & R.G. Park, 1987; D.L. Kohlstedt et al., 1995), does not allow for the transfer of stress along the length of a crustal beam, and hence negates oroclinal buckling as a means of deformation. Consequently, the only way to produce oroclines in our experiments was to involve the lithospheric mantle underpinning a ribbon continent (**D-2**). These results suggest that oroclines depend upon the deep mantle-lithosphere. Although oroclines require mantle involvement, there are other plausible tectonic scenarios that can result in curvature of crustal structures (Weil, A. B. 2004). However, such thin-skinned formations do not imply an orogen-parallel stress field and therefore cannot be considered as proper “secondary oroclines”.

## 4.3. Differential thickening and lithospheric delamination

Flexing a ribbon around a vertical axis implies subjecting it to a system of "tangential longitudinal strain" (S.W. Carey, 1955; Seeber, 1984; A.C. Ries & R.M. Shackleton, 1976; N.C. Bobillo-Ares 2000; G. Gutierréz Alonso et al. 2004) driving arc-parallel shortening on the concave side and tangential extension around the convex margin. Such strain distribution (**Fig. 13**) is concordant with an anticipated differential thickening (inner swelling and outer thinning). The outstanding lithospheric growth inherent to closure of the buckle in our models (up to 92% thickening) represents a major lithospheric mass imbalance. Such gravitational instability is likely to activate delamination of the unstable lithospheric root (Bird, 1979; Houseman et al., 1981; Houseman and Molnar, 1997; Gutierréz Alonso et al. 2004, Johnston et al. 2013). It stands to reason that if such a detachment of the lower mantle prevails, it will likely initiate via one of the deep thrust faults (possibly one of the blind thrusts) observed under the lithospheric root, at the locality of preferential thickening (seen in experiments **D-2**, **D-4**, **C-6**, **C-8**, **C-9**; **Fig. 7** & **Fig. 8**). Effectively, the isostatic instabilities were accommodated via plastic-strain material redistribution, along both surface (small-scale) and lithospheric-scale root thrusts. The inception of a crustal ''pinch down'' found within cross sections of the buckle's inner hinge (**D-2**; section **3.3.**) provides additional support for interpretations involving the development of lithospheric-scale delamination thrusts in orocline hinge zones (Schott & Schmeling 1998; Pysklywec 2006; Pysklywec et al. 2002; 2010, Morency and Doin, 2004).

Given a pre-existing plane of weakness within the lithosphere, delamination may be activated without the prerequisite of going through lithospheric fractures. An example of such a detachment is the omnipresent MOHO discontinuity. The MOHO can operate as a decoupling interface allowing the mantle to detach from the crust and to sink while the weak crust wedges itself into a converging boundary (Boutelier 2004; Duretz et Gerya 2013; **Fig. 5** & **Fig. 6**). Buoyancy is the most significant factor: the dense mantle bends downward while the buoyant crust resists drowning, preferring instead to wedge, thicken, exhume and

extrude. These mechanisms are potentially those which bring to the surface the enigmatic Low-T High-P crustal rocks (Boutelier 2008) and beg the question 'are ultra-high pressure metamorphic rocks exposed at the surface sometimes the result of lithospheric thickening in oroclinal hinge zones?'.

Effectively, once mantle delamination has occured, "slab pull" aborts, and the remaining crust undergoes instantaneous uplift and exhumation. An intense magmatic pulse, commonly with a fresh Sm/Rd signature (new asthenosphere filling the gap; Gutierrez-Alonso 2011) is observed. An example of such a delamination event associated with orocline formation may be provided in the Eastern Carpathians (Knapp et al., 2005; Houseman and Gemmer, 2007; Ismail-Zadeh et al. 2008; Lorinczi and Houseman, 2009; Fillerup et al., 2010) where deep seismicity beneath the hinge of the Carpathian orocline may indicate mantle delamination.

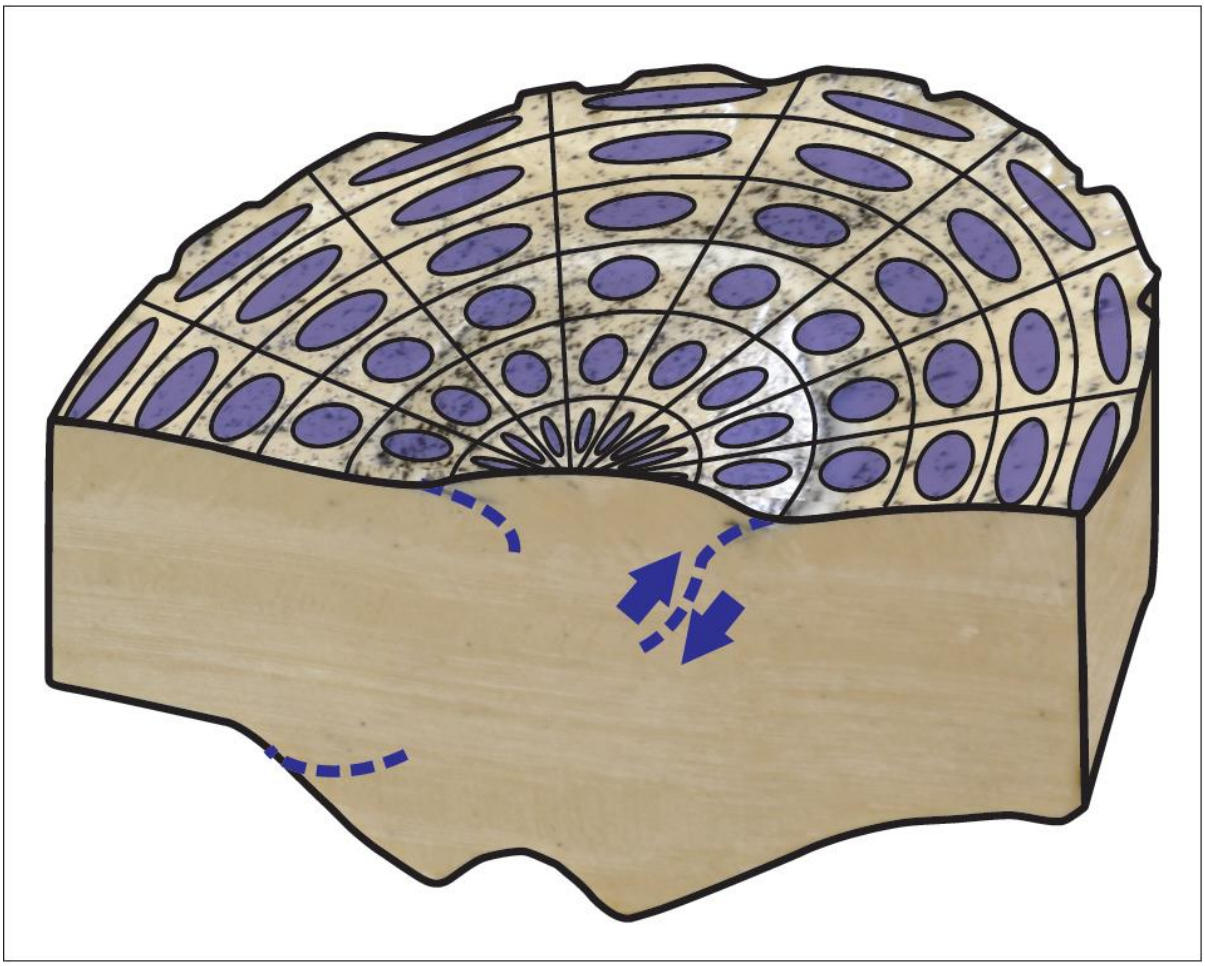

**Figure 13. 3-D Sketch portraying a dissected block (from experiment D-4) and the strain response to vertical axis buckling. Built from two pictures from Fig.8: the model's surface and the cross section [B], both distorted for the sake of 3-D perspective. The strain ellipses show arc-tangent stretching (outer arc) and arc-tangent compression (inner arc) concomitant with thinning and thickening, respectively. Palinspastic reconstruction of this bend would reveal a linear ribbon with strain ellipses all equally symmetrically circular.**

## 4.4. Natural Analogues

### 4.4.1. Variscan Coupled Oroclines

The coupled oroclines of the Variscan orogen (**Fig. 14**) of Iberia include the Central Iberian orocline and the more northerly Cantabrian orocline. These coupled oroclines affect an originally linear, N-S trending orogen (Weil. et al. 2013). Numerous features characterizing these coupled oroclines can be found in our models.

The axial surface of the Central Iberian orocline aligns with the limit between a southern domain of 'Upright Folds' and a northern domain of 'Recumbent Folds' (Diez Balda et al., 1990). It also marks a dichotomy between two regions of different metamorphic grades and differing granitoid magmatism: lower grades and smaller volumes of granitod intrusions are found to the south (Lotze, 1945) of the axial surface of the Central Iberian Orocline. We argue that these characteristics are attributable to a major lithospheric thrust that allowed the trailing limb of the Central Iberian orocline to overthrust the orocline's leading limb, in a fashion similar to the overthrusting of the orocline forelimb observed in our experiments (**Fig. 7** & **Fig. 8**). Our results imply that the configuration and geometry of the Central Iberian orocline developed during final stages of closure of the orocline and indicate that its north- and south- limbs constitute the leading- and trailing-limbs, respectively, of an orocline that formed by overall northward translation during buckling of an originally linear orogen. The higher rates of erosion (Neoproterozoic to lower Cambrian; Shaw et al. 2012) are recorded in the trailing southern limb of the Central Iberian Orocline, supporting the hypothesis that it overthrusts the northern limb.

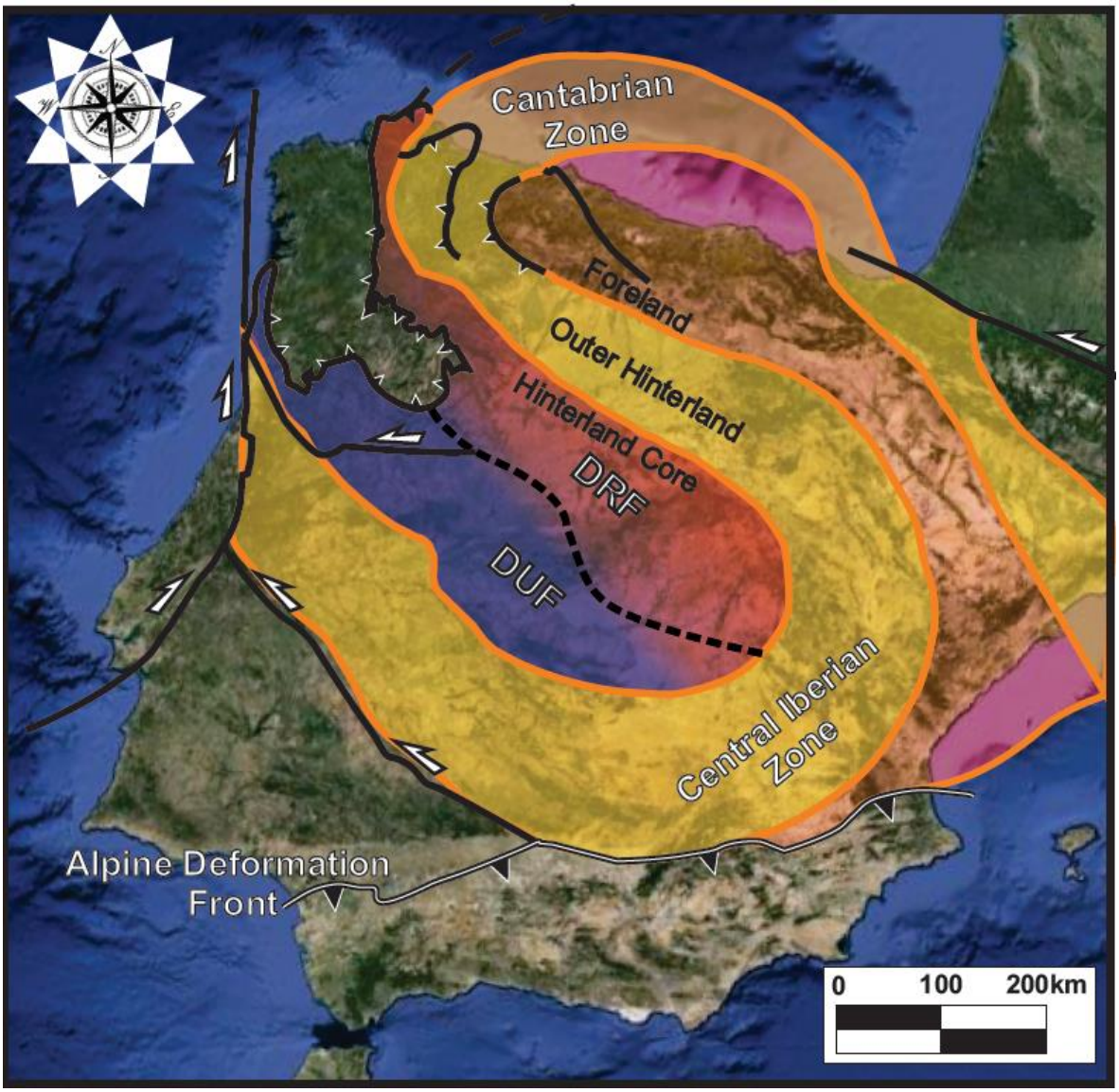


**Figure 14. Central Iberian and Cantabrian oroclinal pair of the Variscan where the outer hinterland of the orogen buckles twice on itself (orange band). The heavy dashed line that aligns with the axial plane of the Central Iberian bend is the demarcation between the Domain of Upright Folds (Blue, South West) and the Domain of Recumbent Folds (Red, North-East) that characterise the inner hinge of the hinterland core. (Continental outline: *Google Earth*; Drawn after Shaw et al. 2012)**

Two principal magmatic pulses characterise the Variscan belt during the time of oroclinal buckling. 1) Granitoids from 310 to 300 Ma (Fernández-Suárez et al., 2000; Gutierrez-Alonso, 2004) intrude the outer arc of the Cantabrian orocline where stretching (longitudinal strain) of the lithosphere (**Fig. 7** [2] & **Fig. 13**) is inferred to have occurred during oroclinal buckling. "Exentensional cracks", such as those formed within model **D-4** (**Fig. 7** & **Fig. 8**) could facilitate decompressive melting and the uprise of the resulting melts. 2) Between 295 and 285 MA a second voluminous magmatic episode characterizes the entire belt (Fernàndez-Suàrez et al., 2000; Valverde-Vaquero et al., 1999) and was accompanied by crustal melting, low-pressure high-temperature metamorphism and coeval mineralization (Gutierrez-Alonso et al. 2004). We consider late magmatic event as the direct aftermath of delamination of the lithospheric root that underpinned the orocline and of the subsequent asthenospheric renewal, which gives a juvenile Sm/Nd mantle signature to magmatism (Gutiérrez-Alonso et al., 2011; Ducea, 2011).

Coupled oroclines, those featuring more than one buckle, are a sign of greater shortening and of shorter buckling wavelengths (higher length/width ratio). A specific tectonic setting is required to stimulate the 3 centers of rotation and was only produced in our models through the use of oppositely apposed tapered corners on the ribbon continents (**Fig. 4**; **D-3**), or, where 4 centers of rotation form a "triple" or "M-shaped" buckle, the involvement of a trench-trench-trench triple junction C-6 (**Fig. 12**).

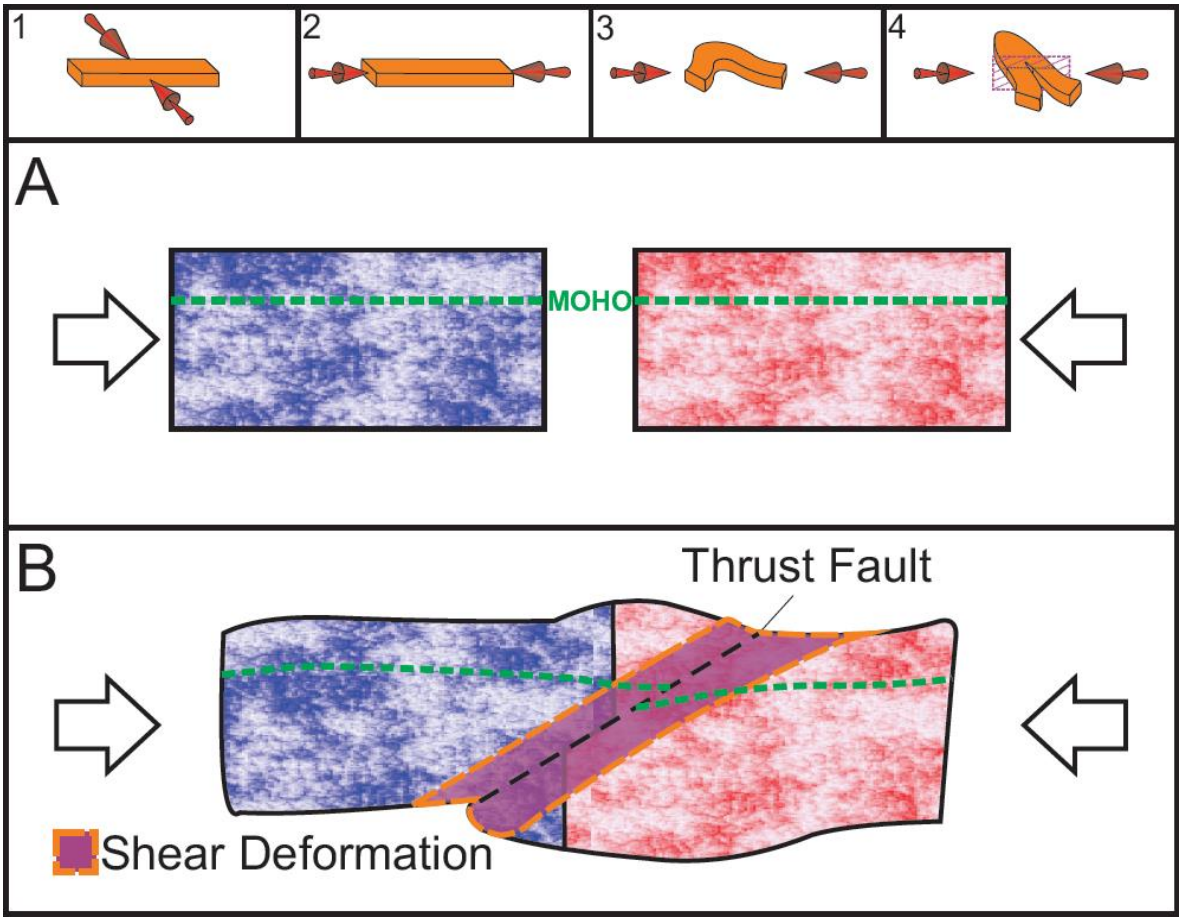


**Figure 15. Progression of a linear orogen upon complete closure of the oroclinal limbs [1 to 4]. The purple rectangle in [4] depicts the locality of the cross section presented in [A] where the trailing (blue) and leading (red) limbs are just about to collide. Cross section [B] is drawn after the contour of the cross section from D-4 (Fig. 7 [C]). Shear deformation (purple) is anticipated at the vicinity of the lithospheric-scale fracture and can explain the presence of recumbent folds at the surface of the leading limb, or the northern limb in the case of Central Iberia.**

### 4.4.2. Panama Deformed Belt

The collision of the Panamian Ismuth with South America in the mid-late Miocene (about 10 Ma) is renowned for providing a bridge that allowed for faunal interchange between the Americas (Marshall et al., 1979; Marshall, 1985; Webb, 1985), and for buckling of the Panamanian Ismuth (Eli Silver, 1990; Coates, 2004). Effectively, compression of the Ismuth between the North and South American continents caused it to buckle and overthrust the Caribbean plate to the northeast, in a manner similar to the continental ribbon from experiment C-5 which overthrust an adjacent oceanic slab. Moreover, the Panamanian Ismuth is bisected by a sinistral strike-slip transform fault, which is accommodating further shortening of the arc (Silver, 1990; Coates 2004; Farris, 2011; Montes et al. 2012). A similar feature developed in experiment C-5 (**Fig. 10**), where the increasing angle between the piston's axis of shortening and the strike of the adjacent orocline limb caused an instability that induced development of an oblique sinistral fault that cut through the entire continental ribbon and effectively terminated oroclinal buckling. Offset along the Panamanian transform fault explains the extended gap between the Paleogene volcanics either side of the transform. (**Fig. 16**)

### 4.4.3. Calabrian Orocline

Buckling of the Apennine – Maghrebide (Sicilian) takes place as the mountain chain is slowly compressed by Africa's 1cm/a (Johnston & Mazzoli) northward motion relative to cratonic Europe, closing the Mediterranean Sea en route (**Fig. 17**). Through the past 10 Ma, the Apennine and Maghrebide segments have rotated in opposite directions about a Calabrian hinge that has migrated to the southeast over the Ionian sea. As the buckle has developed, an extensional basin has opened behind it to the northwest giving rise to the Tyrhennian Sea (T.S.). This situation is analogous to experiment C-5, which involved a tectonic setting similar to that inferred for the Calabrian orocline, and which produced a similar orocline via modeling of a thick skinned continental ribbon compressed and buckled

upon overall orogen parallel compression (northward migration for the Calabrian; Johnston & Mazzoli, 2009), providing an other alternative than the thin skinned (Elderedge et al. 1985) and roll back models (Kastens et al. 1988; Cifelli et al. 2008).


**Figure 16. Interpretative map of Central America featuring the extent of the continental ribbon (orange shading) supporting the Panamian Ismuth (continental outline: *Google Earth*), the North- and the South-American continents (Purple). Dashed toothed lines depict the converging boundaries. Miniature map at the bottom left is a scheme of the relative plate motions around the investigated area. SPDB- South Panama deformed belt. NPDB- North Panama deformed belt. (Drawn after Coates 2004)**

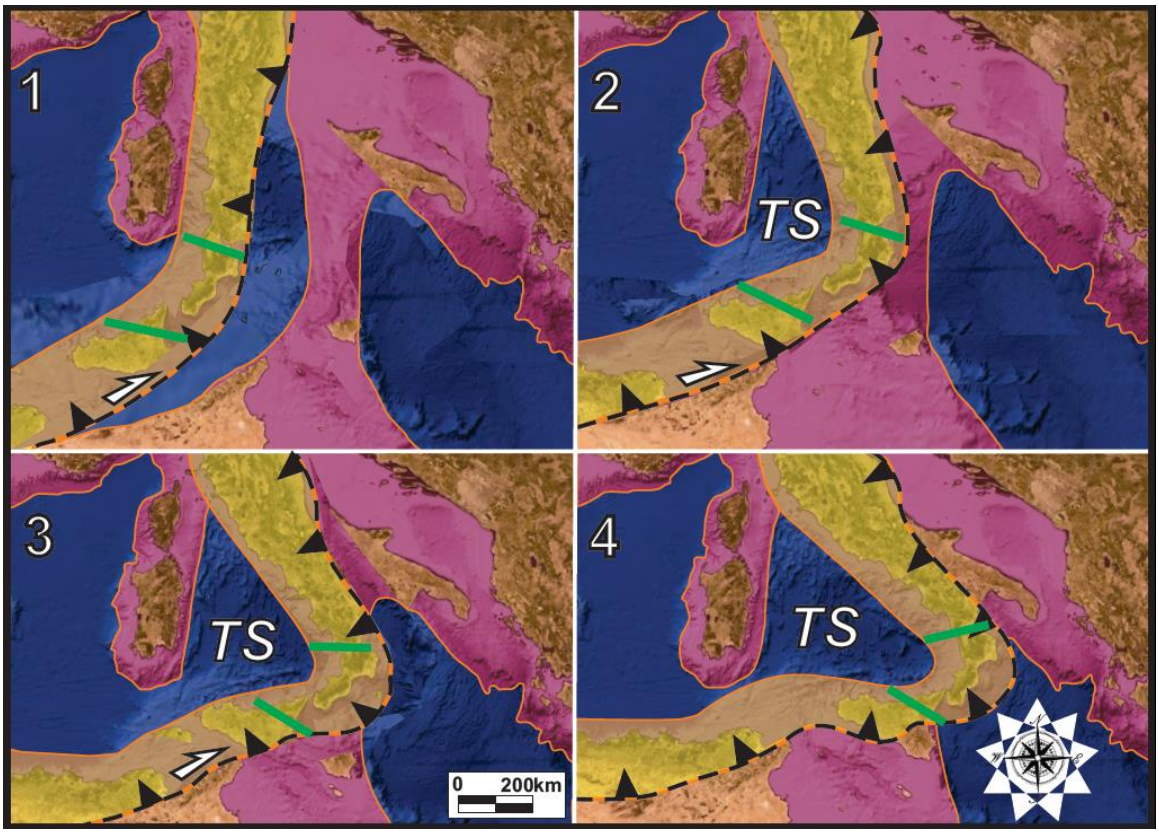


**Figure 17. Progression of the Apennine-Silician mountain chain through the past 10 Ma. Present day continental outline (*Google Earth*) are presented along with the full extent of continental crust (orange) and the oceanic to transitional crust (purple). The linear palinspastically restored continental ribbon slowly develops buckling south-eastward, as it overthrusts (black teeth) the oceanic lithosphere (Ionian sea) and opens an extensive basin to the north-west, the Tyrrhenian Sea (TS). The later basin starts to close itself as the two limbs (Apennine and Maghrebide belts) are rotating toward each other. Green lines are the Sangineto (sinistral) and the Taormina (dextral) transform faults (drawn after Johnston & Mazzoli 2009)**

## 4.5 Models' Limitations

Alike any model, those presented in this study know limitations. For instance the size of the modeling device constrains the modeled plates not to exceed 40 cm of length. A longer tank would allow us to experiment on the bending wavelength of buckling beams and would accommodate more shortening, multiplying the number of possible modeling

scenarios. One approximation in our models is the use of water to model the asthenosphere, depreciating its natural viscocity (see 2.2.1.). Such lower viscosity should result in a slight increase of the slab pull (lower viscous resistance) and lower the coupling at the astheno-lithosphere interface. New materials with a better suited viscosity, like cellulose polymer solutions, are presently being experimented in order to replace the water in future studies. The exact viscosity of the asthenosphere is still under debate, but is usually estimated between $10^{19}$ and $10^{21}$ Pa*s (Mitrovica and Forte, 2004; James et al., 2009). In models with an asthenosphere less viscous than these estimated values, it has been demonstrated (numerical modeling; Bonnardot et al. 2008) that there is not much impact registered in the geometry and dynamics of a subducting slab. Moreover, in our models, during opening of extensional basins, the $H_2O$ did not fulfill the criteria of an asthenosphere that forms new oceanic lithopshere as it surfaces at the ridge. At last, further investigation is crucial to conclude on the matter, for instance more models should be developed to test which tectonic scenarios offer the less resistance to bending of a continental beam (excluding the approximation of free ribbons). Extensional forces like slab pull could potentially not only accommodate but even activate the buckling mechanisms. Trying to resolve these empirical obstacles and to expand on different plausible tectonic scenarios will help better and further constrain the formation of the world-renowned oroclines.

*Chapter 5*

# 5. Conclusions

The first attempts to use paraffin-wax analogues to thermo-physically model "oroclines" are presented in this study which addresses the question of the oroclinal requirements, constraints and scale. We employ a three-dimensional thermo-mechanical analogue modeling device in order to investigate the behaviours of these originally linear continental "orogens" when positioned parallel to the shortening axis of a compressive regime. Our models show textbook examples of vertical axis buckling, along with the systems inherent to "tangential longitudinal strain" (differential thickening, delamination, thrusts, "extensional cracks", etc.). This form of plastic strain deforms the entire lithosphere, as predicted by the "thick-skinned" orocline hypothesis (lithospheric scale); besides, it was proven unfeasible to produce "thin-skinned" oroclines (crustal scale), as the weak crust yields an extensively extrusive and strain-localized behaviour.

Our analogue models show striking similarities with some exhaustively studied natural oroclinal structures. For instance, experiment C-5, strongly comparable to the Central Iberian Orocline (CIO), guided us to an explanation to why its north limb exposes recumbent folds while its south limb bears upright folds. In the model, a thrust fault is found to activate between the 2 limbs, allowing the trailing arm to overthrust the leading arm, accommodating further shortening after closure of the bend. We argue that the shear deformation inherent to such large thrust is what deformed the pre-existing upright Variscan folds into recumbent folds. Such results indicate that the north- and south- limbs of the CIO constitute the leading- and trailing- limbs, respectively, of an orocline that formed by overall northward translation. Moreover, the two wide magmatic episodes of the Variscan coincide with two mechanisms pinpointed in our buckling models: 1) outer arc thinning (steeper Geotherm.) and 2) delamination of the lithospheric hinge.

The Panamian and the Calabrian Ismuths share a similar tectonic scenario: both are wedged between 2 converging massive continents. Alike our magmatic arc analogues, the 2 originally linear continental ribbons slowly develop a vertical-axis buckle, overthrusting the oceanic plate on one side and opening an extensive “interlimb basin” on the other. A late-stage large-scale strike-slip sinistral fault also severes through the entire modeled beam, reminiscent of the Panama Canal and Sangineto sinistral transform faults.

This study shows that our modeled “oroclines” withstand the direct aftermaths of tangential longitudinal strain. The same outcomes should therefore also be expected within natural analogues. This implies high levels of compression at the inner hinge expressed through thickening and thrust systems that can potentially evolve into lithospheric delamination. Around the outer arc of the buckling beam, we can predict extensional features such as thinning of the lithosphere or even extensional fracturing. The highly compressive regimes in cause, principally in zones of weakness or instability, can also trigger other lithospheric scale failures such as transpressional systems or lithospheric underthrusts. Further research would be beneficial to advance on many questions like thoses of “coupled oroclines” and “terrane wrecks”.

# References


Adam, J., Urai, J.L., Wieneke, B., Oncken, O., Pfeiffer, K., Kukowski, N., Lohrmann, J., Hoth, S., van der Zee, W., Schmatz, J., 2005. Shear localisation and strain distribution during tectonic faulting — new insights from granular-flow experiments and highresolution optical image correlation techniques. J. Struct. Geol. 27 (2), 283–301.

Bird, P., 1978, Initiation of intracontinental subduction in the Himalaya: Journal of Geophysical Research, v. 83, p. 4975–4987.

Bobillo-Ares, N. C., F. Bastida, and J. Aller. "On tangential longitudinal strain folding." *Tectonophysics* 319, no. 1 (2000): 53-68.

Boutelier, David, Alexandre Chemenda, and Cedric Jorand. "Thermo-mechanical laboratory modelling of continental subduction: first experiments." *Journal of the Virtual Explorer* 6 (2002): 61-65.

Boutelier, D., Chemenda, A., and Burg, J.-P., 2003, Subduction versus accretion of intra-oceanic volcanic arcs: insight from thermo-mechanical analogue experiments: Earth and Planetary Science Letters, v. 212, no. 1-2, p. 31–45, doi: 10.1016/S0012-821X(03)00239-5.

Boutelier, D., A. Chemenda, and C. Jorand (2004), Continental subduction and exhumation of high-pressure rocks: Insights from thermo-mechanical laboratory modelling, Earth Planet. Sci. Lett., 222, 209–216, doi:10.1016/j.epsl.2004.02.013.

Boutelier, D., and A. Chemenda (2008), Exhumation of UHP/LT rocks due to the local reduction of the interplate pressure: Thermo-mechanical physical modelling, Earth Planet. Sci. Lett., 271, 226–232, doi:10.1016/j. epsl.2008.04.011.

Boutelier, D., and O. Oncken, 2011, 3-D thermo-mechanical laboratory modeling of plate-tectonics: Modeling scheme, technique and first experiments, Solid Earth, 2, 35–51, doi:10.5194/se-2-35-2011.

Boutelier, D., and A. Chemenda (2011), Physical modeling of arc-continent collision: A review of 2-D, 3-D, purely mechanical and thermo- mechanical experimental models, in Arc-Continent Collision, edited by D. Brown and P. Ryan, pp. 445–473, Springer, Berlin, doi:10.1007/978- 3-540-88558-0_16.

Brace, W.F., Kohlstedt, D.L., 1980. Limits on lithospheric stresses imposed by laboratory experiments. J. Geophys. Res. 85, 6248– 6252.

Buckingham, Edgar. "On physically similar systems; illustrations of the use of dimensional equations." *Physical Review* 4, no. 4 (1914): 345-376.

Burchfield, Susan R., Stephen C. Woods, and Matthew S. Elich. "Pituitary adrenocortical response to chronic intermittent stress." *Physiology & behavior* 24, no. 2 (1980): 297-302.

Byerlee, J., 1978. Friction of rocks. Pure Appl. Geophys. 116 (4–5), 615–626.

Carey, S.W., 1955, The orocline concept in geotectonics: Proceedings of the Royal Society of Tasmania, v. 89, p. 255–288.

Chemenda, Alexander I., Jean-Pierre Burg, and Maurice Mattauer. "Evolutionary model of the Himalaya–Tibet system: geopoem: based on new modelling, geological and geophysical data." *Earth and Planetary Science Letters* 174, no. 3 (2000): 397-409.

Cifelli, F., Mattei, M., and Della Seta, M., 2008, Calabrian arc oroclinal bending: The role of subduction: Tectonics, v. 27, TC5001, doi:10.1029/2008TC002272.

Coates, A.G., Collins, L.S., Aubry, M.P., and Berggren, W.A., 2004, The geology of the Darien, Panama, and the late Miocene–Pliocene collision of the Panama arc with northwestern South America: Geological Society of America Bulletin, v. 116, p. 1327–1344, doi: 10.1130/B25275.1.

Conrad, Clinton P., and Mark D. Behn. "Constraints on lithosphere net rotation and asthenospheric viscosity from global mantle flow models and seismic anisotropy." *Geochemistry Geophysics Geosystems* 11, no. 5 (2010): Q05W05.

Davy, Ph, and P. R. Cobbold. "Experiments on shortening of a 4-layer model of the continental lithosphere." *Tectonophysics* 188, no. 1 (1991): 1-25.

Díez Balda, M.A., Vegas, R., and González Lodeiro, F., 1990. Structure, *in* Dallmeyer, R.D., and Martínez García , E., eds., Pre-Mesozoic Geology of Iberia: Berlin, Springer-Verlag, p. 172–188.

Doglioni, Carlo, Alik Ismail-Zadeh, Giuliano Panza, and Federica Riguzzi. "Lithosphere–asthenosphere viscosity contrast and decoupling." *Physics of the Earth and Planetary Interiors* 189, no. 1 (2011): 1-8.

Ducea, M.N., 2011, Fingerprinting orogenic delamination: Geology, v. 39, p. 191–192, doi: 0.1130/focus022011.1.

Duretz, T., and T. V. Gerya. "Slab detachment during continental collision: Influence of crustal rheology and interaction with lithospheric delamination." *Tectonophysics* (2013).

Eldredge, S., Bachtadse, V. and Van der Voo, R., 1985. Paleomagnetism and the orocline hypothesis. In: N.L. Carter and S. Uyeda (Editors), Collision Tectonics: Deformation of Continental Lithosphere. *Tectonophysics, 119: 153-179.*

Evans, Brian, and David L. Kohlstedt. "Rheology of rocks." *AGU Reference Shelf* 3 (1995): 148-165.

Farris, David W., Carlos Jaramillo, German Bayona, Sergio A. Restrepo-Moreno, Camilo Montes, Agustin Cardona, Andres Mora, Robert J. Speakman, Michael D. Glascock, and Victor Valencia. "Fracturing of the Panamanian Isthmus during initial collision with South America." *Geology* 39, no. 11 (2011): 1007-1010.

Fernández-Suárez, J., Dunning, G.R., Jenner, G.A., and Gutiérrez-Alonso, G., 2000, Variscan collisional magmatism and deformation in NW Iberia: Constraints from U-Pb geochronology of granitoids: Journal of the Geological Society, v. 157, p. 565–576, doi: 10.1144/jgs.157.3.565.

Fillerup, M.A., Knapp, J.H., Knapp, C.C., and Raileanu, V., 2010, Mantle earthquakes in the absence of subduction? Continental delamination in the Romanian Carpathians: Lithosphere, v. 2, p. 333–340, doi: 10.1130/L102.1.

Ghosh, S. K., and Hans Ramberg. "Buckling experiments on intersecting fold patterns." *Tectonophysics* 5, no. 2 (1968): 89-105.

Goetze, Christopher, and Brian Evans. "Stress and temperature in the bending lithosphere as constrained by experimental rock mechanics." *Geophysical Journal International* 59, no. 3 (1979): 463-478.

Gutiérrez-Alonso, G., Fernández-Suárez, J., and Weil, A.B., 2004, Orocline triggered lithospheric delamination, *in* Sussman, A.J., and Weil, A.B., eds., Orogenic Curvature: Integrating Paleomagnetic and Structural Analyses: Geological Society of America Special Paper 383, p. 121–131.

Gutiérrez-Alonso, G., Fernández-Suárez, J., Jeffries, T.E., Johnston, S.T., Pastor-Galán, D., Murphy, J.B., González, M.P.F., and Gonzalo, J.C., 2011, Diachronous postorogenic magmatism within a developing orocline in Iberia, European Variscides: Tectonics, v. 30, TC5008, doi:10.1029/2010TC002845.

Gutiérrez-Alonso, G., S. T. Johnston, A. B. Weil, D. Pastor-Galán, and J. Fernández-Suárez. "Buckling an orogen: the Cantabrian Orocline." *GSA Today* 22, no. 7 (2012): 4-9.

Hampel, A., Adam, J., Kukowski, N., 2004. Response of the tectonically erosive south Peruvian Forearc to subduction of the Nazca Ridge: analysis of three-dimensional analogue experiments. Tectonics 23 (5), 16.

Hartz, Ebbe H., and Yuri Y. Podladchikov. "Toasting the jelly sandwich: The effect of shear heating on lithospheric geotherms and strength." *Geology* 36, no. 4 (2008): 331-334.

Houseman, G.A., McKenzie, D.P., and Molnar, P., 1981, Convection instability of a thickened boundary-layer and its relevance for the thermal evolution of continental convergent belts: Journal of Geophysical Research, v.86, p. 6115- 6132.

Houseman, G.A., and Molnar, P., 1997, Gravitational (Rayleigh-Taylor) instability of a layer with non-linear viscocity and convective thinning of continental lithosphere: Geophysical Journal International, v. 128, p. 125-150.

Houseman, Gregory A., and Lykke Gemmer. "Intra-orogenic extension driven by gravitational instability: Carpathian-Pannonian orogeny." *Geology* 35, no. 12 (2007): 1135-1138.

Ismail-Zadeh, Alik, Gerald Schubert, Igor Tsepelev, and Alexander Korotkii. "Thermal evolution and geometry of the descending lithosphere beneath the SE-Carpathians: An insight from the past." *Earth and Planetary Science Letters* 273, no. 1 (2008): 68-79.

Jeffery, George B. "The motion of ellipsoidal particles immersed in a viscous fluid." *Proceedings of the Royal Society of London. Series A, Containing Papers of a Mathematical and Physical Character* 102, no. 715 (1922): 161-179.

Johnston, S.T., 2004, The d'Entrecasteaux orocline and rotation of the Vanuatu–New Hebrides arc: An oroclinal orgy and analogue for Archean craton formation, *in* Sussman, A., and Weil, A.B., eds., Orogenic Curvature: Integrating Paleomagnetic and Structural Analyses: Geological Society of America Special Paper 383, p. 225–236.

Johnston, S.T., and Mazzoli, S., 2009, The Calabrian orocline: Buckling of a previously more linear orogen, *in* Murphy, J.B., Keppie, J.D., and Hynes, A.J., eds., Ancient Orogens and Modern Analogues: Geological Society of London Special Publication 327, p. 113–125.

Johnston, Stephen T., A. B. Weil, and G. Gutiérrez-Alonso. "Oroclines: Thick and thin." *Geological Society of America Bulletin* 125, no. 5-6 (2013): 643-663.

Johnston, Stephen T., A. B. Weil, and G. Gutiérrez-Alonso. "Oroclines: Thick and thin." *Geological Society of America Bulletin* 125, no. 5-6 (2013): 643-663.

Kastens, Kim, Jean Mascle, Christian Auroux, Enrico Bonatti, Christina Broglia, James Channell, Pietro Curzi et al. "ODP Leg 107 in the Tyrrhenian Sea: Insights into passive margin and back-arc basin evolution." *Geological Society of America Bulletin* 100, no. 7 (1988): 1140-1156.

Kohlstedt, D.L., Evans, B., Mackwell, S.J., 1995. Strength of the lithosphere: constraints imposed by laboratory experiments. J. Geophys. Res. 100, 17587– 17602.

Knapp, J.H., Knapp, C.C., Raileanu, V., Matence, L., Mocanu, V., Dinu, C., 2005. Crustal constraints on the origin of mantle seismicity in the Vrancea Zone, Romania: the case for active continental lithospheric delamination. Tectonophysics 410, 311– 323.

Kusznir, N. J., and R. G. Park. "The extensional strength of the continental lithosphere: its dependence on geothermal gradient, and crustal composition and thickness." *Geological Society, London, Special Publications* 28, no. 1 (1987): 35-52.

Lorinczi, P., and G. A. Houseman. "Lithospheric gravitational instability beneath the southeast Carpathians." *Tectonophysics* 474.1 (2009): 322-336.

Lambeck, K., and P. Johnston. "Land subsidence and sea-level change: contributions from the melting of the last great ice sheets and the isostatic adjustment of the Earth." In *Land Subsidence. Proc. Fifth Int. Symp. Land Subsidence, The Hague*, pp. 16-20. 1995.

Lotze, F., 1945. Zur Gliederung der Varisziden der Iberischen Meseta. Geotekton. Forsch. 6, 78–92.

Marshak, S., 1988, Kinematics of orocline and arc formation in thin-skinned orogens: Tectonics, v. 7, p. 73–86.

Marshak, S., 2004. Arcs, oroclines, salients, and syntaxes — the origin of map-view curvature in fold-thrust belts. In: McClay, K.R. (Ed.), Thrust Tectonics and Petroleum Systems: American Association of Petroleum Geologists Memoir, 82, pp. 131–156.

Marshall, L.G., Buttler, R.F., Drake, R.E., Curtis, G.H., and Telford, R.H., 1979, Calibration of the Great American Interchange: Science, v. 204, p. 272–279.

Marshall, Larry G. "Geochronology and land-mammal biochronology of the transamerican faunal interchange." In *The great American biotic interchange*, pp. 49-85. Springer US, 1985.

Montes, Camilo, Agustin Cardona, Rory McFadden, S. E. Morón, C. A. Silva, S. Restrepo-Moreno, D. A. Ramírez et al. "Evidence for middle Eocene and younger land emergence in central Panama: Implications for Isthmus closure." *Geological Society of America Bulletin* 124, no. 5-6 (2012): 780-799.

Montési, Laurent GJ, and Maria T. Zuber. "A unified description of localization for application to large-scale tectonics." *Journal of Geophysical research* 107, no. B3 (2002): 2045.

Morency, C., and M-P. Doin. "Numerical simulations of the mantle lithosphere delamination." *Journal of Geophysical Research: Solid Earth (1978–2012)* 109, no. B3 (2004).

Nicolas, A., U. Achauer, and M. Daignieres. "Rift initiation by lithospheric rupture." *Earth and planetary science letters* 123, no. 1 (1994): 281-298.

Pastor-Galán, Daniel, Gabriel Gutiérrez-Alonso, Kieran F. Mulchrone, and Pedro Huerta. "Conical folding in the core of an orocline. A geometric analysis from the Cantabrian Arc (Variscan Belt of NW Iberia)." *Journal of Structural Geology* 39 (2012): 210-223.

Pérez-Estaún, A., Bastida, F., Alonso, J.L., Marquinez, J., Aller, J., Alvarezmarron, J., Marcos, A., Pulgar, J.A., 1988. A thin-skinned tectonics model for an arcuate fold and thrust belt — the Cantabrian Zone (Variscan Ibero-Armorican Arc). Tectonics 7, 517–537.

Poirier J, 1980, Shear localization and shear instability in materials in the ductile field. J Struct Geol 2(1–2):135–142

Pysklywec, Russell N., Christopher Beaumont, and Philippe Fullsack. "Lithospheric deformation during the early stages of continental collision: Numerical experiments and comparison with South Island, New Zealand." *Journal of Geophysical Research: Solid Earth (1978–2012)* 107, no. B7 (2002): ETG-3.

Pysklywec, Russell N. "Surface erosion control on the evolution of the deep lithosphere." *Geology* 34, no. 4 (2006): 225-228.

Pysklywec, Russell N., Oguz Gogus, J. Percival, A. R. Cruden, and C. Beaumont. "Insights from geodynamical modeling on possible fates of continental mantle lithosphere: Collision, removal, and overturn." *Canadian Journal of Earth Sciences* 47, no. 4 (2010): 541-563.

Ranalli, G., Murphy, D.C., 1987. Rheological stratification of the lithosphere. Tectonophysics 132, 281–295.

Ranalli, Giorgio. "Rheology of the lithosphere in space and time." *Geological Society, London, Special Publications* 121, no. 1 (1997): 19-37.

Ries, A. C., and R. M. Shackleton, Patterns of strain variation in arcuate fold belts, Philos. Trans. R. Soc. London, Ser. A, 283, 281-288, 1976.

Rutter, E. H., and K. H. Brodie. "The role of tectonic grain size reduction in the rheological stratification of the lithosphere." *Geologische Rundschau* 77, no. 1 (1988): 295-307.

Schott, B., and H. Schmeling. "Delamination and detachment of a lithospheric root." *Tectonophysics* 296, no. 3 (1998): 225-247.

Schreurs, G., Buiter, S. J., Boutelier, D., Corti, G., Costa, E., Cruden, A. R., ... & Nilforoushan, F. (2006). Analogue benchmarks of shortening and extension experiments. *SPECIAL PUBLICATION-GEOLOGICAL SOCIETY OF LONDON*, *253*, 1.

Seeber, L., and J. G. Armbruster. "Some elements of continental subduction along the Himalayan front." *Tectonophysics* 105, no. 1 (1984): 263-278.

Shaw, J., Johnston, S.T., Gutierrez-Alonso, G., and Weil, A.B., 2012, Oroclines of the Variscan orogen of Iberia: Paleocurrent analysis and paleogeographic implications: Earth and Planetary Science Letters, v. 329–330, p. 60–70, doi:10.1016/j.epsl.2012.02.014.

Shemenda, Alexander I. *Subduction: Insights from physical modeling*. Dordrecht: Kluwer Academic Publishers, 1994.

Silver, E.A., Reed, D.L., Tagudin, J.E., and Heil, D.J., 1990, Implications of the north and south Panama thrust belts for the origin of the Panama orocline: Tectonics, v. 9, p. 261–281, doi:10.1029/TC009i002p00261.

Stehli, Francis G., and S. David Webb. "A kaleidoscope of plates, faunal and floral dispersals, and sea level changes." In *The great American biotic interchange*, pp. 3-16. Springer US, 1985.

Tatsumi, Y., Otofuji, Y. I., Matsuda, T., & Nohda, S. (1989). Opening of the Sea of Japan back-arc basin by asthenospheric injection. Tectonophysics, 166(4), 317-329.

Turcotte, D. L., and G. Schubert. "Geodynamics, 450." (1982).

Valverde-Vaquero, P., 1992, Permo-Carboniferous Magmatic Activity in the Cantabrian Zone (N.E. Iberian Massif, Asturias, NW Spain) [Ph.D. thesis]: Boston, Massachusetts, Boston College, 498 p.

Van der Voo, Rob. "Paleomagnetism, oroclines, and growth of the continental crust." *GSA Today* 14, no. 12 (2004): 4-9.

Webb, S.D., 1985, Late Cenozoic mammal dispersals between the Americas, *in* Stehli, F.G., and Webb, S.D., eds., The Great American Biotic Interchange: New York, Plenum Press, p. 357–386.

Weil, Arlo B., and Aviva J. Sussman. "Classifying curved orogens based on timing relationships between structural development and vertical-axis rotations." *Orogenic curvature: integrating paleomagnetic and structural analyses* 383 (2004): 1e16.

Weil, Arlo Brandon, Gabriel Gutiérrez-Alonso, and David Wicks. "Investigating the kinematics of local thrust sheet rotation in the limb of an orocline: a paleomagnetic and structural analysis of the Esla tectonic unit, Cantabrian–Asturian Arc, NW Iberia." *International Journal of Earth Sciences* 102.1 (2013): 43-60.

White S, Burrows S, Carreras J, Shaw N, Humphreys F, 1980, On mylonites in ductile shear zones. Struct Geol 2(1–2):175–187

Zulauf J., Zulauf G. (2004) – Rheology of plasticine used as rock analogue: the impact of temperature, composition and strain. *Journal of Structural Geology*. 26(4), 725- 737.

# Appendices

## LG-2012-A1 (18/09/2012)

**Materials :**

- *$Mantle_{over.}$ :* C5K2 old (ρ=0.98)
- *Crust:* $CN_{white}$ (ρ=0.86)
- *$Mantle_{Subd.}$ p:* C5K2 new (ρ=0.98)

**Temperatures :**

- *Labo:* 21.0
- *$Melting_{mantle}$ :* 65.0
- *Pouring:* 47.5
- *Surface:* 37.0
- *Asthenosphere:* 41.0

| Time | Actual | | Calibrated | |
|---|---|---|---|---|
| | Surface | Asthenosphere | Surface | Asthenosphere |
| 12:45 | 19.0 | 19.4 | 30.0 | 40.0 |
| 13:15 | 28.8 | 39.8 | 35.0 | 40.0 |
| 14:00 | 35.5 | 39.1 | 36.0 | 40.0 |
| 14:45 | 36.0 | 41.1 | 36.5 | 40.0 |
| 15:00 | 36.7 | 41.0 | 36.8 | 40.0 |
| 15:08 | 36.8 | 41.0 | START | |

**Stabilizes at** :

- 37.0 $^0$C
- 41.0 $^0$C

**Couplage :**

- *Ribbon-lithosphere:* high, poured over
- *Trench:* nothing

**Speed :**

- 125 µm/s
- *Moving from:* 430 mm *to:* 70 mm

**Cameras :**

- *1*: near computer
- *2*: 500 mm
- *3*: 455mm
- *4*: 455mm

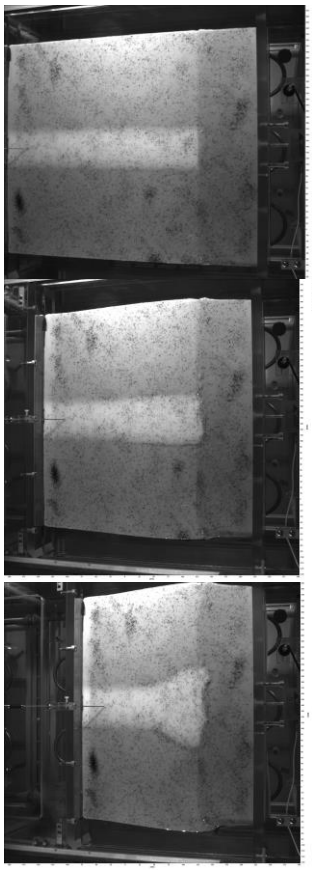

**Waterline / Calibration height :**

- 4.5 cm **/** 5.5 cm

**Calibration :**

- *Polynome #3 (a side is missing)*

**Calibration error and scale :**

| Camera | *RMS* | *Pix/mm* |
|---|---|---|
| **2** | 0.34 | 4.196 |
| **3** | 0.25 | 4.07 |
| **4** | 0.24 | 4.07 |

**Picture frequency :**

- 0.5 Hz

## Laboratory Comments

**Geometry and dynamism**
Low density mantle environment holding a crustal ribbon of low strength and high buoyancy. The ribbon enters the trench orthogonally, parallel to convergence. The ribbon-lithosphere coupling is strong as the mantle has been poured over the crust.

**Ductile extrusion**
The compressive stress is high but does not propagate enough, the strain expressed is too localized and the main deformation seems to be a lateral ductile extrusion of the crust, which does not go over the overriding plate.

**Coupling**
It seems like the coupling between the crust and the mantle was too strong. The ribbon would not move or deformed before getting fairly close to the trench (ductile localized strain). Hence, the stress would not propagate horizontally but rather be accommodated through lateral (parallel to the trench) extrusion over the subducting mantle. Probably, if the coupling was diminished, the curst would have reacted differently and the stress propagated a bit further, similarly if the crust material was more brittle to start with. The coupling was so good

**Density contrast**
Isostacy and a good coupling revealed the density variation between the mantle and the crust as the mantle was stretching up at its contact with the more buoyant crust. Hence, we could see an important curve (convex facing up) at the bottom of the mantle where the ribbon was floating. Even though the mantle was denser than the crust, it was lighter than the asthenosphere, permitting high horizontal compressive stresses at the convergence zone but low slab pull once in the asthenosphere.

# LG-2012-B1 (25/09/2012)

**Materials :**

- *$Mantle_{over.}$ :* C5K2 old (ρ=0.98)
- *Crust:* CN (ρ=0.86)
- *$Mantle_{Subd.}$* p: C5K2 new (ρ=0.98)

**Temperatures :**

- *Labo:* 22.0
- $Melting_{crust}$ : 60.0
- *$Melting_{mantle}$ :* 65.0
- *Pouring:* 47.5
- *Surface:* 37.0
- *Asthenosphere:* 41.0

| Time | Actual | | Calibrated | |
|---|---|---|---|---|
| | Surface | Asthenosphere | Surface | Asthenosphere |
| 13:00 | 20.0 | 20.0 | 30.0 | 40.0 |
| 13:30 | 29.9 | 31.6 | 35.5 | 40.0 |
| 14:15 | 35.6 | 39.8 | 36.0 | 40.0 |
| 15:00 | 35.8 | 41.0 | 36.5 | 40.0 |
| 15:15 | 36.7 | 40.9 | 36.8 | 40.0 |
| 15:28 | 37.0 | 40.9 | START | |

**Stabilizes at** :

- 37.0 $^0$C
- 41.0 $^0$C

**Couplage :**

- *Ribbon-lithosphere:* high, poured over
- *Trench:* nothing
- *Lateral faults:* paraffin oil

**Speed :**

- 250 µm/s
- *Moving from:* 430 mm *to:* 70 mm

**Cameras :**

- *1*: back left corner
- *2*: 500 mm
- *3*: 465 mm
- *4*: 465 mm

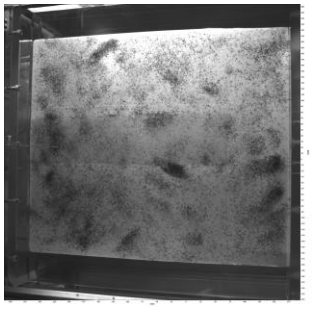

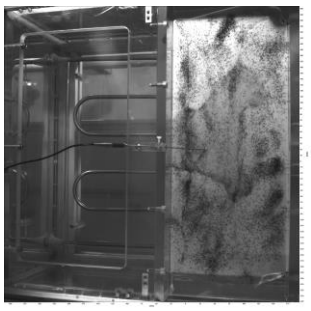

**Waterline / Calibration height :**

- 5.1 cm **/** 6.6 cm

**Calibration :**

- *Pin-hole*

**Calibration error and scale :**

| Camera | RMS | Pix/mm |
|---|---|---|
| 2 | -/- | 3.98 |
| 3 | 0.155 | 4.04 |
| 4 | 0.138 | 4.04 |

**Picture frequency :**

- 0.5 Hz

**Laboratory Comments**
**Geometry and dynamism**

This experiment, like LG-2012-A2 one, introduce a curved ribbon, but this time it is constrained by 2 lithospheric faults promoting the mantle of the continental ribbon to override the two lateral mantle plates.

**Results**

The compression was high enough to block any crust from being subducted. However instead of lateral displacements on the faults of the ribbon to accommodate shortening on the whole central plate, the compressive stress was expressed through ductile enlargement of the surface material before subduction. Such results were only possible because of the 2 free sides off the model and of the high buoyancy of the subducting plates, preventing any slab pull. An even more extensive (than LG-2012-A1) lateral extrusion was observed for the crust material which again deformed in a n extrusive manner preferentially on the side of the ribbon where the fault endorses overthrust of the lithophere (Left). Contrarily to experiment LG-2012-A1 and A2, there was a significant amount of crustal extrusion over the overriding plate, again preferentially on the side of the ribbon endorsing overthrust.

# LG-2012-A2 (27/09/2012)

**Materials :**

- *$Mantle_{over.}$ :* C5K2 old (ρ=0.98)
- *Crust:* CN (ρ=0.86)
- *$Mantle_{Subd.}$* p: C5K1 (ρ=1.30)

**Temperatures :**

- *Labo:* 22.0
- *Melting :* 65.0
- *Pouring overriding:* 47.5 *subducting + crust* 51.0
- *Surface:* 36.0
- *Asthenosphere:* 40.0

| Time | Actual | | Calibrated | |
|---|---|---|---|---|
| | Surface | Asthenosphere | Surface | Asthenosphere |
| 12:30 | 23.0 | 23.0 | 30.0 | 39.0 |
| 13:15 | 30.5 | 36.9 | 32.0 | 39.0 |
| 13:45 | 32.6 | 39.5 | 33.0 | 39.0 |
| 14:00 | 33.1 | 39.8 | 34.0 | 39.0 |
| 14:20 | 34.1 | 40.0 | 35.0 | 39.0 |
| 14:30 | 35.1 | 40.0 | 35.5 | 39.0 |
| 14:45 | 35.5 | 39.7 | 35.8 | 39.0 |
| 14:52 | 35.8 | 39.7 | START | |

**Curvature :**

- 40 cm radius

**Couplage :**

- *Ribbon-lithosphere:* paraffin oil
- *Trench:* paraffin oil

**Speed :**

- 125 µm/s
- Moving *from:* 430 mm *to:* 70 mm

**Cameras :**

- *1*: back left corner
- *2*: 500 mm
- *3*: 478 mm
- *4*: 478 mm

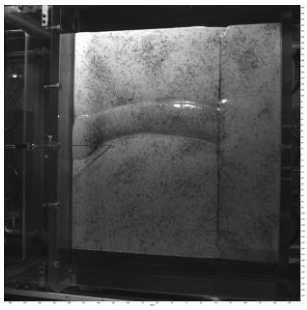

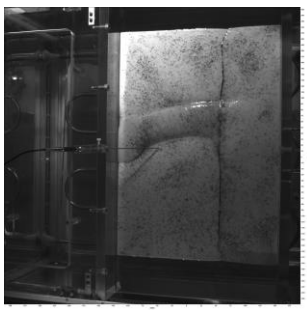

**Waterline / Calibration height :**

- 6.3 cm **/** 7.8 cm

**Calibration :**

- *Pin-hole*

**Calibration error and scale :**

| Camera | RMS | Pix/mm |
|---|---|---|
| 2 | 0.367 | 4.111 |
| 3 | 0.174 | 4.059 |
| 4 | 0.179 | 4.059 |

**Picture frequency :**

- 0.5 Hz

## Laboratory Comments

**Geometry and dynamism**

In this experiment, we chose a higher density for the subducting lithosperic mantle. This would potentially prevent the lithospheric enlargement seen in LG-2012-A1 and LG-2012-B1, the slab will pull strongly enough so the compressive stress is all focalised on the crustal material. We also tried to minimize coupling between the lithospheric mantle and the crust by simply deposing the later on the first, after a paraffin oil lubrication of the interface. To promote buckling, we gave an initial curvature (radius of 40cm) to the ribbon and placed it on the mantle lithosphere so that at its middle, the tangent was parallel to convergence. We kept both the asthenosphere and the surface temperatures relatively low to try to create a more brittle environment for the crust and prevent an extrusive ductile deformation. We rely on isostasy to ensure that the crust sinks enough to avoid that the overriding plate cuts through the crust-lithosphere interface.

**Results**

Indeed, negative buoyancy of the subducting slab being significant, the convergence did not lead to ductile lateral enlargement this time, but was accommodated by slab subduction. Once again, the crust mainly behaved as ductile except for the rotation (anticlockwise) of a whole block near the end of the experiment, we observed two faults overthrusting the block on two extremities. For the first time, probably because of the more dynamic and less compressive state of the model, some crustal material was subducted, but once passed the trench, as the hotter and denser water got in contact, the crust viscously floated under the overriding plate and accumulated there. 3D calculations show a topographic high where occurred this accumulation of crustal material, in the trench and under the overriding plate. Through time, the topographic high composed by the ribbon and the trench crustal accumulation is progressively shrinking parallel to convergence and the interlimb angle of around $50^0$ at the beginning evolved to an estimated curvature of $180^0$. However, this quick increase in curvature seems less attributable to vertical axis bending than to one direction shortening of an already curved orogen. The horizontal force on the captor was considerably high which might be attributed to the bending resistance of the subducting lithosphere, promoted by the colder temperature. The low heat budget was also shown in the subducting lithosphere where, as it was bending, many extensive strike-parallel faults appeared on the upper side of the plate.

# LG-2012-A3 (11/10/2012)

**Materials :**

- *$Mantle_{over.}$ :* C5K2 old (ρ=0.99)
- *$Mantle_{Subd\text{-}plate.}$* : C5K2 new (ρ=0.99)
- *$Mantle_{Subd\text{-}plate\text{-}tip.}$* : C5K1 (ρ=1.30)
- *Crust*: C5B (ρ=0.86, strongest)
- *Mantle-crust interface*: C6 (ρ=0.86, weakest)

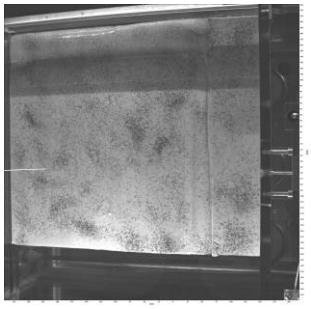

**Temperatures :**

- *Labo:* 22.6
- *Melting :* 65.0
- *Pouring:* 47.5
- *Surface:* 36.5
- *Asthenosphere:* 40.5

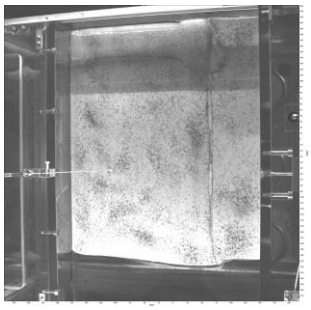

| Time | Actual | | Calibrated | |
|---|---|---|---|---|
| | Surface | Asthenosphere | Surface | Asthenosphere |
| 11:50 | 21.0 | 23.0 | 30.0 | 39.5 |
| 12:20 | 30.0 | 34.2 | 34.0 | 39.5 |
| 12:40 | 33.9 | 37.6 | 34.5 | 39.5 |
| 13:10 | 35.1 | 40.1 | 35.7 | 39.5 |
| 13:30 | 35.6 | 40.4 | 36.2 | 39.5 |
| 13:45 | 36.3 | 40.6 | START | |

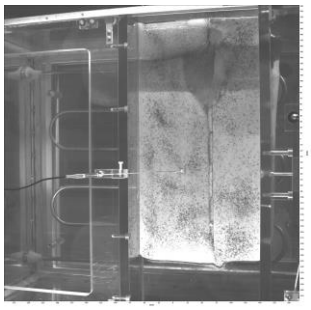

**Stabilizes at** :

- 35.6 $^0$C
- 40.2 $^0$C

**Couplage :**

- *Mantle-Crust*: Low strength 2mm layer of crustal material
- *Trench*: paraffin oil
- *Mantle-side of tank*: nothing

**Speed :**

- 250 µm/s
- *Moving from:* 430 mm *to:* 70 mm

**Cameras :**

- *1*: back left corner
- *2*: 500 mm
- *3*: 503 mm
- *4*: 503 mm

**Waterline / Calibration height :**

- 88 cm **/** 1.03 cm

**Calibration :**

- *Pin-hole*

**Calibration error and scale :**

| Camera | RMS | Pix/mm |
|---|---|---|
| 2 | 0.315 | 3.97 |
| 3 | 0.149 | 4.01 |
| 4 | 0.158 | 4.01 |

**Picture frequency :**

- 0.5 Hz

**Laboratory Comments**
**Geometry and dynamism**

We are on the way to get a new piston that does not cover the whole tank and that would allow us to isolate a portion of the plates from compressive stress. Until then, the best to do in order to model a stable lateral continent is to use one of the tank sides. We will put our crust just next to the Plexiglas and that way, the ribbon should be totally constricted on one side. We taught about using the lighter lithospheric material to embody the mantle and to use our new more resistant material for the crust that will be 1.5 cm (52km) thick. We were planning on minimizing the crust-mantle coupling but not on building any lateral fault. We did add a really thin (2mm) layer of C6 material (red) the lowest strength material we have. This should ensure that the coupling between crust and lithosphere is at his very lowest. To ensure that the crust enter the trench and doesn't just accretes on top of overriding plate we did cut the crustal frontal tip on a very progressive slope.

**Results**

The weak interface layer succeeded at minimizing the crust-mantle coupling, as almost no crust did get subducted. The crust behaved with less ductility this time as instead of only ductile extrusion, the shortening was also accommodated through several overthrusts (average dip of maybe $60^0$). Overthrust deformation as is seen in this model is probably triggered by the downward motion of our subducting plate. Even though we encountered brittle behaviour, once again, the deformation is very localized at the frontal tip of the ribbon; hence no buckling and hardly any evident vertical axis bending. We need to find a way to propagate the stress on the whole plate, it seems that the buckling phenomena can't only be constrained to the crustal level, where the deformation is too localized, but has to get the underlying mantle involved.

# LG-2012-B2 (05/10/2012)

**Materials :**

- *$Mantle_{over.}$ :* C5K2 old (ρ=0.98)
- *Crust:* CN (ρ=0.86)
- *$Mantle_{LateralSubd}$* : C5K1 (ρ=1.30)
- *$Mantle_{CentralSubd.}$:* C5K2 new (ρ=0.98)

**Temperatures :**

- *Labo:* 21.5
- *$Melting_{mantle}$ :* 65.0
- *Pouring:* 47.5
- *Surface:* 36.5
- *Asthenosphere:* 40.5

| Time | Actual | Calibrated | | |
|---|---|---|---|---|
| | Surface | Asthenosphere | Surface | Asthenosphere |
| 11:45 | 20.6 | 20.6 | 30.0 | 39.5 |
| 12:15 | 28.7 | 32.3 | 31.0 | 39.5 |
| 13:00 | 33.4 | 39.7 | 33.0 | 39.5 |
| 13:25 | 33.4 | 40.5 | 34.5 | 39.5 |
| 13:40 | 34.5 | 40.6 | 35.5 | 39.5 |
| 13:50 | 35.7 | 40.5 | 36.0 | 39.5 |
| 13:55 | 35.9 | 40.5 | 36.3 | 39.5 |
| 14:00 | 36.5 | 40.5 | START | |

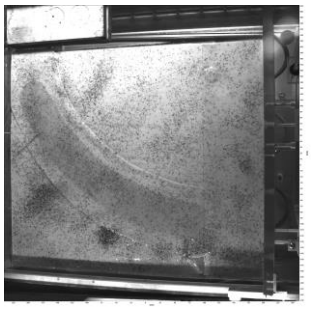

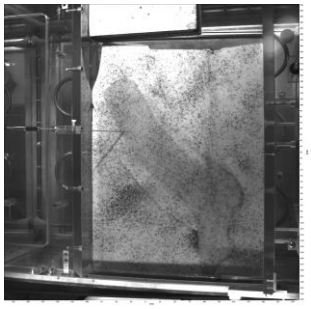

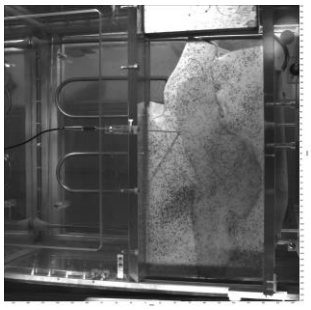

**Stabilizes at** :

- 36.8 $^0$C
- 40.5 $^0$C

**Curvature :**

- 40 cm radius (crust and central lithosphere)

**Couplage :**

- *Ribbon-lithosphere:* high, poured over
- *Trench:* nothing
- *Lateral faults:* paraffin oil

**Speed :**

- 250 µm/s
- *Moving from:* 430 mm *to:* 170 mm

**Cameras :**

- *1*: back left corner
- *2*: 500 mm
- *3*: 465 mm
- *4*: 465 mm

**Waterline / Calibration height :**

- 5.2 cm **/** 6.7 cm

**Calibration :**

- *Pin-hole*

**Calibration error and scale :**

| Camera | RMS | Pix/mm |
|---|---|---|
| 2 | 0.34 | 4.196 |
| 3 | 0.25 | 4.07 |
| 4 | 0.24 | 4.07 |

**Picture frequency :**

- 0.5 Hz

**Laboratory Comments**
**Geometry and dynamism**

This experiment, like LG-2012-A2 one, introduce a curved ribbon, but this time it is constrained by 2 lithospheric faults promoting the mantle (low density) of the continental ribbon to override the two lateral mantle plates (high density). This time, the curve plate is placed so at its trench extremity, the tangent is parallel to convergence.

**Results**

The fourth experiment did not express much buckling or bending. The crust behaved as ductile and extruded on the sides and over the overriding plate. No crust was subducted, but the light lithospheric mantle was, pulled by the 2 other heavier plates. The lateral faults where not activated even though well lubricated until the very end when the dense slab is finally detached from the concave side of the curved ribbon.

The main rotational feature observed was the rotation of the concave heavy plate in a clockwise manner as the free size encountered a significant lesser amount of resistance to subduction than the one coupled to the low density central lithospheric plate.

# LG-2012-C1 (18/10/2012)

**Materials :**

- $Mantle_{over.}$ *:* C5K2 old (ρ=0.98)
- $Mantle_{subduct.}$: C5K1 (ρ=1.30)
- $Mantle_{Stable\ Continent.}$: C5K2 new (ρ=0.98)
- $Mantle_{Ribbon}$ : C5K2 (ρ=0.98)

**Temperatures :**

- *Labo:* 21.5
- $Melting_{mantle}$ *:* 65.0
- *Pouring:* 47.5
- *Surface:* 36.5
- *Asthenosphere:* 40.5

| Time | Actual | | Calibrated | |
|---|---|---|---|---|
| | Surface | Asthenosphere | Surface | Asthenosphere |
| 12:10 | 21.6 | 22.5 | 30.0 | 39.5 |
| 12:40 | 29.5 | 34.2 | 34.0 | 39.5 |
| 13:00 | 33.4 | 37.7 | 35.0 | 39.5 |
| 13:20 | 35.5 | 39.5 | 35.5 | 39.5 |
| 13:40 | 35.9 | 40.6 | 36.2 | 39.5 |
| 13:50 | 36.0 | 40.5 | 36.4 | 39.5 |
| 14:00 | 36.6 | 40.5 | START | |

**Stabilizes at** :

- 36.8 $^0$C
- 40.5 $^0$C

**Couplage :**

- *Medium nothing everywhere*

**Speed :**

- 250 µm/s
- *Moving from:* 430 mm *to:* 170 mm

**Cameras :**

- *1*: back left corner
- *2*: 500 mm
- *3*: 477 mm
- *4*: 477 mm

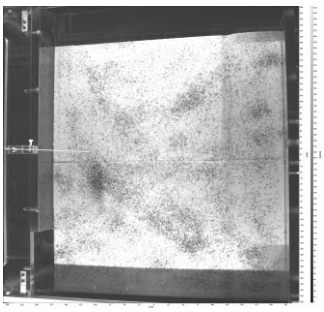

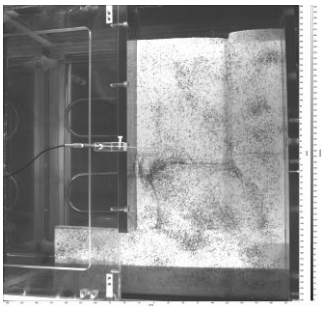

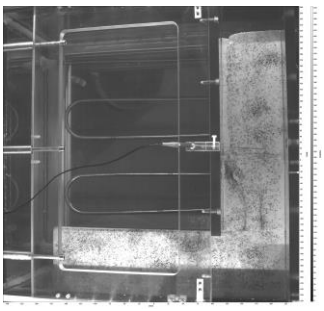

## Waterline / Calibration height :

- 6.2 cm **/** 7.7 cm

## Calibration :

- *Pin-hole*

## Calibration error and scale :

| Camera | RMS | Pix/mm |
|---|---|---|
| 2 | 0.235 | 4.06 |
| 3 | 0.173 | 4.05 |
| 4 | 0.155 | 4.05 |

## Picture frequency :

- 0.5 Hz

## Laboratory Comments

**Geometry and dynamism**

A common tendency in the past experiments is for crustal deformation not to propagate in the plate through vertical axis bending but rather to be localized near the convergence zone, as ductile extrusions or as overthrusting. It seems that the crust alone does not have the ability to buckle, and that a stronger bigger part of the lithosphere must be involved. The lateral subducting plates have high power of entrainment for a continental ribbon (as seen in LG-2012-B1 and B2). A good way to prevent the ribbon from subducting is to block his access to the trench. The shortening ribbon will be constrained to the right by a stable continental plate (now that we have our new piston) and to the left by a subducting mantle plate. The ribbon could override the subducting plate and be divided from continental plate by a strike-slip fault. Such constraints on the ribbon extremities are quite radical, but it will prevent any subduction of the ribbon and lower its risks to overthrust (Overthrust deformation in LG-2012-A3 is probably triggered by the downward motion of our subducting plate). Once we mastered the art of buckling a stripe of ribbon, we can start considering changing the dynamics and evolve from straight horizontal compression to subduction zone compression.

**Results**

Even though the last model turned out to be quite interesting and our new piston to work properly, it did not produce any vertical bend. The shortening was accommodated at first at the ribbon's two tips through material widening and thickening, shortly after, 2 thrust faults were formed only 4 to 5 centimetres away from each extremities. The two faults initiate on the side of the stable continental and propagate across the ribbon. The fault is completely orthogonal to the ribbon next to the piston but is oblique on the other side as the fault propagated directly towards the triple junction. Once the two faults are completed, all the shorthening is contained by the two subduction zones in two opposite directions (away from the center). The bend in the ribbon is substantial, only, it is on a horizontal axis.The fold is practically only formed from compressive stress since the slab pull can't be obtain in a lithosphere of asthenosphere density. Maybe could we produce oroclinal if we constrained a ribbon to similar faults (subduction-like) only with the axis orthogonally turned in a vertical direction.

# LG-2012-C2 (31/10/12)

**Materials :**

- *Ribbon* : C5K2 old (ρ=0.98)
- $Mantle_{Subducting}$: C5K1 (ρ=1.30)

**Temperatures :**

- *Labo:* 22.6
- $Melting_{mantle}$ *:* 65.0
- *Pouring:* 47.5
- *Surface:* 36.5
- *Asthenosphere:* 40.0

| Time | Actual | | Calibrated | |
|---|---|---|---|---|
| | Surface | Asthenosphere | Surface | Asthenosphere |
| 11:10 | 23.0 | 24.2 | 30.5 | 39.0 |
| 11:30 | 29.5 | 31.8 | 32.5 | 39.0 |
| 11:45 | 32.7 | 35.3 | 34.5 | 39.0 |
| 12:15 | 34.5 | 39.0 | 35.5 | 39.0 |
| 12:35 | 35.5 | 39.7 | 36.3 | 39.0 |
| 12:55 | 36.7 | 40.0 | START | |

**Stabilizes at** :

- 36.5 $^0$C
- 40.0 $^0$C

**Couplage :**

- *Paraffin oil*

**Speed :**

- 125 µm/s
- *Moving from:* 430 mm *to:* … mm

**Cameras :**

- *1*: back left corner
- *2*: 500 mm
- *3*: 465 mm
- *4*: 465 mm

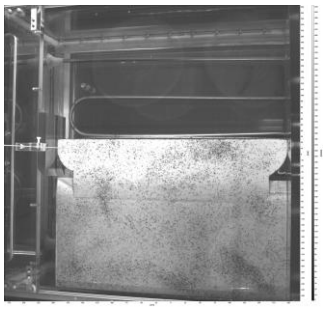

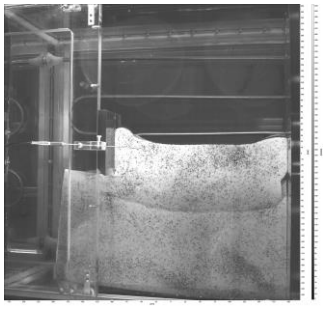

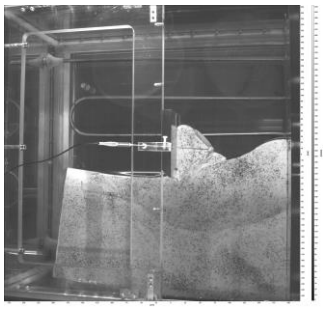

**Waterline / Calibration height :**

- 5.0 cm **/** 6.5 cm

**Calibration :**

- *Pin-hole*

**Calibration error and scale :**

| Camera | RMS | Pix/mm |
|---|---|---|
| 2 | 0.346 | 4.041 |
| 3 | 0.166 | 4.068 |
| 4 | 0.162 | 4.068 |

**Picture frequency :**

- 0.5 Hz

**Laboratory Comments**
**Geometry and dynamism**

We have built a piston small enough too push only on the ribbon. The first experiment this week (LG-2012-C2) introduced only a ribbon (the curved cut corners ribbon from LG-2012-D1) and a thin plate separated by a subduction zone on the side where the ribbon is expected to bend. From experiment LG-2012-D1, we will keep the configuration of the ribbon #1 (the one with curved cut corners), the one which expressed lateral deformation first. However, this time, the ribbon will be constrained on one side (the side of expected bending) by a thin dense plate. A subduction zone dipping towards the ribbon will separate the 2 plates. For the first experiment, we want to keep the other side free.

**Manipulation mistake**

For the oceanic plate, I took the 9 cm radius blade instead of the 7 cm one. The gap between the plate and the ribbon filled in while the model was warming up.

**Results**

A noticeable bend (around $130^0$ interlimb angle) formed and the ribbon managed to significantly override the thin lithospheric plate, which began to subduct in the middle. Once the limb in contact with the piston had obtained enough obliquity with respect to convergence, a strike-slip fault forms and the shortening could no longer be accommodated by buckling but only through the ribbon's tip translation. We thought that maybe such vertical fault would have been prevented if a stable continent was laterally constraining the tips of our ribbon. Some localized shear extension was observed on the ribbon near the contact with the other plate.

# LG-2012-C3 (01/11/12)

**Materials :**

- *Ribbon* : C5K2 new (ρ=0.98)
- *Mantle$_{Subducting}$*: C5K1 (ρ=1.30)
- *Stable Continent*: C5K2 new (ρ=0.98)

**Temperatures :**

- *Labo:* 21.1
- *Melting$_{mantle}$ :* 65.0
- *Pouring:* 47.5
- *Surface:* 36.5
- *Asthenosphere:* 40.0

| Time | Actual | | Calibrated | |
|---|---|---|---|---|
| | Surface | Asthenosphere | Surface | Asthenosphere |
| 12:08 | 23.4 | 24.6 | 31.0 | 39.0 |
| 12:36 | 30.6 | 34.2 | 33.0 | 39.0 |
| 12:53 | 33.6 | 37.2 | 34.5 | 39.0 |
| 13:15 | 34.8 | 39.0 | 35.5 | 39.0 |
| 13:35 | 35.7 | 39.4 | 36.0 | 39.0 |
| 13:45 | 36.1 | 39.9 | 36.5 | 39.0 |
| 14:00 | 36.7 | 40.0 | START | |

**Stabilizes at** :

- 36.7 $^{0}$C
- 40.0 $^{0}$C

**Couplage :**

- *Paraffin oil at both interfaces*

**Speed :**

- 125 µm/s
- *Moving from:* 430 mm *to:* … mm

**Cameras :**

- *1*: back left corner
- *2*: 500 mm
- *3*: 467 mm
- *4*: 467 mm

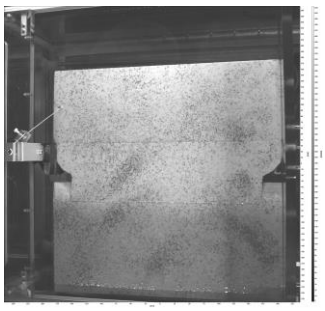

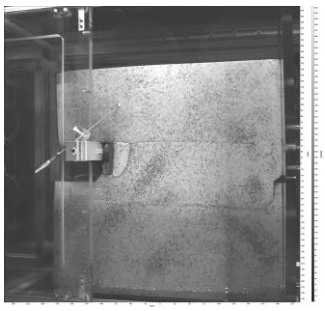

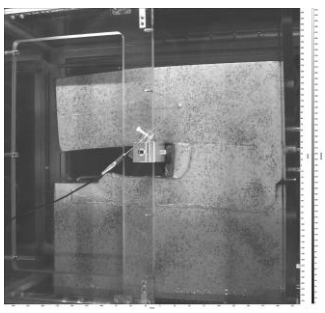

**Waterline / Calibration height :**

- 5.2 cm **/** 6.7 cm

**Calibration :**

- *Pin-hole*

**Calibration error and scale :**

| Camera | RMS | Pix/mm |
|---|---|---|
| 2 | 0.366 | 4.028 |
| 3 | 0.161 | 4.063 |
| 4 | 0.160 | 4.063 |

**Picture frequency :**

- 0.5 Hz

**Laboratory Comments**
**Geometry and dynamism**

In this experiment we will try to constrain the other side with a stable continental ribbon. This should reduce the lateral constraints without completely removing them Our second experiment was exactly the same but with a stable continent on the other side of the ribbon (the small piston is still pushing only on the ribbon). Apart from this, the only other differences from LG-2012-C2 are the use of C5K2 New (instead of old) and the use of a smaller piston that is in contact only with the ribbon and that force us to put the thermometer in the continental plat instead (thus the temperature a bit higher… the thermometer was fairly close to the hot side). Also because of the piston geometry, the subduction zone was 4mm away from being completely closed before the start of the experiment.

**Results**

It seams that the lateral constraints were too strong because this time, shortening was accommodated by vertical growth of the ribbon's tips and then by a thrust fault striking orthogonally to convergence allowing the ribbon to subduct. The results were quite similar to LG-2012-C1 except that subduction was restrained to only one side. So, as we added a second constraint, (necessity of lateral extension on a vertical fault) the ribbon lost its ability to buckle. Was the stable continent enough to stop the bend or was it rather a combination of the two plates?

# LG-2012-D1 (24/10/2012)

**Materials :**

- *Ribbons* : C5K2 new (ρ=0.98)

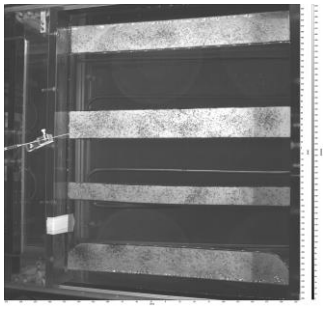

**Temperatures :**

- *Labo:* 21.6
- *Melting$_{mantle}$ :* 65.0
- *Pouring:* 47.5
- *Surface:* 36.5
- *Asthenosphere:* 40.0

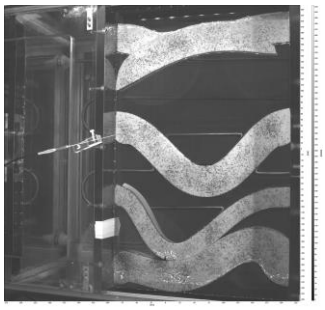

| Time | Actual | | Calibrated | |
|---|---|---|---|---|
| | Surface | Asthenosphere | Surface | Asthenosphere |
| 11:00 | 21.6 | 22.0 | 30.5 | 39.0 |
| 11:25 | 29.3 | 31.8 | 32.5 | 39.0 |
| 11:45 | 33.3 | 36.2 | 34.0 | 39.0 |
| 12:05 | 34.5 | 38.4 | 35.0 | 39.0 |
| 12:25 | 35.6 | 39.6 | 36.3 | 39.0 |
| 12:42 | 36.3 | 39.9 | 36.3 | 39.0 |
| 12:50 | 36.5 | 40.0 | START | |

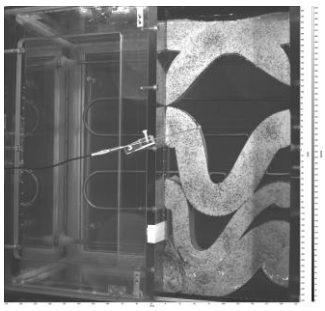

**Stabilizes at** :

- 36.5 $^{0}$C
- 40.0 $^{0}$C

**Couplage :**

- *No plate interaction (until lateral bending make them touch)*

**Speed :**

- 125 µm/s
- *Moving from:* 430 mm *to:* … mm

**Cameras :**

- *1*: back left corner
- *2*: 500 mm
- *3*: 472 mm
- *4*: 472 mm

**Waterline / Calibration height :**

- 5.7 cm **/** 7.2 cm

**Calibration :**

- *Pin-hole*

**Calibration error and scale :**

| Camera | RMS | Pix/mm |
|---|---|---|
| 2 | 0.313 | 4.056 |
| 3 | 0.137 | 4.00 |
| 4 | 0.172 | 4.00 |

**Picture frequency :**

- 0.5 Hz

**Laboratory Comments**
**Geometry and dynamism**

This week, for efficiency reasons, we think about trying a series of experiments on linear ribbons and how they react to direct horizontal compressive stress. To simplify the model we will just put the lithospheric ribbons straight into the astenosphere, no surrounding plates, this is a considerable simplification, but it will allow us to try 3 or 4 ribbons at a time and save us some precious time. Furthermore, the freedom on the sides of the ribbons will promote buckling formation. We will add lateral constraints for the ribbon and a real subduction zone only once, in these experiments, we really define the best initial geometry for vertical axis ribbon bending. Joined is a picture of some of the ribbon geometries we consider testing. All these ribbons will share the same dimensions (40 x 5 x 3 cm), the difference will lie in inherited geometric features.

1. **Curved vertical faults**

   Curved vertical faults could bend the ribbon on a vertical axis the way the thrust faults in LG-2012-C1 bent the ribbon on a horizontal axis.

2. **Thick an narrow ribbon**

   To explore the effects of height vs width ratio. A ribbon twice as thick as its width

3. **Curved-cut corners**

   Such ribbon geometry should initiate the buckle as the compression start on one side only (to the right). There is the possibility to add some pre-cut extension faults to the left to facilitate extension. It is also possible to consider lithospheric thinning at the center of the ribbon on the right side, which would promote deformation (bending) at the center instead of the extremities (thrust faults or oblique strike-slips). Unless you think such differential thinning or pre-cut faulting is not relevant.

4. **Pastor-Galan**

we build our fourth model exactly as #2 except to place it horizontally in the tank.

**Results**

Our 4 ribbons did produce vertical axis bends, so much that it didn't take long before they start interacting with each others. The first ribbon to express lateral deformation was #3. The stronger bend, overall, was #2 but we might not stick to such geometry since the width vs height ratio is not so realistic. All the bends showed lithospheric vertical growth on the inner side.

Overall, we see that freedom on the sides substantially helps the buckling. Therefore we plan on reducing the lateral constraints in our future experiments

# LG-2012-C4 (07-11-12)

**Materials :**

- *Free Ribbon* : C5K2(ρ=0.98)
- *Stable continent*: C5K2 New (ρ=0.98)
- *Constrained Ribbon* : C5K2 New (ρ=0.98)

**Temperatures :**

- *Labo:* 22.0
- *Melting$_{mantle}$ :* 65.0
- *Pouring:* 47.5
- *Surface:* 36.5
- *Asthenosphere:* 40.0

| Time | Actual | | Calibrated | |
|---|---|---|---|---|
| | Surface | Asthenosphere | Surface | Asthenosphere |
| 11:24 | 22.5 | 22.5 | 30.0 | 39.0 |
| 11:37 | 31.0 | 34.0 | 32.0 | 39.0 |
| 12:10 | 32.1 | 36.0 | 33.5 | 39.0 |
| 12:25 | 33.7 | 37.7 | 34.5 | 39.0 |
| 12:40 | 34.6 | 39.2 | 35.5 | 39.0 |
| 12:58 | 35.7 | 39.9 | 36.2 | 39.0 |
| 13:12 | 37.5 | 40.0 | 36.5 | Start |

**Stabilizes at** :

- 36.8 $^{0}$C
- 39.6 $^{0}$C

**Couplage :**

- *None*

**Speed :**

- 125 µm/s
- **Moving** *from:* 430 mm

**Cameras :**

- *1*: 500 mm
- *2*: back left
- *3*: 462 mm
- *4*: 462 mm

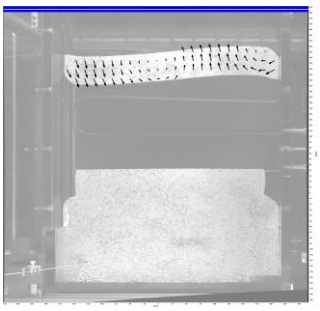

**Waterline / Calibration height :**

- 4.7 cm **/** 6.2 cm calibration error (306+94-400+4.7+1.5)

**Calibration :**

- *Pin-hole*

**Calibration error and scale :**

| Camera | RMS | Pix/mm |
|---|---|---|
| 1 | 186 | 4.033 |
| 3 | 162 | 3.99 |
| 4 | 160 | 3.99 |

**Picture frequency :**

- 0.5 Hz

**Laboratory Comments**
**Geometry and dynamism**

In order to ascertain whether or not the continent alone (with a vertical fault) is enough to prevent buckling, I made an experiment where the exact same ribbon would only be constrained by the continent and nothing on the other side.

I also try a second experiment introducing different geometries of ribbons placed straight in the water (Alike experiment LG-2012-D1).

**Results**

Two ribbons, one with the same ribbon as for previous week (C2 and C3) but this time only in contact with a stable continent on one side (free on the other). The two plates were separated by a thick strike-slip. Shearing (through the strike slip) between the 2 plates was quite effective, however, buckling was substancially harder to produce and there would not be more lateral displacement than in experiment C3. Therefore, from these results, we confirm that horizontal extension is really hard to obtain orthogonally to a strike-slip fault.

# LG-2012-C5 (09/11/12)

**Materials :**

- *Ribbon* : C5K2 New(ρ=0.98)
- *Mantle$_{Subducting}$*: C5K1 (ρ=1.03)
- *Stable Continent*: C5K2 New (ρ=0.98)

**Temperatures :**

- *Labo:* 24.2
- *Melting$_{mantle}$ :* 65.0
- *Pouring:* 47.5
- *Surface:* 36.5
- *Asthenosphere:* 40

| Time | Actual | | Calibrated | |
|---|---|---|---|---|
| | Surface | Asthenosphere | Surface | Asthenosphere |
| 11:00 | 21.3 | 21.1 | 30.0 | 39.0 |
| 11:30 | 30.0 | 31.0 | 32.0 | 39.0 |
| 11:42 | 32.3 | 34.3 | 33.0 | 39.0 |
| 11:58 | 33.6 | 36.9 | 34.5 | 39.0 |
| 12:12 | 34.9 | 38.5 | 35.5 | 39.0 |
| 12:26 | 36.2 | 39.5 | 36.0 | 39.0 |
| 12:40 | 36.6 | 39.9 | 36.3 | 39.0 |
| 12:47 | 36.5 | 40.0 | 36.3 | START |

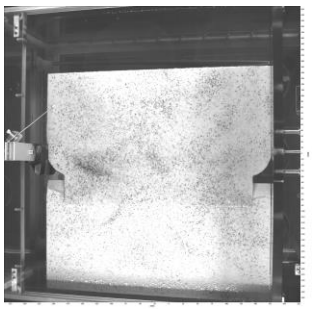

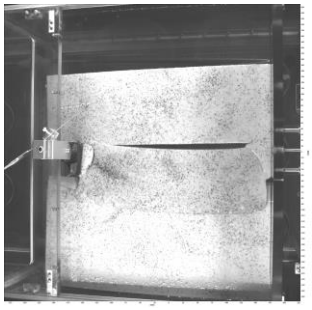

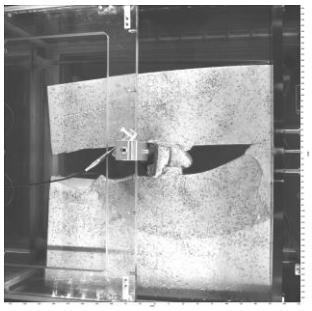

**Couplage :**

- *Paraffin oil at subduction zone*

**Speed :**

- 125 µm/s
- *Moving from:* 430 mm *to:* … mm

**Cameras :**

- *1*: 500 mm
- *2*: back left
- *3*: 470 mm
- *4*: 470 mm

**Waterline / Calibration height :**

- 5.5 cm **/** 7.0 cm

**Calibration :**

- *Pin-hole*

**Calibration error and scale :**

| Camera | RMS | Pix/mm |
|---|---|---|
| 1 | 0.136 | 4.05 |
| 3 | 0.159 | 3.98 |
| 4 | 0.154 | 3.98 |

**Picture frequency :**

- 0.5 Hz

**Laboratory Comments**
**Geometry and dynamism**

To promote extension next to the core of our ribbon, we did create a back arc basin. Thus, only a very thin (2mm) layer of material divides the 2 plates. We were fairly confidant that the ribbon would bend, so we also added a thin underthrusted oceanic lithosphere on the outer arc like in C2 and C3 (see sketches).

**Results**

The results of this experiment are very similar to those from C2 which has no continental plate at all. Indeed, our ribbon bends in the direction predicted and force a significant part of the underthrusting oceanic lithosphere to subduct. Once the piston's end of the ribbon has rotated to a substantial angle, the narrow piston create the necessary differential forcing to form a strike slip (starting at the pistons extremity) almost parallel to shortening, preventing the ribbon to buckle to higher angles. We believe that such issue would not be the case with a larger piston, since as the limb rotates it enters progressively in contact with the advancing piston.

Model C7 is another alternative to insure that the underthrusted plate accommodate (through subduction) all the shortening produced by the piston. We already discussed on the possibility of a similar ribbon undergoing a rapid orthogonal axis turn. The angle is exaggerated to 90 degrees, if it works well, we could consider some smaller angles. The underthrusted plate subducts under both ribbon limbs allowing shortening of the oceanic plate and buckling of the ribbon.

Experimental time runs short, I have to decide if I continue to try various model geometries or if we rather start playing with our most successful models, changing different variables (speed, temperature, plate thicknesses).

# LG-2012-C6 (14/11/12)

**Materials :**

- *Ribbon* : (ρ=0.98)*Crust:* CN (ρ=0.86)
- $Mantle_{Subducting}$: (ρ=1.03)
- *Stable Continent*: (ρ=0.98)

**Temperatures :**

- *Labo:* 21.5
- $Melting_{mantle}$ *:* 65.0
- *Pouring:* 47.5
- *Surface:* 40.0
- *Asthenosphere:* 36.5

| Time | Actual | | Calibrated | |
|---|---|---|---|---|
| | Surface | Asthenosphere | Surface | Asthenosphere |
| 11:15 | 20.6 | 24.0 | 30.0 | 39.0 |
| 11:39 | 30.8 | 33.0 | 32.0 | 39.0 |
| 11:52 | 32.6 | 35.6 | 33.0 | 39.0 |
| 12:03 | 33.6 | 37.9 | 34.2 | 39.5 |
| 12:16 | 34.4 | 38.8 | 35.2 | 39.5 |
| 12:38 | 35.0 | 40.3 | 36.2 | 39.5 |
| 12:50 | 36.9 | 40.5 | 36.2 | 39.5 |
| 1:00 | 36.9 | 40.6 | START | |

**Stabilizes at** :

- 36.7 $^0$C
- 40.5 $^0$C

**Couplage :**

- *Paraffin oil between ribbon and underthrust*

**Speed :**

- 125 µm/s
- *Moving from:* 430 mm *to:* … mm

**Cameras :**

- *1*: back left
- *2*: 500 mm
- *3*: 460 mm
- *4*: 460 mm

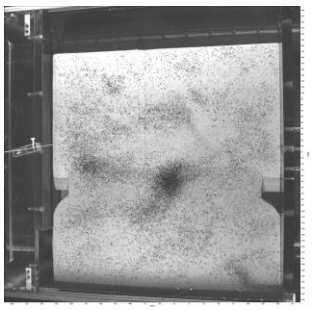

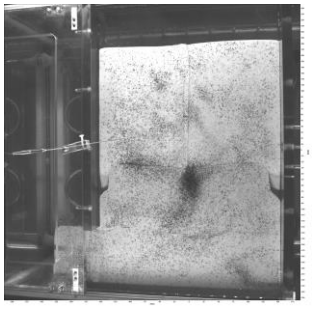

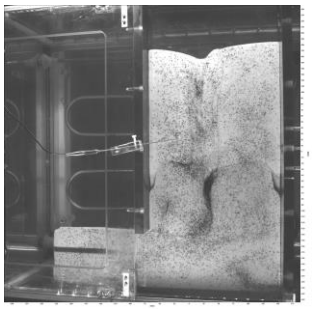

**Waterline / Calibration height :**

- 4.5 cm **/** 6.0 cm

**Calibration :**

- *Pin-hole*

**Calibration error and scale :**

| Camera | RMS | Pix/mm |
|---|---|---|
| 2 | 0.449 | 3.96 |
| 3 | 0.184 | 4.078 |
| 4 | 0.179 | 4.078 |

**Picture frequency :**

- 0.5 Hz

**Laboratory Comments**
**Geometry and dynamism**

I suggest two models that allow a larger piston. We will simply add a way for the thin underthrusted oceanic lithosphere to accommodate the shortening created by the piston. Thus, near its first third, we will pre-cut a subduction zone. Hopefully such a thrust fault in the underthrusted plate will not propagate into the ribbon and will instead facilitate the ribbon's overthrust.

# LG-2012-C7 (16/11/12)

**Materials :**

- *Ribbon* : C5K2 New (ρ=0.98)

**Temperatures :**

- *Labo:* 24.0
- *Melting:* 65.0
- *Pouring:* 47.5
- *Surface:* 37.5
- *Asthenosphere:* 36.5

| Time | Actual | | Calibrated | |
|---|---|---|---|---|
| | Surface | Asthenosphere | Surface | Asthenosphere |
| 4:10 | 21.9 | 21.2 | 31.0 | 39.0 |
| 4:43 | 31.4 | 32.5 | 32.2 | 39.0 |
| 4:53 | 33.0 | 34.8 | 33.2 | 39.0 |
| 5:20 | 36.4 | 38.6 | 35.0 | 39.0 |
| 5:42 | 35.2 | 39.8 | 35.5 | 39.0 |
| 5:50 | 35.8 | 39.9 | 36.2 | 39.0 |
| 6:05 | 36.3 | 40.0 | START | |

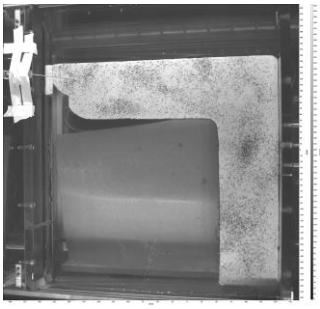

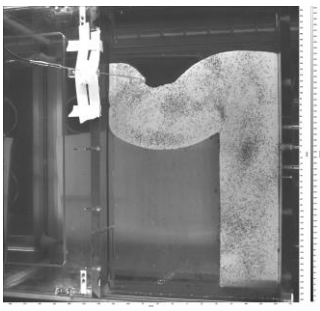

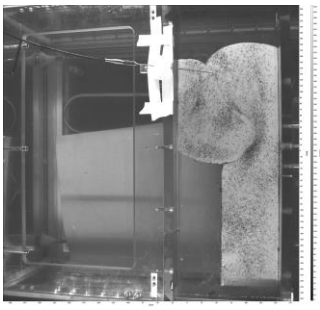

**Couplage :**

- *None*

**Speed :**

- 125 µm/s
- *Moving from:* 430 mm *to:* … mm

**Cameras :**

- *1*: back left
- *2*: 500 mm
- *3*: 468 mm
- *4*: 468 mm

**Waterline / Calibration height :**

- 5.3 cm **/** 6.8 cm

**Calibration :**

- *Pin-hole*

**Calibration error and scale :**

| Camera | RMS | Pix/mm |
|---|---|---|
| 2 | 0.322 | 3.970 |
| 3 | 0.149 | 4.080 |
| 4 | 0.159 | 4.080 |

**Picture frequency :**

- 0.5 Hz

**Laboratory Comments**
**Results**

Unfortunately the inner corner was not properly cut and the middle plate sunk during the experiment, the remaining ribbon still produced an interesting bend.

# LG-2012-D2 (19/11/12)

**Materials :**

- *Ribbons* : C5K2 New (ρ=0.98)
- *Ribbons' crusts*: (pale blue crust)

**Temperatures :**

- *Labo:* 23.7
- *Melting :* 65.0
- *Pouring:* 47.5
- *Surface:* 36.5
- *Asthenosphere:* 40.0

| Time | Actual | | Calibrated | |
|---|---|---|---|---|
| | Surface | Asthenosphere | Surface | Asthenosphere |
| 11:53 | 22.4 | 24.1 | 30.0 | 39.0 |
| 12:24 | 30.0 | 34.1 | 32.0 | 39.0 |
| 12:30 | 32.0 | 36.0 | 33.0 | 39.0 |
| 13:04 | 33.5 | 39.1 | 34.5 | 39.0 |
| 13:14 | 35.0 | 39.5 | 36.2 | 39.0 |
| 13:28 | 36.5 | 39.9 | START | |

**Couplage :**

- *None*

**Speed :**

- 250 µm/s
- *Moving from:* 430 mm *to:* … mm

**Cameras :**

- *1*: back left
- *2*: 500 mm
- *3*: 463 mm
- *4*: 463 mm

**Waterline / Calibration height :**

- 4.8 cm **/** 6.3 cm

**Calibration :**

- *Pin-hole*

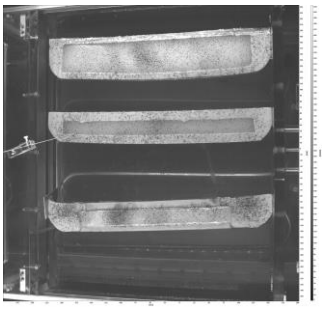

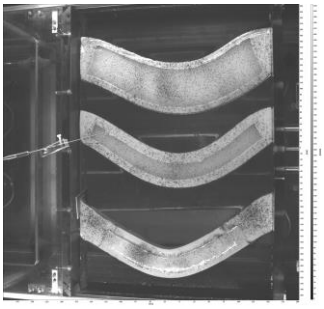

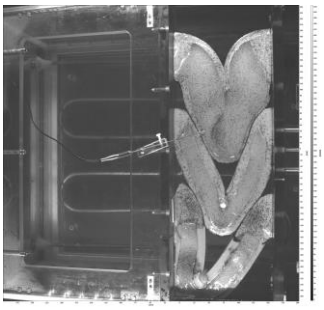

**Calibration error and scale :**

| Camera | RMS | Pix/mm |
|---|---|---|
| 2 | 0.319 | ? |
| 3 | 0.148 | ? |
| 4 | 0.170 | ? |

**Picture frequency :**

- 0.5 Hz

**Laboratory Comments**

**Results**

The ribbon with crust on the top was quite heavy, ended up bending in the middle towards the bottom, though the thermal gradient is far from accurate.

Careful, the force data has been taken in 2 steps, look at the dates for LG-2012-D1 and LG 2012-D2

# LG-2012-D3 (20/11/12)

**Materials :**

- *Asymmetric Ribbon* : C5K2 old (ρ=0.98)
- *Symmetric Ribbons*: C5K2 new (ρ=0.98)

**Temperatures :**

- *Labo:* 24.8
- *Melting$_{mantle}$ :* 65.0
- *Pouring:* 47.5
- *Surface:* 36.5
- *Asthenosphere:* 40.0

| Time | Actual | Calibrated | | |
|---|---|---|---|---|
| | Surface | Asthenosphere | Surface | Asthenosphere |
| 10:00 | 23.1 | 21.7 | 30.0 | 39.0 |
| 10:30 | 30.3 | 32.5 | 32.0 | 39.0 |
| 10:45 | 32.6 | 36.0 | 33.0 | 39.0 |
| 10:55 | 33.6 | 37.6 | 34.5 | 39.0 |
| 11:15 | 34.7 | 39.1 | 36.0 | 39.0 |
| 11:50 | 36.0 | 40.0 | 36.2 | 39.0 |
| 11:56 | 36.5 | 40.1 | START | |

**Stabilizes at** :

- 36.3 $^{0}$C
- 39.8 $^{0}$C

**Couplage :**

- *None*

**Speed :**

- 250 µm/s
- *Moving from:* 430 mm *to:* … mm

**Cameras :**

- *1*: back left
- *2*: 500 mm
- *3*: 473 mm
- *4*: 473 mm

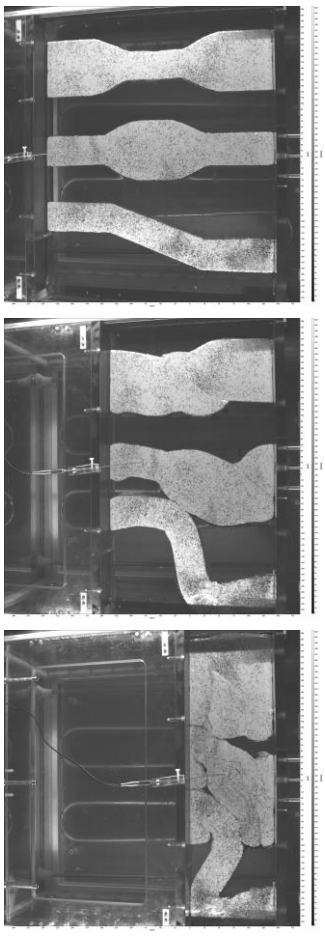

**Waterline / Calibration height :**

- 58 cm **/** 73 cm

**Calibration :**

- *Pin-hole*

**Calibration error and scale :**

| Camera | RMS | Pix/mm |
|---|---|---|
| 2 | 0.311 | 3.972 |
| 3 | 0.147 | 4.064 |
| 4 | 0.176 | 4.064 |

**Picture frequency :**

- 0.5 Hz

# LG-2012-C8 (23/11/12)

**Materials :**

- *Ribbon* : C5K2 new(ρ=0.98)
- Stable *continent*: C5K2 new (ρ=0.98)
- *Undertrusted mantle plates*: C5K1pink (p=1.03)

**Temperatures :**

- *Labo:* 23.6
- *Melting :* 65.0
- *Pouring:* 47.5
- *Surface:* 36.5
- *Asthenosphere:* 40.0

| Time | Actual | | Calibrated | |
|---|---|---|---|---|
| | Surface | Asthenosphere | Surface | Asthenosphere |
| 11:45 | 23.4 | 26.8 | 30.0 | 39.0 |
| 12:13 | 30.5 | 35.5 | 32.0 | 39.0 |
| 12:28 | 32.8 | 37.8 | 34.0 | 39.0 |
| 12:45 | 34.4 | 39.1 | 35.0 | 39.0 |
| 1:05 | 35.4 | 40.0 | 36.0 | 39.0 |
| 1:22 | 36.5 | 40.0 | 36.2 | 39.0 |
| 1:25 | 36.6 | 40.1 | START | |
| | | | | |

**Stabilizes at** :

- $^0$C and $^0$C

**Couplage :**

- *Paraffin oil on ribbon*

**Speed :**

- 125 µm/s
- *Moving from:* 430 mm *to:* … mm

**Cameras :**

- *1*: back left
- *2*: 500 mm
- *3*: 481 mm
- *4*: 481 mm

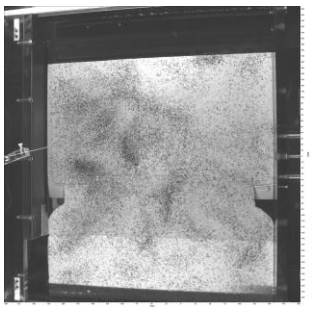

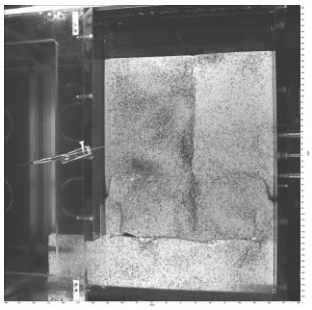

**Waterline / Calibration height :**

- 6.6 cm **/** 8.1 cm

**Calibration :**

- *Pin-hole*

**Calibration error and scale :**

| Camera | RMS | Pix/mm |
|---|---|---|
| 2 | 0.329 | 3.976 |
| 3 | 0.149 | 4.063 |
| 4 | 0.163 | 4.063 |

**Picture frequency :**

- 0.5 Hz

# LG-2012-C9 (25/11/12)

**Materials :**

- *Ribbon* : C5K2 new(ρ=0.98)
- *Mantle$_{Subducting}$*: C5K1pink (ρ=1.03)
- *Crust*: blue (ρ=0.860)

**Temperatures :**

- *Labo:* 23.0
- *Melting :* 65.0
- *Pouring:* 47.5
- *Surface:* 36.5
- *Asthenosphere:* 40.0

| Time | Actual | | Calibrated | |
|---|---|---|---|---|
| | Surface | Asthenosphere | Surface | Asthenosphere |
| 11:00 | 23.0 | 23.0 | 30.0 | 39.0 |
| 11:40 | 30.6 | 35.1 | 32.0 | 39.0 |
| 11:56 | 32.6 | 37.6 | 34.0 | 39.0 |
| 12:16 | 34.4 | 39.4 | 35.5 | 39.0 |
| 12:48 | 35.3 | 39.8 | 36.2 | 39.0 |
| 13:00 | 36.0 | 40.0 | START | |
| | | | | |
| | | | | |

**Stabilizes at** :

- 39.6 $^{0}$C
- 36.4 $^{0}$C

**Couplage :**

- *Paraffin oil at subduction zones*

**Speed :**

- 125 µm/s
- *Moving from:* 430 mm *to:* … mm

**Cameras :**

- *1*: back left
- *2*: 500 mm
- *3*: 484 mm
- *4*: 484 mm

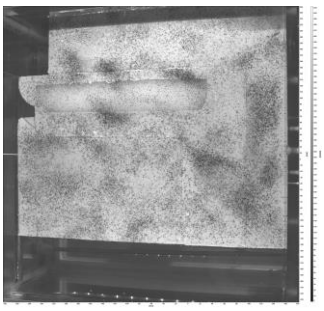

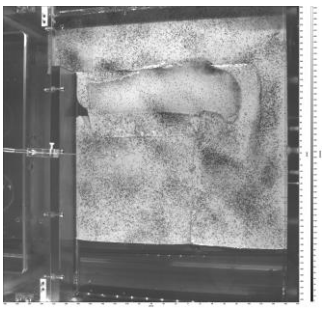

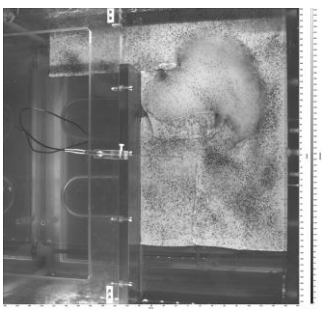

**Waterline / Calibration height :**

- 6.9 cm **/** 8.4 cm

**Calibration :**

- *Pin-hole*

**Calibration error and scale :**

| Camera | RMS | Pix/mm |
|---|---|---|
| 2 | 0.4269 | 3.97 |
| 3 | 0.156 | 4.216 |
| 4 | 0.122 | 4.216 |

**Picture frequency :**

- 0.5 Hz

# LG-2012-C10 (26/11/12)

**Materials :**

- *Ribbon* : C5K2 new(ρ=0.98)
- $Mantle_{Subducting}$: C5K1 pink(ρ=1.03)
- *Stable Continent*: C5K2 new (ρ=0.98)
- $Mantle_{Overriding}$ : C5K2 new (ρ=0.98)

**Temperatures :**

- *Labo:* 21.0
- *Melting :* 65.0
- *Pouring:* 47.5
- *Surface:* 36.5
- *Asthenosphere:* 40.0

| Time | Actual | | Calibrated | |
|---|---|---|---|---|
| | Surface | Asthenosphere | Surface | Asthenosphere |
| 3:08 | 22.3 | 25.2 | 30.0 | 39.0 |
| 3:41 | 30.7 | 35.7 | 32.0 | 39.0 |
| 3:56 | 32.6 | 38.0 | 34.2 | 39.0 |
| 4:15 | 34.8 | 39.5 | 35.2 | 39.0 |
| 4:48 | 35.5 | 39.5 | 36.2 | 39.0 |
| 5:03 | 36.3 | 39.9 | START | |

**Stabilizes at** :

- $^0$C and $^0$C

**Couplage :**

- *Paraffin oil on ribbon and subduction zone*

**Speed :**

- 125 µm/s
- *Moving from:* 430 mm *to:* … mm

**Cameras :**

- *1*: back left
- *2*: 500 mm
- *3*: 489 mm
- *4*: 489 mm

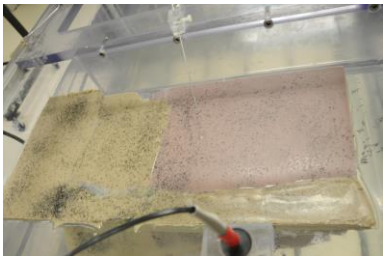

**Waterline / Calibration height :**

- 7,4 cm (too low, ribbon lower than piston **/** 8.9 cm

**Calibration :**

- *Pin-hole*

**Calibration error and scale :**

| Camera | RMS | Pix/mm |
|---|---|---|
| 2 | 0.31 | 3.99 |
| 3 | 0.156 | 4.23 |
| 4 | 0125 | 4.23 |

**Picture frequency :**

- 0.5 Hz

# LG-2012-C11 (28/11/12)

**Materials :**

- *Ribbon* : C5K2 new (ρ=0.98)
- *Mantle*: C5K1pink (ρ=1.03)
- *Stable Continent*: C5K2 new (ρ=0.98)

**Temperatures :**

- *Labo:* 23.6
- *Melting$_{mantle}$ :* 65.0
- *Pouring:* 47.5
- *Surface:* 56.5
- *Asthenosphere:* 39.0

| Time | Actual | | Calibrated | |
|---|---|---|---|---|
| | Surface | Asthenosphere | Surface | Asthenosphere |
| 11:03 | 24.0 | 25.5 | 30.0 | 39.0 |
| 11:32 | 30.1 | 32.5 | 32.0 | 39.0 |
| 11:52 | 32.7 | 36.6 | 34.0 | 39.0 |
| 12:09 | 34.2 | 38.4 | 35.5 | 39.0 |
| 12:21 | 35.4 | 39.4 | 36.2 | 39.0 |
| 12:52 | 36.5 | 40.0 | 36.2 | 39.0 |
| | | | START | |

**Stabilizes at** :

- 36.0 $^{0}$C
- 39.6 $^{0}$C

**Couplage :**

- *Paraffin oil on ribbon and subduction zone*

**Speed :**

- 125 µm/s
- *Moving from:* 430 mm *to:* … mm

**Cameras :**

- *1*: back left
- *2*: 500 mm
- *3*: 455 mm
- *4*: 455 mm

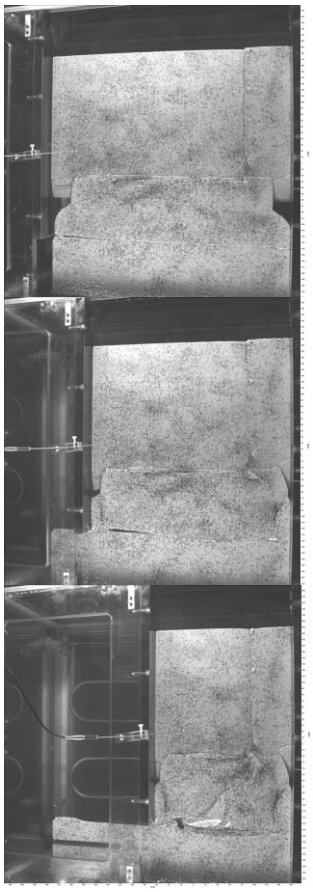

**Waterline / Calibration height :**

- 4.0 cm **/** 5.5 cm

**Calibration :**

- *Pin-hole*

**Calibration error and scale :**

| Camera | RMS | Pix/mm |
|---|---|---|
| 2 | 0.429 | ? |
| 3 | 0.162 | ? |
| 4 | 0.105 | ? |

**Picture frequency :**

- 0.5 Hz

# LG-2012-C12 (29/11/12)

**Materials :**

- *Ribbon* :C5K2 new (ρ=0.98)
- $Mantle_{Subducting}$: C5K1pink (ρ=1.03)

**Temperatures :**

- *Labo:* 21.5
- *Melting :* 65.0
- *Pouring:* 47.5
- *Surface:* 36.5
- *Asthenosphere:* 40.0

| Time | Actual | | Calibrated | |
|---|---|---|---|---|
| | Surface | Asthenosphere | Surface | Asthenosphere |
| 9:53 | 23.9 | 22.2 | 30.0 | 39.0 |
| 10:12 | 30.2 | 34.5 | 32.0 | 39.0 |
| 10:34 | 33.0 | 37.9 | 34.0 | 39.0 |
| 10:52 | 34.1 | 39.1 | 35.2 | 39.0 |
| 11:13 | 35.6 | 40.0 | 36.2 | 39.0 |
| 11:41 | 36.5 | 39.9 | START | |

**Couplage :**

- *Paraffin oil*

**Speed :**

- 125 µm/s
- *Moving from:* 430 mm *to:* … mm

**Cameras :**

- *1*: back left
- *2*: 500 mm
- *3*: 469 mm
- *4*: 469 mm

**Waterline / Calibration height :**

- 5.4 cm **/** 6.9 cm

**Calibration :**

- *Pin-hole*

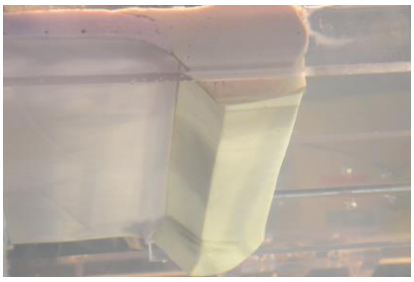

**Calibration error and scale :**

| Camera | RMS | Pix/mm |
|---|---|---|
| 2 | 0.422 | ? |
| 3 | 0.1618 | 4.204 |
| 4 | 0.137 | 4.204 |

**Picture frequency :**

- 0.5 Hz

# LG-2012-C13 (30/11/12)

**Materials :**

- *Ribbon* : C5K2 new (ρ=0.98)
- *Mantle$_{Underriding}$*: C5K1 pink(ρ=1.03)
- *Stable Continent*: C5K2 new (ρ=0.98)

**Temperatures :**

- *Labo:* 24.8
- *Melting :* 65.0
- *Pouring:* 47.5
- *Surface:* 36.5
- *Asthenosphere:* 40.0

| Time | Actual | | Calibrated | |
|---|---|---|---|---|
| | Surface | Asthenosphere | Surface | Asthenosphere |
| 10:52 | 20.0 | 20.0 | 30.0 | 39.0 |
| 11:38 | 30.4 | 35.5 | 33.0 | 39.0 |
| 12:05 | 33.3 | 39.0 | 35.2 | 39.0 |
| 12:30 | 35.7 | 39.9 | 36.2 | 39.0 |
| 12:45 | 36.3 | 40.0 | START | |

**Couplage :**

- *Paraffin oil on ribbon*

**Speed :**

- 125 µm/s
- *Moving from:* 430 mm *to:* … mm

**Cameras :**

- *1*: back left
- *2*: 500 mm
- *3*: 471 mm
- *4*: 471 mm

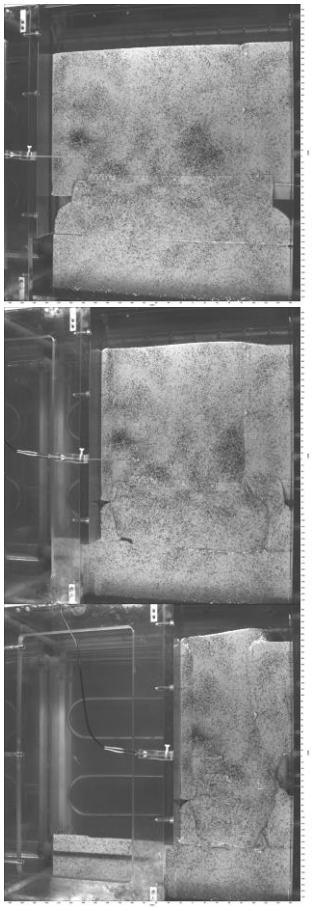

**Waterline / Calibration height :**

- 5.6 cm **/** 7.1 cm

**Calibration :**

- *Pin-hole*

**Calibration error and scale :**

| Camera | RMS | Pix/mm |
|---|---|---|
| 2 | 0.436 | 3.953 |
| 3 | 0158 | 4.208 |
| 4 | 0.104 | 4.208 |

**Picture frequency :**

- 0.5 Hz

# LG-2012-D4 (01/12/12)

**Materials :**

- *Ribbons* : C5K2 new (ρ=0.98)
- $Mantle_{Undertrusted}$: C5K1 pink (ρ=1.03)

**Temperatures :**

- *Labo:* 25.8
- *Melting:* 65.0
- *Pouring:* 47.5
- *Surface:* 40.0
- *Asthenosphere:* 36.5

| Time | Actual | | Calibrated | |
|---|---|---|---|---|
| | Surface | Asthenosphere | Surface | Asthenosphere |
| 3:00 | 24.0 | 24.9 | 30.0 | 39.0 |
| 3:30 | 30.6 | 35.4 | 32.0 | 39.0 |
| 3:42 | 32.7 | 37.0 | 34.2 | 39.0 |
| 3:55 | 34.5 | 38.6 | 35.2 | 39.0 |
| 4:10 | 35.2 | 39.3 | 36.2 | 39.0 |
| | | | START | |

**Couplage :**

- *Paraffin oil for ribbon*

**Speed :**

- 250 µm/s
- *Moving from:* 430 mm *to:* … mm

**Cameras :**

- *1*: back left
- *2*: 500 mm
- *3*: 483 mm
- *4*: 483 mm

**Waterline / Calibration height :**

- 6.8 cm **/** 8.3 cm

**Calibration :**

- *Pin-hole*

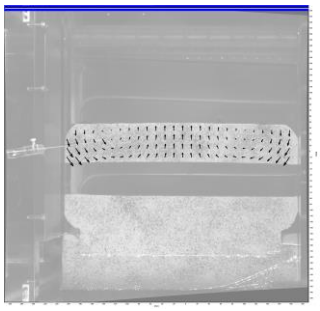

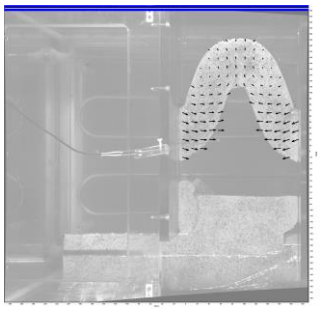

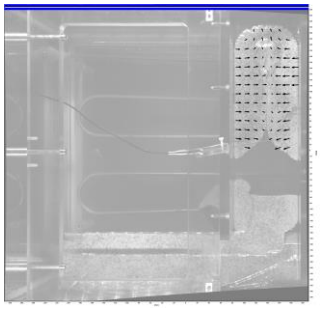

**Calibration error and scale :**

| Camera | RMS | Pix/mm |
|---|---|---|
| 2 | 0.324 | 3.97 |
| 3 | 0.187 | 4.21 |
| 4 | 0.149 | 4.21 |

**Picture frequency :**

- 0.5 Hz

# LG-2012-D5 (03/11/12)

**Materials :**

- *Ribbons on the sides* : C5K2 new(ρ=0.98)
- *Ribbon in the midde* : C5K2 old (ρ=0.98)
- *Plate* $_{Overriding}$: C5K2 old (ρ=0.98)

**Temperatures :**

- *Labo:* 24.2
- *Melting :* 65.0
- *Pouring:* 47.5
- *Surface:* 36.5
- *Asthenosphere:* 40.0

| Time | Actual | | Calibrated | |
|---|---|---|---|---|
| | Surface | Asthenosphere | Surface | Asthenosphere |
| 9:30 | 21.7 | 20.7 | 30.0 | 39.0 |
| 10:00 | 30.4 | 33.0 | 32.0 | 39.0 |
| 10:22 | 32.8 | 37.0 | 34.0 | 39.0 |
| 10:35 | 34.4 | 38.6 | 35.5 | 39.0 |
| 11:00 | 36.1 | 39.8 | 36.2 | 39.0 |
| 11:12 | 36.5 | 40.0 | START | |

**Couplage :**

- *None*

**Speed :**

- 250 µm/s
- *Moving from:* 430 mm *to:* … mm

**Cameras :**

- *1*: back left
- *2*: 500 mm
- *3*: 476 mm
- *4*: 476 mm

**Waterline / Calibration height :**

- 6.1 cm **/** 7.6 cm

**Calibration :**

- *Pin-hole*

**Calibration error and scale :**

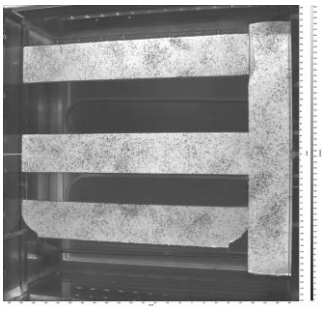

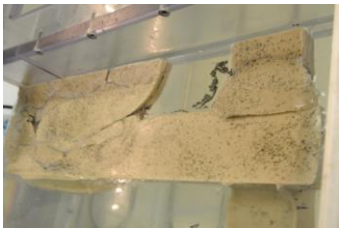

| Camera | RMS | Pix/mm |
|---|---|---|
| 2 | 0.294 | ? |
| 3 | 0.183 | ? |
| 4 | 0.151 | ? |

**Picture frequency :**

- 0.5 Hz